3-21-2013

Discrimination Between Child and Adult Forms Using Radar Frequency Signature Analysis

Stephanie R. Keith

Discrimination Between Child and Adult Forms Using Radar Frequency Signature Analysis

THESIS

Stephanie R. Keith, Captain, USAF

AFIT-ENP-13-M-20

DEPARTMENT OF THE AIR FORCE
AIR UNIVERSITY

AIR FORCE INSTITUTE OF TECHNOLOGY

Wright-Patterson Air Force Base, Ohio

AFIT-ENP-13-M-20

DISCRIMINATION BETWEEN CHILD AND ADULT FORMS USING RADAR FREQUENCY SIGNATURE ANALYSIS

THESIS

Presented to the Faculty

Department of Engineering Physics

Graduate School of Engineering and Management

Air Force Institute of Technology

Air University

Air Education and Training Command

in Partial Fulfillment of the Requirements for the

Degree of Master of Science in Applied Physics

Stephanie R. Keith, B.S.

Captain, USAF

March 14, 2013

AFIT-ENP-13-M-20

DISCRIMINATION BETWEEN CHILD AND ADULT FORMS USING RADAR FREQUENCY SIGNATURE ANALYSIS

Stephanie R. Keith, B.S.
Captain, USAF

Approved:

Amy L Magnus	4 March 2013
Dr. A. L. Magnus Chairman	Date
Anadia Miranda	4 March 2013
Dr. A. Miranda Member	Date
C. Borel	4 March 2013
Dr. C. Borel-Donohue Member	Date

AFIT-ENP-13-M-20

Abstract

In this thesis we develop a method to discriminate between adult and child radar signatures. In particular, we examine radar data measured from behind a wall, which introduces radar signal attenuation and multipath effects. To investigate the child/adult discrimination problem in a through-wall, multipath scenario, a previously developed free-space human scattering model was expanded to incorporate multiple paths, and the effects of transmission through, and reflections from, walls and ground. The ground was modeled as a perfectly reflecting surface, while the walls were modeled as homogeneous concrete slabs. Twenty-five reflection paths were identified, involving the direct paths, as well as reflected paths between the ground and an adjacent wall. All paths included two-way transmission through an obstructing wall.

In addition to the model expansion, radar scattering measurements were collected from human volunteers, both child and adult, in order to investigate the classification of child and adult through-wall radar data. To our knowledge, this thesis is the first published work that analyzes child radar scattering data. A classification accuracy of above 95% was reached in both the time and frequency domains, indicating that, with minimal processing, a high degree of certainty is achievable in characterizing a subject behind a wall, in a real-world, multipath environment.

Acknowledgements

Embrace entropy.

This thesis has been a phenomenal experience for me, even if the experiments seemed to obey Murphy's law more than any other. There were frequent references to something called "karma," specifically mine, but, despite all that, we were able to bring the project to a successful conclusion. It was not, however, without the help of several extraordinary people, who have my deepest gratitude.

First and foremost, I thank my sponsor, Dr. Analee Miranda, and my advisor, Dr. Amy Magnus, for giving me the opportunity to carry out this research, and for giving me the aid and advice I needed in order to get things done. Dr. Miranda, in particular, spent several long nights with me, hammering out corrections and ideas to pursue, and was instrumental in coordinating the various parties involved with this extensive project. Additionally, thanks to AFRL, RYMD, and AFOSR for further sponsorship and support, and, in particular, Dr. Arje Nachman for useful comments.

I also thank Chad Waddington for his assistance in conducting the experiments, and Loria Wang for her help, especially at the last minute. Thank you, also, to Dr. Grant Erdmann provided for providing the SVM code and advice. A big thank you goes out to Darrell Lochtefeld for the design of my infamous concrete wall, and to Ron Miller for its tireless construction. Additional thanks to the rest of RHXB, Matrix Research, and Jim Reed, Reimy Emmanuel and the rest of the AFRL Indoor Range team for their roles in getting the obnoxious thing transported and set up.

Thank you to Dr. Dustin Bruening for IRB support, to TSgt Thomas Waldrop for such quick turnaround in getting safety measurements for our radar systems, to Tim Tanigawa for his radar experience, to Dr. Boris Tomasic for his aid in spherical vector harmonics, to the Bleszynskis of Monopole Research for providing documentation, to

the STAMR group for the invaluable suggestion of PCA, to Dr. Richard Albanese for additional helpful comments, and to all my volunteers for making this experiment possible (you know who you are).

Thank you to my Space Weather class for valuable (and entertaining) advice on my defense presentation.

Finally, last but certainly not least, I thank my sister, my parents, and my best friends, for giving me the support and understanding I needed to hide away from the rest of the world in order to get everything done.

Stephanie R. Keith

Table of Contents

List of Figures

List of Tables

DISCRIMINATION BETWEEN CHILD AND ADULT FORMS
USING RADAR FREQUENCY SIGNATURE ANALYSIS

I. Introduction

Medical imaging modalities often illuminate humans with electromagnetic radiation in order to infer the properties of living tissue. With its longer wavelengths, radar may be used to infer larger features such as head size and thigh length. Additionally, similar to how a law-enforcement professional uses radar to determine the speed of a driver, we can use radar to detect the speed of human limbs. Anthropologists use measurements to characterize and classify groups of humans with similar features. Radar data may be used in conjunction with physical measurements to build an age classification tool that may ultimately provide a method of remotely characterizing human activity.

Unlike optical sensors, radar systems need not rely upon line-of-sight or good weather to perform well. Radar is capable of penetrating building materials, cloth, and foliage due to its long wavelength, and thus is ideal for the detection of objects behind barriers and other visual obstructions. Work has been done in imaging humans using radar both from the standpoint of a moving platform [1], and through walls at close range, from a stationary platform [2, 3, 4, 5, 6, 7, 8, 9, 10, 11]. Through-wall radar provides vital information about the situation inside buildings. The ability to distinguish between types of people, such as adults and children, becomes especially important in situations like the Sandy Hook Elementary school shooting, in which law enforcement had no ability to determine where the children were located with respect to the shooter. Although previous work has been done in both identifying

human activity and distinguishing male from female, no research has yet developed models which discriminate between children and adults.

1.1 Problem

The problem tackled by this thesis is two-fold: multipath modeling and child/adult classification. A human radar signature inside a building is complicated by clutter due to obstructions and objects inside the building. Incorporating these varied effects in a human radar signature model is difficult. Previous human scattering models have included scattering due to humans in the presence of ground. The first part of this thesis builds upon the work by Miranda, et al. [12, 13, 14, 15] to create a sphere-cylinder representation of a human and a human radar scattering model, modified to incorporate the multipath effects due to a corner, i.e., the ground and a wall adjacent to the target.

The second part of the problem is the classification of the child or adult. This project will identify features in the radar-scattering data that best distinguish a child from an adult, and use a Support Vector Machine, a type of binary classification tool, to classify the subjects based on these features. Finally, the results of the Support Vector Machine will be explored using Principal Component Analysis to reveal the relationship between child and adult classes.

1.2 Research Goals

In addition to the dual goals of developing the ground-wall human scattering model and the classifier, experimental data will be gathered to validate the scattering model and test the classification. The experiment setup will consist of a pair of concrete walls arranged to form a corner. Human volunteers serve as the test subjects. Through-the-wall radar-scattering data will be gathered from both children and adults.

1.3 Overview

The remainder of this document is organized as follows: Chapter II provides a review of previous research regarding the radar detection of humans and human classification methods. Chapter III details background material and lays the project's foundation. Chapter IV launches into the theory necessary to advance the project, while Chapter V provides the research approach and experimental procedures. Chapter VI details the results and their analysis and discussion, and, finally, Chapter VII presents the conclusions, implications of the research, and suggestions for future work.

II. Radar Detection of Humans and Human Classification

A significant effort has been made in identifying human subjects with radar data, classifying their movements, and locating them through obstructions such as walls. What follows in this chapter is an overview of recent research pertinent to the problem of radar human detection, emphasizing those which provide the framework for this thesis. Efforts in human line-of-sight radar detection are discussed first, along with research in identifying characteristic human movements. Following this, we present a discussion of through-the-wall radar imaging. This chapter concludes with prior work in the classification of humans.

2.1 Line-of-Sight Human Detection via Radar

Detection of humans using radar typically employs Doppler radar. Doppler radar takes advantage of the frequency shift of a moving target in order to isolate it from background stationary objects, and thus suppress clutter. The Doppler signatures of moving objects are typically divided into two categories: "simple" Doppler and micro-Doppler. Simple Doppler refers to the overall motion of an object — its lateral translation in space, for example. In our detection scenario, this motion would correspond to a human or animal moving across a room. Micro-Doppler contributes to the overall Doppler return signal and can be extracted from it. These micro-Doppler features stem from the movement of individual components of the subject: the swinging of arms and legs, for example, as well as the more subtle variations of physiological movement — the small fluctuations of the body and skin due to breathing and the beating of the heart. These micro-Doppler movements are small and difficult to isolate from noise, yet the isolation has been done, and research is ongoing.

In many remote detection situations, a moving target can indicate a human pres-

ence. However, the target may be also be another moving object or animal. In order to reliably determine the presence of a human, work has been done to analyze the features characteristic of human motion. Mainly, these distinguishing features are present in the micro-Doppler. Because humans move in a fundamentally different way from other animals, their micro-Doppler signatures are unique. Indeed, as researchers have been able to distinguish between different species [16, 17], we may also be able to distinguish individual humans. We expect that each person possesses a unique set of "micro-motions" and so has his or her own "micro-Doppler signature", provided the individual micro-Doppler components could be resolved sufficiently [18].

The following subsections briefly describe efforts in line-of-sight motion detection. First, we discuss the micro-Doppler motion of parts of the body. Then, physiological monitoring is presented separately. A more specific application of micro-Doppler signatures, physiological monitoring is considerably more difficult, requiring a much wider bandwidth or higher frequency than other micro-Doppler motions.

Motion Detection

In many efforts to characterize the motion of humans, the radar spectrogram has become the preferred method (Figure 1(a)). The spectrogram, generated by the short-time Fourier transform (STFT) on time domain radar data, displays the various component frequencies that comprise the motion of an object, including the motion of the torso, arms, and legs. A human radar spectrogram varies depending on how the subject moves and the way the subject carries objects [19, 2]. Resolution of the different frequency components of the spectrogram improves as incident radar wavelength shortens [2].

The spectrogram has been used as a measurement tool to create a realistic walking model of a human with reasonable accuracy [20]. The spectrogram can be further

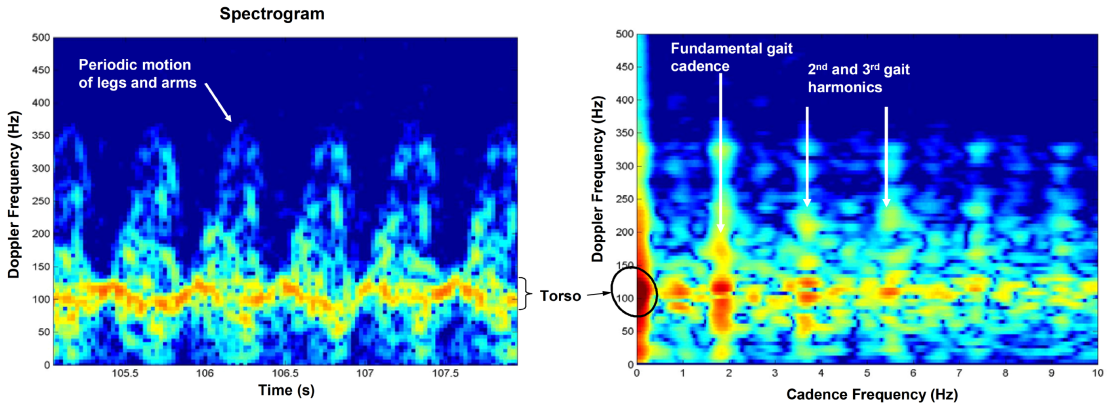

(a) (b)

Figure 1. The Spectrogram and Cadence Frequency of a Walking Human. Plot (a) displays the spectrogram of a walking human over a period of three seconds. The graph is formed from short-time Fast Fourier Transforms of the radar data. The component with the highest amplitude (shown in red) is associated with the torso, which has a Doppler frequency near 100 Hz, correpsonding to a velocity of 1.4 m/s. The motion of the arms and legs are seen in the sawtooth pattern above the torso component. This motion produces a cadence frequency of about 2 Hz. The cadence frequencies are shown in (b). The torso again produces the strongest intensity; its cadence frequency is near zero due to its near-constant velocity. [Reprinted with permission from [16]].

evaluated using tools such as cadence frequency plots, which display periodic micro-Doppler signals present in the spectrogram (see Figure 1(b)), in order to characterize subjects using features such as speed, stride length, and body ratios to determine actions, size, gender and species [21, 16, 22].

Gürbüz [21] cautions against applying the cadence frequency plot to estimate subject parameters, especially with limited data of the subject or when noise and clutter are present. The estimation works well when there is low noise and the subject is close to the antenna, resulting in high signal-to-noise ratio. Parameter estimation from the spectrogram is also sub-optimal for human subject reflections because the signals have nonlinear phase. An alternative backprojection-style technique described in [21] tends to be significantly more accurate when noise is present. Unfortunately, the iterative technique is computationally intensive, rendering it impractical for real-time detection. Cadence frequency plots appear to be useful for the study of human

walking motion in controlled, laboratory settings, yet, again, care must be taken when applying the method to real-world, complex scenarios.

Despite the drawbacks in the use of cadence frequency plots, the spectrograms themselves are rich in information that characterizes the moving subject, in terms of the component frequencies and shape of the spectrogram. The spectrograms of individual limbs of a walking human have been isolated [2, 23], and those characterizing different types of movements have been studied [7, 19, 23, 24]. This information may be used to classify human activity [19, 24] (discussed later). Additionally, improvements upon the basic spectrogram methods have been proposed, including the reassigned joint time-frequency (RJTF) transform [2], and an approach using a quadratic time-frequency S-method in conjunction with the Viterbi algorithm [18].

Physiological Monitoring

In this paper, physiological monitoring refers to the detection of the life signs of a person — respiration and heartbeat — distinguishing this type of measurement from the measurement of larger motion, such as translational or limb movement. Physiological measurements can be obtained with other micro-Doppler measurements, but they require an accurate radar system using a very wide bandwidth, or high frequency, in order to resolve the motion of the chest and skin.

The interest in physiological monitoring lies in the possibility of detecting a person's life signs from a distance. Standoff detection can aid in locating disaster victims trapped in rubble, who are unable to move, but can still breathe. Physiological monitoring from a distance could aid the measurement of vital signs of those who cannot have detectors placed directly on the skin, such as burn victims. It may also be useful in law enforcement and military application in detecting people hidden behind doors, in closets or containers, in assessing casualties from a distance when it may

be dangerous to approach, and in monitoring vital signs through chemical or biological protection suits. These military applications have seen research as early as the mid-1980s, under the term Radar Vital Signs Monitor (RVSM), developed by the Georgia Tech Research Institute [25]. This monitoring system could detect heartbeat and respiration up to 100 meters from the subject; however, it suffered at high ranges due to clutter from moving foliage. Georgia Tech developed a later version in 1996 to evaluate Olympic athlete performance. Operating at 24.1 GHz, the new version was able to detect the pressure wave propagating across the thorax from the pumping of the heart. The display of this pressure wave served as a time domain radar cardiogram [25].

Yarovoy [26], rather than using a single high-frequency tone, employed an ultra-wide bandwidth of 11.7 GHz in order to carry out frequency spectrum analysis to detect human respiration. This bandwidth provided a resolution of 1.3 cm, and was sufficient for showing the difference in amplitude due to inhalation and exhalation of the lungs in the time domain. Yarovoy also noted that minor movements of a stationary human contributed greatly to the spectral variation of the radar return; thus, a person could be detected, not only by respiration, but also by these small movements.

Most applications of physiological monitoring via radar involve through-the-wall detection and implementation of ultra-wide band radar, as used by Yarovoy. Ultra-wide band radar and efforts in physiological through-the-wall detection are discussed in the following section.

2.2 Through-the-Wall Radar Imaging

Radar applications most relevant to this thesis are those involving through-the-wall detection of targets. Analysis of such radar signals provides information of

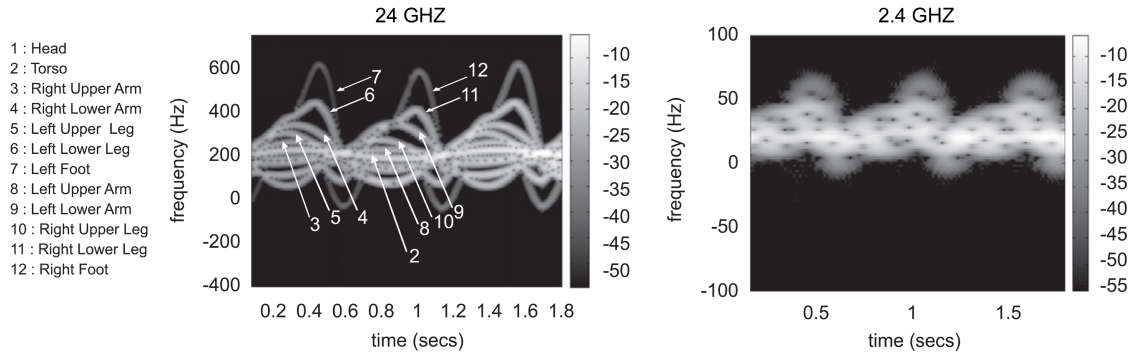

Figure 2. Frequency Tradeoff (reproduced from [2]). Both plots display the simulated STFT spectrogram of a human walking at 1.4 m/s toward a Doppler radar. The plot on the left shows the results for a carrier frequency of 24 GHz — the resolution is superior, with contributions by portions of the body easily identifiable and labeled. The plot on the right displays results for a carrier frequency of 2.4 GHz. The micro-Doppler components are blurred and difficult to distinguish.

activities occurring out of view of observers. Radar signal attenuation though walls increases quickly as a function of frequency, so frequencies below 5 GHz are often used [2], ideally restricting the bandwidth to the ultra-high frequency (UHF) range, about 500-1000 MHz, for best penetration. There is a trade-off, however, between Doppler sensitivity and signal penetration: signal penetration improves with lower frequency, but sensitivity and resolution improve at higher frequency. The difference in frequency resolution was demonstrated by Ram [2] in the comparison of spectrogram simulations of a walking human at carrier frequencies of 2.4 GHz and 24 GHz. As seen in Figure 2, the spectrogram of 24 GHz has better resolution of the micro-Doppler components, but through-wall signal attenuation at this frequency is severe.

A second property of through-the-wall radar imaging is employment of an ultra-wide band spectrum. Ultra-wide band (UWB) radar provides superior resolution and information content not available in a single frequency. The two characteristics of UHF and UWB are the common properties behind good through-the-wall radar imaging systems. Noise waveforms are also used, as they have properties suitable for accurate and inconspicuous detection of subjects. [3]

The next two sections briefly describe the merits of UWB radar and UWB noise radar, as they apply to through-the-wall imaging, including prior efforts in through-the-wall detection of humans using these types of systems.

Ultra-Wide Band Radar

Ultra-wide band (UWB) radar is defined as having a signal with a fractional bandwidth greater than 20% [27]. The fractional bandwidth, Δf, is defined as [27]

$$\Delta f = \frac{2(f_H - f_L)}{f_H + f_L} = \frac{f_H - f_L}{f_0} \tag{1}$$

where f_H and f_L are the upper and lower boundaries of the bandwidth, respectively, and f_0 is the average of the two frequencies. A wide bandwidth provides good range resolution. For the bandwidth $B = f_H - f_L$, the range resolution ΔR is [28]

$$\Delta R = \frac{c}{2B} \tag{2}$$

where c is the wave propagation speed (speed of light for EM waves in vacuum). Additionally, depending on the ratio of wavelength to object size, the wide bandwidth may provide information from different scattering regimes. For an object of size l under incident radiation of wavelength λ, there are three regimes of scattering: Rayleigh ($\lambda >> l$), resonance ($\lambda \approx l$), and optical ($\lambda << l$). Provided the bandwidth is large enough, the scattered signal can provide information about the object in all three regimes [28].

Noise Radar

Random noise radar, although not applied in this thesis, is mentioned here due to its advantages in through-the-wall detection. Random noise radar employs a non-

periodic, incoherent waveform which provides two main advantages in radar detection. The first is the suppression of range and Doppler ambiguity which allows unambiguous high-resolution imaging [3, 28]. For example, for a periodic waveform with repetition frequency f_r, ambiguity in range occurs when the range $R > R_{rep} = c/(2f_r)$ [28]. A non-periodic noise waveform has $f_r = 0$, ensuring that the range ambiguity condition is never met. The second advantage is the inherent low probability of intercept (LPI) and low probability of detection (LPD) afforded by noise waveforms. Periodic pulses of energy are easily detected and recognized by adversaries who would employ countermeasures to avoid detection, such as jamming and interference. Noise waveforms, on the other hand, are extremely difficult, if not impossible, to detect and jam. Since they are featureless, such waveforms are ideal for covert, through-the-wall sensing in hostile environments [3].

Coupled with UWB radar, a noise radar system appears to be the ideal in accurate, through-the-wall, covert imaging. Such a system provides real-time Doppler discrimination and target tracking at low cost, with high resolution that diminishes the effects of multipath and clutter. The following sections will detail some of the recent efforts in through-wall human detection, to include successes with noise radar.

Human Detection

Through-the-wall detection of humans began in the 1980s to search for signs of life of survivors trapped during natural disasters [4]. Recent efforts in the detection and tracking of humans include through-the-wall scenarios for military and law enforcement applications, particularly with random noise radar, and employing micro-Doppler extraction; one portable system with a future backpack design was even introduced in [4]. These experiments have been divided into two categories: motion detection and physiological monitoring.

Motion Detection

The motion detection problem includes the tracking of humans within a room and identification of activities performed, a very difficult goal, particularly when the human subject cannot be visually seen. Researchers at the University of Texas investigated methods of gathering location information on multiple moving human subjects, using a carrier frequency of 2.4 GHz [2]. Using Doppler discrimination, the researchers were able to determine the azimuth direction of arrival (or bearing) of the subjects, provided that each subject is moving at a different radial velocity with respect to the radar. Their method was later extended to capture two-dimensional azimuth-elevation and three-dimensional range-azimuth-elevation information. The researchers found, however, that the probability of successful resolution of multiple subjects drops off as the number of subjects increases [2].

Another through-wall motion tracking technique was described by Wang [5]. This technique employs the subtraction of successive frames of cross-correlation signals between each received and transmitted signal. In essence, it extracts the signals of moving subjects — suppressing interference between transmit and receive antennas and environmental clutter — and leaves only the moving subject (or multiple moving subjects) to be displayed via a back projection algorithm. If the wall electrical parameters of dielectric constant and conductivity are unknown or incorrect, the image of the moving subject is displaced a distance less than the system resolution, which is usually acceptable.

Because human body motion is usually non-linear and non-stationary, Hilbert-Huang transform (HHT) analysis proved a viable method of time-frequency analysis and isolation of various movement profiles [6, 7]. This technique involves empirical mode decomposition (EMD), which empirically identifies intrinsic oscillatory modes (or intrinsic oscillatory mode functions, IMFs) that are defined by their time scales

of oscillation. The original signal is decomposed into these IMFs, then Hilbert transform is applied to derive the instantaneous amplitude and frequency of the IMF. The time-frequency distribution of the IMF amplitude, i.e., the Hilbert spectrum, can then be plotted, resulting in a spectrogram similar to the STFT spectrograms presented previously. However, the HHT spectrograms have higher time and frequency resolution and are better able to display fluctuations in repetitive movements of human subjects, such as a waving arm. The STFT spectrogram is less capable of displaying these minute differences. HHT analysis is thus more appropriate in detecting variations of movement in noisy environments, such as through-the-wall scenarios. [6]

Individual IMFs contain unique oscillatory information present in a scene, so it is possible to isolate individual movements, or combinations of movements, by separating IMFs that contain information of a particular movement of interest. Narayanan [7] used the energy distribution across IMFs to characterize different through-wall movements — such as standing and breathing, shuffling while seated, moving arms rapidly up and down, and lifting large objects — and to differentiate them from the absence of a human. Additionally, the IMFs were used to recreate the Doppler signatures from the movement of different sections of the arm.

A relatively recent technology called the Radar Scope, developed by DARPA, was a hand-held device capable of detecting movements as small as breathing through a foot of concrete and 50 feet into a room [8]. Another DARPA technology, called VisiBuilding, is a much more advanced system. It is intended to see through multiple walls in order to image entire floor plans, as well as occupant and object locations, as fully-usable, model-based diagrams rather than "radar blurs" common to most imaging techniques [9].

Physiological Monitoring

The detection of human physiological information is a difficult problem that becomes worse when attempted through barriers such as walls. Physiological movements — the rise and fall of a person's chest as they breathe, the beating of the heart and the small, associated fluctuations produced in the skin — are very small compared to limb movements. Thus, limitations on the use of physiological monitoring techniques exist. A human subject must face the radar because the Doppler shift will be indistinguishable otherwise. Additionally, the subject must be near to the separating wall. Averaging is necessary to determine the central Doppler shift which takes additional time. A through-the-wall detection system must necessarily be low-frequency to avoid signal attenuation, yet the bandwidth to detect the small motions of breathing (3.75 cm resolution) is 4 GHz which is outside the range of low-frequency through-the-wall systems. To remain in the low-frequency UHF band and still detect such small movements, a single-tone frequency is needed. [6]

Several researchers have demonstrated the detection of physiological signals in a through-the-wall scenario. Bugaev [10] measured the pulse rate and breathing rate of a human subject behind a wall with a 2-GHz system. Bugaev was able to show the increase in pulse rate due to the subject holding his breath for an extended period of time thus experiencing oxygen starvation. Additionally, Bugaev showed that the amplitude of breathing is much greater than that of the heart rate. Movements of the body during speech were also recorded, and the possibility of speech recognition via radar was indicated.

One technology field tested by 2000 was the RADAR Flashlight, developed by the Georgia Tech Research Institute as the descendant of the RVSM systems that measured Olympic athletes. The system detects both body movement and the breathing of subjects behind walls and other barriers, and was intended primarily for law en-

forcement applications. The detection of involuntary respiration of subjects hidden behind doors and walls during search scenarios is critical when the subject can not be depended upon to voluntarily move, or in hostage situations when the subject may be prevented from moving. Early versions of this system operated at 24.1 GHz; the more recent prototype operated at 10.525 GHz. [11]

Using the HHT processing approach described earlier, Narayanan [3] and Lai [6] employed an UWB noise wave form concealing a single 2-GHz tone in order to measure the expansion and contraction of the chest cavity in breathing. The IMFs corresponding to the Doppler frequency associated with human breathing were isolated and were also used to distinguish cases when no human was present.

The HHT process may lend itself well to classification of human movements and activity, provided enough measurements are taken. This concept, and others, will be described in the next section.

2.3 Human Classification

Human classification involves the discrimination between different types of people, based on various parameters, such as gender, age, or even activities being performed. Additional classification efforts involve discrimination between humans, animals, and vehicles. Discrimination via radar is mainly intended to address the challenging question of determining human intent, so that accurate decisions may be based on this information. Radar discrimination itself can be a difficult problem, because of the need for a high signal-to-noise ratio in order to resolve what may be small differences that characterize the desired classification scheme. For example, Gürbüz [29] demonstrated a method of gender discrimination by extracting the thigh height from cadence frequency plots derived from radar human spectrograms and employing a Neyman-Pearson detector based on statistical human dimensions to classify the

person as male or female. This technique suffers, however, from the inaccuracies inherent in noisy spectrograms and cadence frequency plots.

Although this thesis will employ an age-based classifier to discriminate between children and adults, movement-based classification is presented here, due to its relevancy to the through-wall human detection problem.

Movement-Based Classification

Otero [16] developed a binary classification system, extracting features from the cadence frequency plot of human spectrograms, in order to discriminate between situations when a walking human was present, and when no one was present. The correct classification rate was 88%, with no false alarms seen. Due to the significant spectrogram differences between a human's two-legged gait and an animal's four-legged gait, Otero was able to discriminate humans from animals. Such a multi-class classifier, which can determine both the presence of a human, and distinguish human signatures from those of animals, may be very useful in applications of security and perimeter protection.

In addition to species differences, human radar spectrograms display noticeable differences due to changes in movement and walking pattern of the subject. Ram [2], using the RJTF transform, demonstrated such differences in a human carrying a variety of objects: a corner reflector, metal box, and metal pole. Contributions from the reflector and pole are seen in the spectrogram, as well as an altered walking pattern due to the person carrying the box in both hands.

Kim [19] studied the spectrograms of seven human activities — running, walking, walking with a stick, crawling, boxing in place and while moving forward, and sitting — in order to build a classifier to distinguish among them. A 2.4-GHz, line-of-sight radar system was used, and six features extracted from the spectrogram of

each movement to be processed with the classifier. Although the classifier could process the entire spectrogram itself, such a method results in high-dimensional data, a complex internal structure of the classifier, and a long training process. Paring the data down to a subset of correctly chosen features, however, significantly reduces the data dimensions while still maintaining the important characteristics of the spectrogram. Each of the chosen features, such as torso Doppler frequency, total bandwidth, and Doppler offset, was identified with a specific characteristic of the motion of the human. A Support Vector Machine (SVM), a type of binary classifier to be described in greater detail in Chapter IV, was used together with a decision tree to classify the spectrograms. Further analysis found that only four of the features were necessary for classification accuracy above 90%. Researchers also tested a sequence of activities with classification errors arising in the transition between activities, as expected. Through-wall measurements were briefly investigated with the finding that the signal-to-noise ratio suffered and that micro-Doppler movements were much more difficult to identify, particularly as the human subject moved further away from the radar. Kim indicates, however, that improved hardware may result in significant signal improvements.

A second effort using SVM classification was carried out by Fairchild [24], this time using HHT analysis and the EMD algorithm to extract features from human micro-Doppler signals for classification. Fairchild used a 750-MHz radar system, with human subjects placed behind a wall. The SVM was paired with a one-against-all method in order to handle multi-class classification. Six classes were identified: noise or no subject, breathing or holding breath, swinging arms, picking up an object, standing from a crouch, and miscellaneous movements. It was shown that the energy distribution over the signal's IMF components was unique to specific movements, and an average classification accuracy of 83% was obtained.

The work detailed above demonstrates successes in classification of human presence and activity. This thesis will add another component to the radar classification problem: child-adult discrimination, which will provide further information about potential situations within a building.

III. Previous Work

This chapter describes the research that provides the project's foundation. An effort in age-based classification based on anthropometric measurements is briefly discussed, followed by precursor work to this thesis. The development of the Miranda human cylinder-sphere model is described, as adapted to this project. The Miranda human scattering model will be explained in Chapter V after supporting background is presented.

3.1 Age-Based Classification

Although efforts at discriminating adults from children via radar analysis are relatively recent, there has been work to accomplish age-based discrimination using other methods. This section describes efforts by Bowden [30] to develop a classification model based on anthropometric measurements.

There is a difficulty in obtaining data on children. In research ethics law, children are a protected population, so there is limited existing research data available, and new data is difficult to obtain. Bowden found only one public domain database of child anthropometric data, a 1977 study called "Anthropometry of Infants, Children, and Youths to Age 18 for Product Safety Design", provided by the National Institute of Standards and Technology. [30]

The classification scheme in [30] targeted three groups: subjects under 96 months of age, those between 96 and 144 months, and those over 144 months. A variety of anthropometric measurements were used to develop a multiple linear regression equation to determine group recognition rates. The equation coefficients were determined via sigma-plot software, and custom Labview software determined the rates.

The regression was originally carried out with all seventeen anthropometric mea-

surements available. From these seventeen, two were identified as providing the bulk of the accuracy in the multiple linear regression, with little gained by the addition of the other variables. These two measurements were femur length and skull length. In the dataset consisting of both the 1977 data and supplemental data from subjects 18 to 79 years of age, the accuracy of the regression in the two-variable case was about 91%. A similar experiment was done involving only two groups, divided at age 144 months. The two-variable regression accuracy for the two groups was about 96%. The multiple linear regression model developed to achieve this two-group accuracy was [30]

$$\text{Age Group} = 0.391 + 0.00400F_L - 0.00459H_L \tag{3}$$

where F_L is the femur length (buttock to knee length as given in the report), and H_L is the length of the head. An investigation into noise added to the measurements indicated that accuracy does not begin to fall significantly until 4-8 cm of measurement error is reached, indicating that classification based on reasonably accurate measurement data can be fairly robust.

3.2 Small Human Discrimination

In [1, 12], Miranda developed an analytical radar scattering model of a human and conducted a series of radar scattering measurements to verify the model. The model consisted of an arrangement of spheres and cylinders representing a simplified human form. This section details the results of Miranda's 2012 experiments and describes her human cylinder-sphere model and electromagnetic scattering model.

The experiments involved the radar measurements of two objects, dielectrically similar to humans, referred to as "Green Man" (162 cm tall) and "Timmy" (84 cm) in the plots. Both human surrogates were filled with a compound that simulates a combination of muscle and fat in order to mimic the dielectric properties of humans.

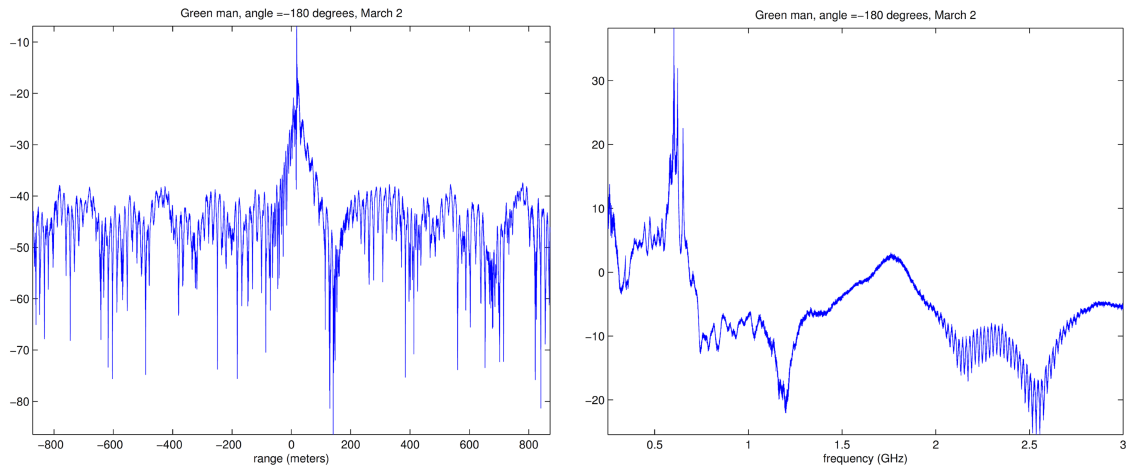

Figure 3. Radar Scattering from an Adult ("Green Man") Substitute (reproduced from [31]). Scattering amplitude in the range domain is displayed on the left; frequency domain on the right. The wide peak in the center of the range domain indicates the adult substitute — it is a much broader peak than that of the child substitute (Figure 4). The resonance region of the human substitute, 500-750 MHz, is displayed in the plot on the right.

These objects were measured with a radar system operating at a frequency range of 250 MHz to 3 GHz. Measurements were taken at two elevation angles and multiple azimuth angles. Characteristic measurement results are shown in Figures 3 and 4 [31]. The first figure displays the measurements for the adult "Green Man" in the range and frequency domains, while the second displays the same domains for the child "Timmy."

In comparing the sets of plots for the adult and child substitutes, note that, in the range domain, the radar return for the adult substitute is broader, and the noise floor tends to be higher. The child substitute, on the other hand, has a much narrower return, and the shape is less distinguishable. In the frequency domain, a resonance is seen for both objects at about 500-750 MHz. This resonance region is worth noting, because this thesis is concerned with radar frequencies of that range.

To further characterize radar scattering from adults and children, both human surrogate models were digitally scanned to obtain their geometries in order to perform

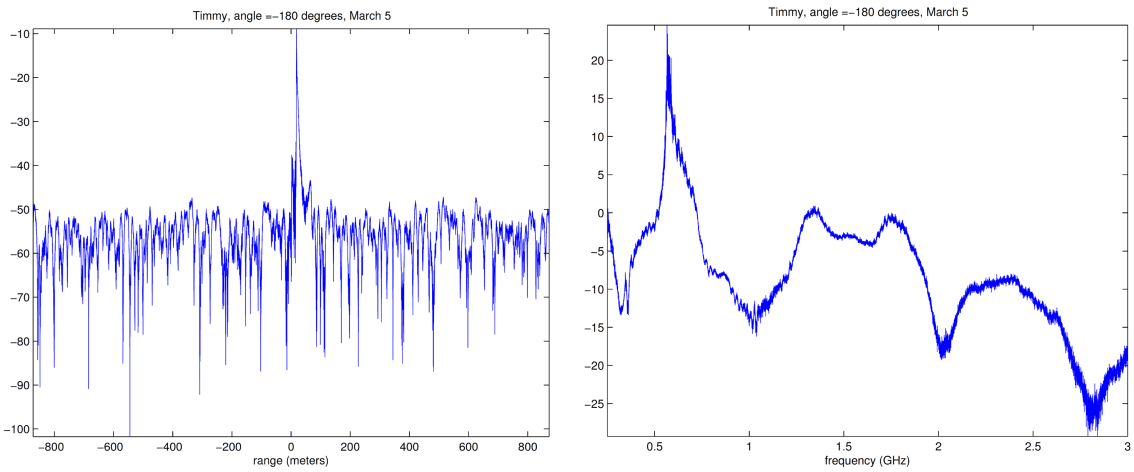

Figure 4. Radar Scattering from a Child ("Timmy") Substitute (reproduced from [31]). Scattering amplitude in the range domain is displayed on the left; frequency domain on the right. The narrow peak in the center of the range domain indicates the child substitute. The resonance region of the substitute, 500-750 MHz, is displayed in the plot on the right.

numerical backscattering radar cross-section (RCS) simulations. The simulations were carried out by Monopole Research located in California. These simulations demonstrated elevation, azimuth, polarization, and frequency dependence of the RCS for both the adult and child substitutes. Although elevation and radar polarization are not tested in this thesis, the results are applicable to the overall problem of child-adult discrimination. An example [32] of angular dependence of the RCS for vertical polarization, displayed as cross-section domes, is shown in Figure 5. Only the results for 0.5, 1.5, and 3.0 GHz are displayed.

To interpret these plots, the images can be viewed as if the object of interest is observed from above, with a dome placed over the object. The relative value of the RCS is then projected on this dome. Azimuth angles are plotted counterclockwise around the dome, while elevation angles are plotted from the perimeter, at 5.5°, toward the center, ending at 45.5° elevation. From these plots, note that the RCS of both objects increases with frequency. More interesting, however, is how the RCS of the adult and child substitutes differ. In general, the child substitute has a RCS approximately 5

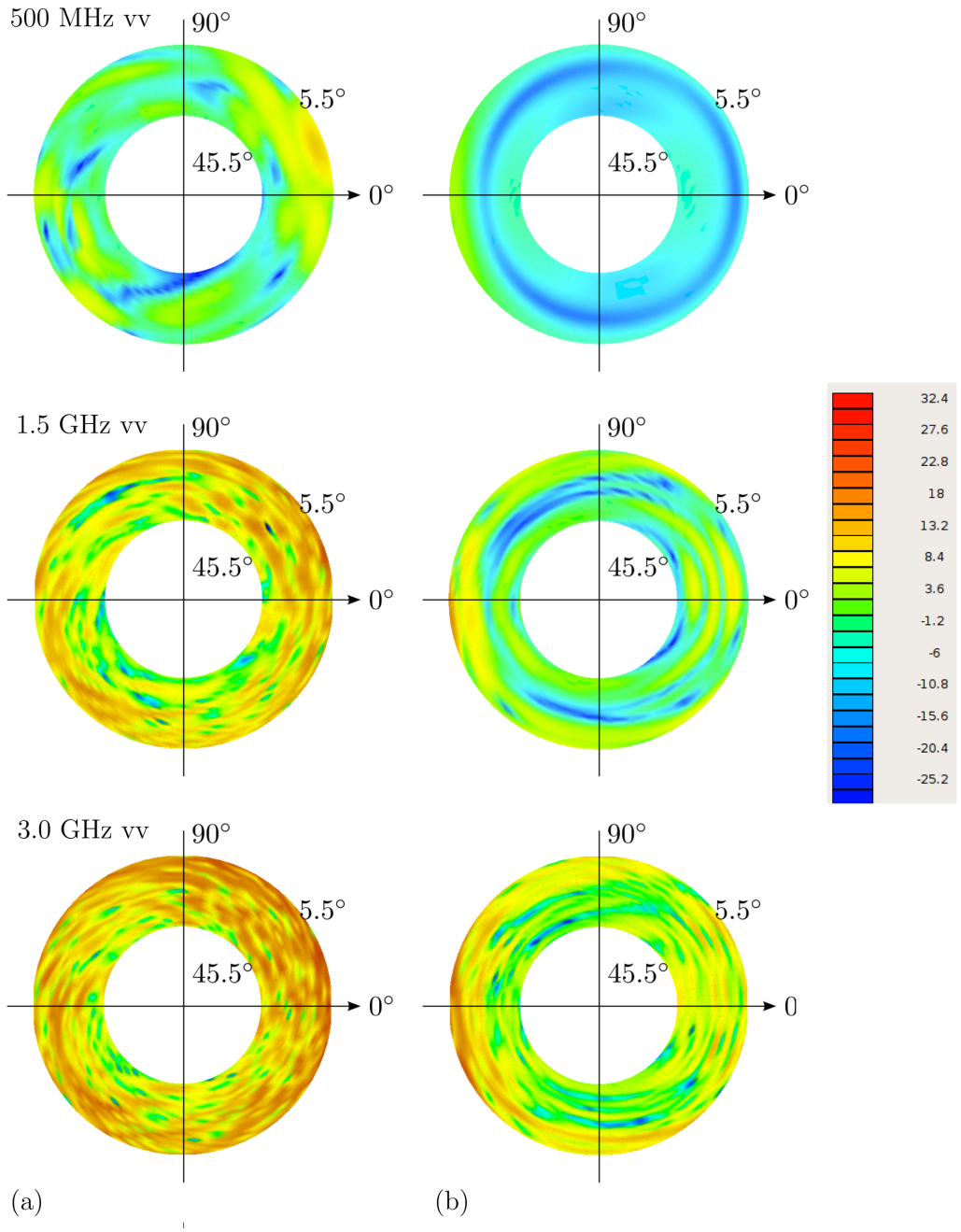

Figure 5. Radar Cross Section Domes of Adult and Child Human Substitutes (reproduced from [32]). Adult RCS "partial domes" for selected radar frequencies are displayed on the left (a); child RCS domes are displayed on the right (b). VV polarization is used. Azimuth angles are plotted counterclockwise from 0° to 360°, while elevation angles increase from the perimeter to the center of each dome, over a range of 5.5° to 45.5°. The colorbar scale displays RCS magnitude in dB. The RCS of both objects increase with frequency, though the adult substitute's RCS is much higher, with the difference between the child and adult RCS greater at lower frequencies. The adult substitute's RCS also has a greater oscillatory structure across the angular range than does the child substitute.

dB lower than the adult substitute at high frequencies, with the difference increasing toward low frequencies. The difference is more visible in comparing the upper and lower plots of Figure 6. Additionally, there are fewer oscillations of the RCS across the angular range for the child substitute than the adult substitute (best seen in Figure 5 at 1.5 GHz), and the adult substitute RCS appears to display more structure with regard to frequency than the child substitute (Figure 6). Note, that in Figure 5, the location of the maximum cross-sections, near azimuth 20° for the adult substitute and azimuth 185° for the child substitute, are *not* due to a fundamental difference in the objects themselves. They are due to the inconsistent rotation of the scanned computer models of the objects: the adult substitute was rotated counterclockwise about 20° and tilted slightly backward, while the child substitute was rotated counterclockwise about 5° and tilted slightly forward [32]. Given the slight tilt and the highest RCS on the perimeter near 5.5° elevation, it is seen that the highest scattering from a human substitute occurs when the full silhouette of the object of interest is presented to the radar.

The results of this project indicate a stronger frequency dependence in the RCS for the child substitute than the adult substitute (Figure 6) and stronger VV than HH scattering at low frequencies. Discrimination between the two objects of interest may thus be best accomplished by considering the difference in magnitude and frequency dependence of the RCS, or in the difference, particularly at low frequencies, in the horizontal and vertical polarization RCS. [32]

These results can be explained by noting that the heights of the objects (162 cm for the adult "Green Man" and 84 cm for the child "Timmy"), in the measured wavelength range of 10-100 cm, fall within the transition region between low-frequency Rayleigh scattering and high-frequency geometrical scattering regions. At low frequencies, the Rayleigh-scattering RCS integrated over the angles behaves as $\sim f^4$,

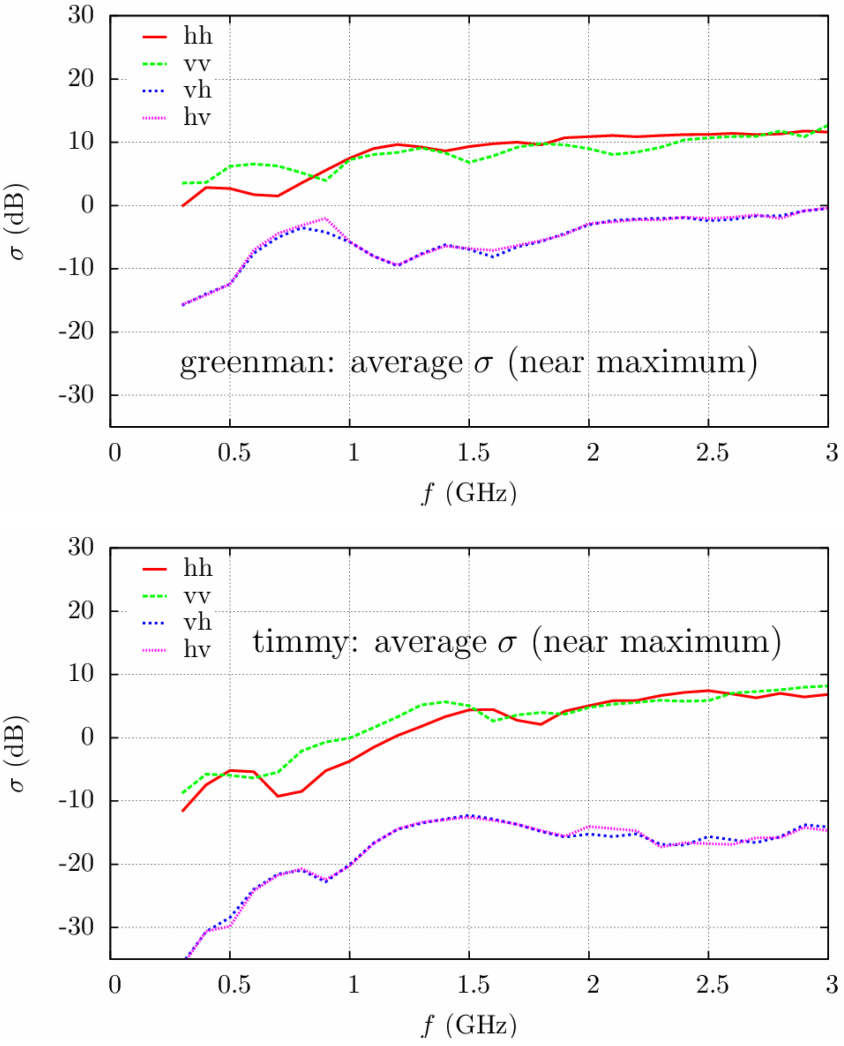

Figure 6. Frequency Dependence of the RCS of Adult ("Greenman") and Child ("Timmy") Human Substitutes (reproduced from [32]). Frequency is plotted along the horizontal azis; RCS (σ) on the vertical. The plot displays RCS averaged over a small angular range near the maximum values of the RCS (as an illustration, consider the lowest pair of plots in Figure 5, near azimuth 20° for (a) and azimuth 185° for (b), where the maximum values lie). The lines show results for different polarizations — v indicating vertical, and h indicating horizontal. The cross-polarization RCS are much smaller, and are of less interest. The adult substitute's RCS shows more structure than that of the child, which is due to the angular distiribution of the RCS changing with frequency, as in Figure 5 [32].

leading to a large frequency dependence, particularly for the child substitute, which is affected more by Rayleigh scattering at low frequencies than is the adult substitute. Within this transition regime, the RCS is approximately proportional to the volume of the object of interest at low frequencies, but proportional to the object's surface area at high frequencies. The transition between Rayleigh and geometrical scattering will take place at a wavelength proportional to the object's size. Additionally, at low frequencies and wavelengths near the object's size, a vertically-oriented elongated volume appears as an electric dipole, producing a larger radar return and a higher RCS for vertical polarization than for horizontal. These observations are consistent with the results of the project. [32]

3.3 Miranda Human Model

The Miranda human cylinder-sphere model is based on the work of Sarabandi [14]. The model (Figure 7) consists of a prolate sphere and a pair of cylinders. At the range of wavelengths this thesis is concerned with (0.375–0.75 m), the wavelengths can penetrate deeper into the body than just the skin; this model is thus concerned with the scattering from bone rather than skin, and the resonances that originate in the ribcage area at these frequencies [1]. The prolate sphere represents the skull of a human while the horizontal, middle cylinder represents the ribcage, with the outward curve of the cylinder mirroring the outward curve of the human ribcage, seen from the side, and the ends of the cylinder extending to include the upper arms on either side of the ribcage. The horizontal cylinder does not include the abdomen or shoulders, since the bone structures of these areas do not fit the design of the model. The vertical cylinder represents the thighs/femurs of a human with legs placed together, excluding the hips and knee caps.

For our discussion, let the first cylinder be the middle, horizontal volume desig-

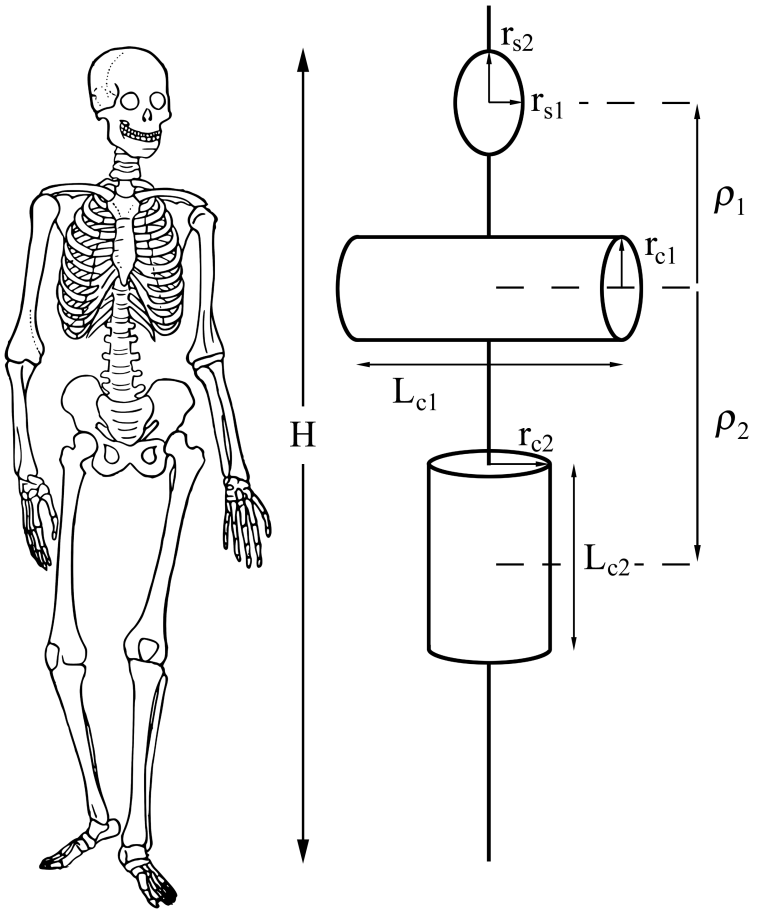

Figure 7. Miranda Human Model. In the Miranda Cylinder-Sphere Human Model, a prolate spheroid represents the skull of a human, a horizontal cylinder represents the ribcage area, and a vertical cylinder represents the thighs of a human with legs together. The major and minor radii of the spheroid are r_{s2} and r_{s1}, respectively. The radius and length of the horizontal cylinder are r_{c1} and L_{c1}, and those of the vertical cylinder are r_{c2} and L_{c2}. The perpendicular distance from the horizontal axis of cylinder 1 to the center of the spheroid is ρ_1; the perpendicular distance from the same axis to the center of cylinder 2 is ρ_2. The parameters r_{s2}, r_{s1} (head size) and ρ_1, ρ_2 (body length) effectively determine the sizes of the cylinders. The model is also wavelength-dependent. The diagram here depicts an acceptable scale model for a wavelength of $\lambda = 0.5625$ m and an average human height of $H = 1.7526$ m (5 ft, 9 in).

nated by radius r_{c1} and length L_{c1}. Let the second cylinder be the lower, vertical volume designated by radius r_{c2} and length L_{c2}. The prolate sphere is the topmost volume designated by minor radius r_{s1} and major radius r_{s2}. These dimensions are illustrated in Figure 7.

Now, an approximate analytical electromagnetic scattering solution from a cylinder-sphere pair (or a cylinder and a second arbitrary scatterer, such as a second cylinder) exists, if the following dimensional conditions are obeyed [14]:

$$\rho > \frac{2r_s^2}{\lambda}, \qquad \frac{L_c^2}{\lambda} \geq \rho > \frac{2r_c^2}{\lambda} \tag{4}$$

where ρ is the perpendicular distance from the axis of the first cylinder to the center of the adjacent object (either the sphere or second cylinder, in this case), L_c is the length of the first cylinder, r_c is the radius of the first cylinder, and r_s is the radius of the sphere or characteristic dimension of the second object. The equation on the left places the first cylinder in the far-field region of the adjacent object. The equation on the right places the adjacent object in the near-field of the first cylinder with respect to the cylinder's length, and in the far-field with respect to the cylinder's radius.

In the case of the Miranda human model, we obtain two sets of equations from (4). The first set applies to the horizontal cylinder and the prolate sphere:

$$\begin{gathered} \rho_1 > \tfrac{2r_{s1}^2}{\lambda}, \qquad \rho_1 > \tfrac{2r_{s2}^2}{\lambda} \\ \tfrac{L_{c1}^2}{\lambda} \geq \rho_1 > \tfrac{2r_{c1}^2}{\lambda} \end{gathered} \tag{5}$$

where r_{s1} and r_{s2} are the minor and major radii of the prolate sphere, respectively; L_{c1} and r_{c1} are the length and radius of the horizontal cylinder; and ρ_1 is the perpendicular distance from the axis of the horizontal cylinder to the center of the prolate sphere. Similarly, the second set of equations, which applies to the horizontal and vertical

cylinders is

$$\begin{gathered} \rho_2 > \frac{2r_{c2}^2}{\lambda}, \qquad \rho_2 > \frac{2L_{c2}^2}{\lambda} \\ \frac{L_{c1}^2}{\lambda} \geq \rho_2 > \frac{2r_{c1}^2}{\lambda} \end{gathered} \tag{6}$$

where r_{c2} and L_{c2} are the radius and length of the vertical cylinder, and ρ_2 is the perpendicular distance from the axis of the horizontal cylinder to the center of the vertical cylinder. Both sets of equations, (5) and (6), must be satisfied.

This model is not only wavelength-dependent but also dependent on the size of the human one chooses to model, as all dimensions must be representative of the dimensions of a realistic human. To determine proper dimensions, the dimensions of the head, r_{s1} and r_{s2}, serve as the best anchor points, as the size of an adult human head is relatively constant. Note that ρ_1 and ρ_2 will always be equal to some constant length dependent on the size of the human model:

$$\rho_1 + \rho_2 = C \tag{7}$$

With these restrictions in place, we can determine maximum and minimum sizes for the radii and lengths of the cylinders and further narrow down the dimensions with respect to what is appropriate for a human of the size we have chosen to model. For a range of wavelengths, λ_{min} to λ_{max}, an appropriate ρ_1 and ρ_2 chosen based on the constant C, and r_{s1}, r_{s2} known, the maximum r_{c1} becomes the lesser of

$$r_{c1,max} = \sqrt{\frac{\lambda_{min} * \rho_1}{2}} \qquad \text{or} \qquad r_{c1,max} = \sqrt{\frac{\lambda_{min} * \rho_2}{2}} \tag{8}$$

the minimum L_{c1} becomes the greater of

$$L_{c1,min} = \sqrt{\lambda_{max} * \rho_1} \qquad \text{or} \qquad L_{c1,min} = \sqrt{\lambda_{max} * \rho_2} \tag{9}$$

and the maximum r_{c2} and L_{c2} are

$$r_{c2,max} = \sqrt{\frac{\lambda_{min} * \rho_2}{2}}, \qquad L_{c2,max} = \sqrt{\frac{\lambda_{min} * \rho_2}{2}} \tag{10}$$

Limitations of the Model

In practice, the limiting dimension is L_{c1}, and, to a lesser extent, L_{c2}. Realistically, ρ_1 will be less than ρ_2, but a longer ρ_2 will drive up the length of cylinder 1 until the model breaks and becomes unrepresentative of a human. A longer wavelength will also increase the length of cylinder 1. Thus, a balance must be struck between ρ_1, ρ_2 and λ_{max}. When ρ_1 and ρ_2 are limited by the dimensions of the human body, an upper limit is placed on wavelength λ_{max}.

The model created for this thesis is based on the dimensions of an average human, 1.7526 m (5 ft, 9 in) tall. The distance between the center of the head and the midpoint on the thigh, C, was estimated to be 0.98 m. Taking into account the wavelength, subject height, and dimension C, and targeting ρ_1 to locate the center of the horizonal cylinder roughly in the center of the ribcage, we arrived at the following model dimensions:

Table 1. Miranda Human Model Chosen Values

$\lambda = 0.5625$ m $H = 1.7526$ m (5 ft, 9 in), $C = 0.98$ m		
Parameter	**Value**	
	(m)	**(in)**
r_{s1}	0.0762	3
r_{s2}	0.1143	4.5
ρ_1	0.4	15.75
ρ_2	0.578	22.76
r_{c1}	0.1143	4.5
L_{c1}	0.5702	22.45
r_{c2}	0.1345	5.3
L_{c2}	0.4022	15.83

Table 1 and the guidelines for arriving at these values represent our contributions to the Miranda human cylinder-sphere model. In investigating the magnitudes of the parameters for various wavelengths, we found that the upper limit on the wavelength for a realistic 5-ft, 9-in human was roughly the midpoint of our range, $\lambda = 0.5625$ m. This wavelength puts the minimum L_{c1} at 0.57 m, and the maximum L_{c2} at 0.40 m. The minimum L_{c1} is just within a realistic limit, if our subject is holding the arms slightly apart from the sides of the body, as if working on some task. Conversely, the lower limit on the wavelength for a human of the same size is about 0.32 m. Although this lower limit sets the minimum L_{c1} at a more comfortable length, the maximum L_{c2} is now at 0.304 m (roughly 1 ft), which is at the lower boundary of what might be seen as a realistic thigh length, according to U.S. anthropometric data [33]. Other populations may have alternate boundaries.

Thus, for an average human height, the Miranda cylinder-sphere human model is limited to a wavelength range of about 0.32–0.56 m, which corresponds to the resonance region of the human body, as seen in Section 3.2.

This chapter has discussed prior work in determining the dependence of a human age-based classifier upon two primary anthropometric dimensions: femur length and head length (Equation (3)). We have also described precursor work of radar-based, child-adult discrimination, as well as the development of the Miranda human cylinder-sphere model. The Miranda human model is based on Equation (4). Our contribution to the Miranda human model is the adaption of the model to an average adult male of 1.7526 m (5 ft, 9 in), and the identification of appropriate representative dimensions of the three volumes that comprise the model.

IV. Theory

This chapter presents the theoretical background for the concepts addressed in this paper. The first section describes the radar range equation as a brief introduction to radar concepts, followed by the derivation of the scattered field from a dielectric object which provides the basis for the Miranda scattering model and our multipath expansion. Further background material, the fundamental development of the scattered field representation, beginning with the wave equation, and the Support Vector Machine as our classification method are developed in Appendices A and B.

4.1 Radar Range Equation

The radar equation is a fundamental model used in the design of radar systems. It relates the main components of the radar — the transmitter, receiver, and antenna — to the object of interest and surrounding environment, in order to determine the maximum range of the radar system. The radar equation not only calculates maximum range, but also various parameters affecting system performance. Using this equation, a radar system designer balances the performance of the radar with the design constraints imposed by the system, with the goal of optimizing the system within given parameters. [34]

For background we shall present the derivation of the radar equation as seen in Skolnik's *Introduction to Radar Systems* [34]. To develop the radar equation, we first consider the simplest case of the isotropic antenna which radiates uniformly in all directions. The power transmitted by the antenna is P_t, and the radial distance from source to observer is R. The power density at some distance R is then the total radiated power divided by the surface area of a sphere with radius equal to that

distance:

$$\Phi_{iso} = \frac{P_t}{4\pi R^2} \tag{11}$$

A directive antenna, however, does not radiate in all directions equally but rather concentrates the radiated power P_t in one direction. The equation for an isotropic antenna is then modified by the antenna gain:

$$G_t = \frac{\text{maximum power density radiated by a directive antenna}}{\text{power density radiated by a lossless isotropic antenna with the same power input}} \tag{12}$$

Antenna gain is a measure of the increased power density radiated in one direction as compared to that from an isotropic antenna. We now have the equation for a directive antenna:

$$\Phi_{trans} = \frac{P_t G_t}{4\pi R^2} \tag{13}$$

Now, place an object in the field of the antenna. Only a portion of the energy radiated by the antenna will be intercepted by the object of interest. Since the intercepted energy will then be reradiated in many directions, only a portion of the intercepted energy will return to the receiver. The radar cross section (RCS) of the object is dependent upon the incident power density and determines the power density returned to the receiver. The RCS corresponds to the effective area that intercepts the radiated power and scatters it isotropically. Given an RCS σ, the reflected power is:

$$P_{ref} = \Phi_{trans}\sigma = \frac{P_t G_t}{4\pi R^2}\sigma \tag{14}$$

The power scattered by the object is again reduced by the surface area of a sphere to determine the power density at the receiver distance:

$$\Phi_{rec} = \frac{P_{ref}}{4\pi R^2} = \frac{P_t G_t \sigma}{(4\pi)^2 R^4} \tag{15}$$

Finally, the receiving antenna will only capture a portion of the scattered energy incident upon it. The received signal power P_r is:

$$P_r = \Phi_{rec} A_e = \frac{P_t G_t}{4\pi R^2} \frac{\sigma}{4\pi R^2} A_e \tag{16}$$

where A_e is the effective area of the receiving antenna, given by $A_e = \rho_a A$; A is the physical area of the antenna and ρ_a is the aperture efficiency. If this equation is solved for R, the maximum range R_{max} is given when P_r equals the minimum detectable signal $P_{r,min}$. Then we obtain the radar range equation:

$$R_{max} = \left[\frac{P_t G_t \sigma A_e}{(4\pi)^2 P_{r,min}} \right]^{\frac{1}{4}} \tag{17}$$

Antenna gain is related to the effective area of the antenna by:

$$G = \frac{4\pi A_e}{\lambda^2} \tag{18}$$

where λ is the wavelength. With this expression in mind, the radar equation can be rewritten to incorporate the gain of the receiving antenna in place of its effective area:

$$R_{max} = \left[\frac{P_t G_t G_r \lambda^2 \sigma}{(4\pi)^3 P_{r,min}} \right]^{\frac{1}{4}} \tag{19}$$

where G_t and G_r are the transmitting and receiving gains, respectively.

Equations (17) and (19) are two different versions of the simple, or fundamental, form of the radar range equation. They do not completely describe the performance of real radar systems, where other phenomena come into play, such as propagation factors, atmospheric attenuation, receiver noise, and various losses and efficiencies. The radar equation can also be modified to suit other radars, like continuous wave and pulse Doppler radar, as well as specific radar applications, such as surveillance,

tracking, synthetic aperture, and HF over-the-horizon radars. In general, the simple form of the radar equation predicts an upper value of range up to a factor of two or more greater than the true value. However, it remains useful in determining how different parameters will affect the maximum range of the radar, particularly when additional terms are considered. [34]

4.2 Scattered Fields: Derivation

This section builds a representation of the scattered field from a dielectric object, following the method in Yeh [13]. Additional material that provides a necessary background to this section may be found in Appendix A.

First, the scattered fields due to the sources $\overline{J}_+$ (electric surface current) and $\overline{M}_+$ (magnetic surface current) are represented in terms of the vector potentials $\overline{A}$ and $\overline{F}$, as in [13]:

$$\overline{E}^s = -\nabla \times \overline{F} - \frac{1}{i\omega\epsilon_0}(\nabla \times \nabla \times \overline{A}) \tag{20}$$

$$\overline{H}^s = -\nabla \times \overline{A} - \frac{1}{i\omega\mu_0}(\nabla \times \nabla \times \overline{F}) \tag{21}$$

where

$$\overline{A} = \frac{1}{4\pi}\int_S \frac{\overline{J}_+ e^{ik\left|\overline{r}-\overline{r}'\right|}}{\left|\overline{r}-\overline{r}'\right|} dS \tag{22}$$

$$\overline{F} = \frac{1}{4\pi}\int_S \frac{\overline{M}_+ e^{ik\left|\overline{r}-\overline{r}'\right|}}{\left|\overline{r}-\overline{r}'\right|} dS \tag{23}$$

$\overline{J}_+$ and $\overline{M}_+$ are given by (151) and (152), $\overline{r}$ is the position vector from the origin (internal to S) to a field point, $\overline{r}'$ is the vector from the origin to the source, and wavenumber $k = 2\pi/\lambda$. In the following derivation drawn from [13], the time variation $e^{-i\omega t}$ is assumed for simplicity, as is assumed for the derivation in Appendix A, Section

1.2. Substituting (22) and (23) into (20) gives [13]

$$\overline{E}^s(\overline{r}) = -\nabla\times\frac{1}{4\pi}\int_S \frac{(\overline{E}_+ \times \hat{n})e^{ik\left|\overline{r}-\overline{r}'\right|}}{\left|\overline{r}-\overline{r}'\right|}dS - \frac{1}{i\omega\epsilon_0}\left(\nabla\times\nabla\times\frac{1}{4\pi}\int_S \frac{(\hat{n}\times\overline{H}_+)e^{ik\left|\overline{r}-\overline{r}'\right|}}{\left|\overline{r}-\overline{r}'\right|}dS\right) \tag{24}$$

Applying $\overline{A}\times\overline{B} = -\overline{B}\times\overline{A}$, and substituting $R = \left|\overline{r}-\overline{r}'\right|$, followed by the free space Green's function $g(kR) = e^{ikR}/(4\pi R)$, results in [13]

$$\overline{E}^s(\overline{r}) = \nabla\times\int_S \left(\hat{n}\times\overline{E}_+\right) g(kR)dS - \nabla\times\nabla\times\frac{1}{i\omega\epsilon_0}\int_S(\hat{n}\times\overline{H}_+)g(kR)dS \tag{25}$$

The expression for the total electric field is then

$$\overline{E}^i(\overline{r}) + \overline{E}^s(\overline{r}) = \begin{cases} \overline{E}_{tot}(\overline{r}) & \text{for } \overline{r} \text{ outside } S \\ 0 & \text{for } \overline{r} \text{ inside } S \end{cases} \tag{26}$$

Equation (26) demonstrates the Equivalence Principal. We see that, inside S, the scattered field must cancel the incident field, and [13]

$$-\overline{E}^i(\overline{r}) = \overline{E}^s(\overline{r}) = \nabla\times\int_S \left(\hat{n}\times\overline{E}_+\right) g(kR)dS - \nabla\times\nabla\times\frac{1}{i\omega\epsilon_0}\int_S(\hat{n}\times\overline{H}_+)g(kR)dS \tag{27}$$

Now we can make use of the results from Appendix A, Sections 1.2 and 1.3. As in 1.2, the incident electric field can be represented by

$$\overline{E}^i(\overline{r}) = \sum_{nm} D_{nm}(a_{nm}\overline{M}^{(1)}_{nm}(k\overline{r}) + b_{nm}\overline{N}^{(1)}_{nm}(k\overline{r})) \tag{28}$$

where D_{nm} is a normalization constant, and a_{nm}, b_{nm} are expansion coefficients. $\overline{M}_{nm}$ and $\overline{N}_{nm}$ are given by

$$\overline{M}_{nm}(k\overline{r}) = \nabla\times\overline{r}\Psi_{nm} \tag{29}$$

$$\overline{N}_{nm}(k\overline{r}) = \frac{1}{k}\nabla \times \overline{M}_{nm}(k\overline{r}) \tag{30}$$

with

$$\Psi_{nm} = f(r,\theta,\phi)e^{-i\omega t} \tag{31}$$

$$f(r,\theta,\phi) = \sum_{n=0}^{\infty} z_n(kr)\left[a_{n0}P_n(\cos\theta) + \sum_{m=1}^{n}(a_{nm}\cos m\phi + b_{nm}\sin m\phi)P_n^m(\cos\theta)\right] \tag{32}$$

as in (144). The transform $P_n^m(\cos\theta)$ is the associated Legendre function, and $z_n(kr)$ is a spherical Bessel function. Inside S, where solutions must be finite at $\overline{r} = 0$, we use Bessel functions of the first kind: $z_n(kr) = j_n(kR)$ and where $j_n(kr)$ is given by (142). These solutions of the first kind are denoted by the superscript 1 in (28). Outside S, where solutions must describe outgoing waves, the solutions involve spherical Bessel functions of the third kind: $z_n(kr) = h_n^{(1)}(kr) = j_n(kr) + in_n(kr)$ (given by (142) and (143)). Solutions of this type will be denoted by the superscript 3. The normalization constant is [13]

$$D_{nm} = \epsilon_m \frac{(2n+1)\,(n-m)!}{4n(n+1)(n+m)!}, \epsilon_m = \begin{cases} 1 & \text{if } m = 0 \\ 2 & \text{if } m > 0 \end{cases} \tag{33}$$

and, since we assume the incident field is a plane wave, we can use the expansion coefficients for a plane wave as given by Stratton [35] (note that these coefficients are *not* presented in [13]):

$$a_n = \frac{2n+1}{n(n+1)}i^n \tag{34}$$

$$b_n = -i^{n+1}\frac{2n+1}{n(n+1)} \tag{35}$$

However, these coefficients are those appropriate for the expression for the field in Equation (123). Because Equation (28) contains the constant D_{nm}, we must find the new representation of the expansion coefficients, and do so simply by dividing

Stratton's equations by D_{nm}:

$$a_{nm} = \frac{a_n}{D_{nm}} = \frac{i^n}{\epsilon_m}\frac{4(n+m)!}{(n-m)!} \tag{36}$$

$$b_{nm} = \frac{b_n}{D_{nm}} = \frac{-i^{n+1}}{\epsilon_m}\frac{4(n+m)!}{(n-m)!} \tag{37}$$

The right side of Equation (27) can be expanded in the following terms [13]:

$$(\hat{n} \times \overline{E}_+)g(kR) = (\hat{n} \times \overline{E}_+) \cdot \overline{\overline{\mathcal{G}}} \tag{38}$$

$$(\hat{n} \times \overline{H}_+)g(kR) = (\hat{n} \times \overline{H}_+) \cdot \overline{\overline{\mathcal{G}}} \tag{39}$$

where $\overline{\overline{\mathcal{G}}}(kR)$ is the free space Green's dyadic [13]

$$\overline{\overline{\mathcal{G}}}(kR) = \frac{ik}{\pi}\sum_{nm} D_{nm}[\overline{M}^{(3)}_{nm}(k\overline{r}_>)\overline{M}^{(1)}_{nm}(k\overline{r}_<) + \overline{N}^{(3)}_{nm}(k\overline{r}_>)\overline{N}^{(1)}_{nm}(k\overline{r}_<)] \tag{40}$$

where $\overline{r}_>$ is the greater of $\overline{r}$ and $\overline{r}^{'}$, and $\overline{r}_<$ is the lesser. As mentioned before, the superscript 3 indicates the presence of spherical Bessel functions of the third kind.

Now, the expansions (28), (38), and (39) can be substituted back into Equation (27). As stated in [13], these equations converge for all r inside S, so this expansion of (27) is valid inside S. Applying this substitution, and carrying out the repeated curl operations $\nabla \times \overline{M} = k\overline{N}$ and $\nabla \times \overline{N} = k\overline{M}$, we get

$$\begin{aligned}
&-\sum_{nm} D_{nm}[a_{nm}\overline{M}^{(1)}_{nm}(k\overline{r}) + b_{nm}\overline{N}^{(1)}_{nm}(k\overline{r})] \\
&\quad = \frac{ik^2}{\pi}\int_S \Big[(\hat{n} \times \overline{E}_+) \cdot \sum_{nm} D_{nm}[\overline{N}^{(3)}_{nm}(k\overline{r}_>)\overline{M}^{(1)}_{nm}(k\overline{r}_<) + \overline{M}^{(3)}_{nm}(k\overline{r}_>)\overline{N}^{(1)}_{nm}(k\overline{r}_<)]dS \\
&\quad - i\left(\frac{\mu_0}{\epsilon_0}\right)^{1/2}(\hat{n} \times \overline{H}_+) \cdot \sum_{nm} D_{nm}[\overline{M}^{(3)}_{nm}(k\overline{r}_>)\overline{M}^{(1)}_{nm}(k\overline{r}_<) + \overline{N}^{(3)}_{nm}(k\overline{r}_>)\overline{N}^{(1)}_{nm}(k\overline{r}_<)]\Big]dS
\end{aligned} \tag{41}$$

where the substitution $k = \omega\sqrt{\mu_0\epsilon_0}$ in the third line has been made for simplification. We can find additional expressions for the coefficients a_{nm} and b_{nm} by matching corresponding $\overline{M}^{(1)}_{nm}$ and $\overline{N}^{(1)}_{nm}$ terms. Through matching, we find that [13]

$$-a_{nm} = \frac{ik^2}{\pi}\int_S \left[(\hat{n}\times\overline{E}_+)\cdot\overline{N}^{(3)}_{nm}(k\overline{r}^{'}) + i\left(\frac{\mu_0}{\epsilon_0}\right)^{1/2}(\hat{n}\times\overline{H}_+)\cdot\overline{M}^{(3)}_{nm}(k\overline{r}^{'})\right]dS \quad (42)$$

$$-b_{nm} = \frac{ik^2}{\pi}\int_S \left[(\hat{n}\times\overline{E}_+)\cdot\overline{M}^{(3)}_{nm}(k\overline{r}^{'}) + i\left(\frac{\mu_0}{\epsilon_0}\right)^{1/2}(\hat{n}\times\overline{H}_+)\cdot\overline{N}^{(3)}_{nm}(k\overline{r}^{'})\right]dS \quad (43)$$

with $\overline{r}_> = \overline{r}^{'}$ because $\overline{r}^{'} > \overline{r}$ inside S.

As stated in [13], the solutions of (42) and (43) guarantee that the total field is zero within S, which is required, due to the Equivalence Principal. These equations can also provide a solution for the surface currents $\hat{n}\times\overline{E}_+$ and $\hat{n}\times\overline{H}_+$, which can then be substituted into (25) in order to obtain the scattered field. However, this substitution assumes scattering from a perfect conductor, while the scattering from a dielectric object is needed. The second part of the problem, dielectric scattering, will now be explored.

Once again expanding the electric field in terms of characteristic vector functions, the internal field of the dielectric is written [13]

$$\overline{E}_{int}(k^{'}\overline{r}) = \sum_{nm}(c_{nm}\overline{M}^{(1)}_{nm}(k^{'}\overline{r}) + d_{nm}\overline{N}^{(1)}_{nm}(k^{'}\overline{r})) \quad (44)$$

where c_{nm} and d_{nm} are again unknown coefficients. The dielectric wavenumber $k^{'} = \omega(\mu\epsilon)^{1/2}$, where μ and ϵ are the absolute permeability and permittivity, respectively, of the medium. They are related to the relative and vacuum values by $\mu_r = \mu/\mu_0$ and $\epsilon_r = \epsilon/\epsilon_0$, where the subscript r denotes the relative values. Substituting for the absolute values, the dielectric wavenumber can be obtained in terms of the relative values and the vacuum wavenumber: $k^{'} = (\mu_r\epsilon_r)^{1/2}k$. Now that the electric field is

specified, we can obtain the magnetic field [13]:

$$\begin{aligned}\overline{H}_{int}(k'\overline{r}) &= \frac{1}{i\omega\mu}\nabla\times\overline{E}_{int}(k'\overline{r}) = \frac{k'}{i\omega\mu}\sum_{nm}(c_{nm}\overline{N}^{(1)}_{nm}(k'\overline{r}) + d_{nm}\overline{M}^{(1)}_{nm}(k'\overline{r})) \\ &= -i\left(\frac{\epsilon_r\epsilon_0}{\mu_r\mu_0}\right)^{1/2}\sum_{nm}(c_{nm}\overline{N}^{(1)}_{nm}(k'\overline{r}) + d_{nm}\overline{M}^{(1)}_{nm}(k'\overline{r}))\end{aligned} \tag{45}$$

In order to determine the coefficients c_{nm} and d_{nm}, the boundary conditions at the surface must be examined. But, first, a combined index σ is introduced, which will now incorporate n and m for more condensed notation. σi will denote the combined indices for the field internal to the surface (as in (44) and (45)), and σe will denote the indices for the external field, as in prior equations.

The boundary conditions require the tangential components of the fields to be continuous at the surface of the dielectric [13]:

$$\hat{n}\times\overline{H}_{ext} = \hat{n}\times\overline{H}_{int} \qquad \hat{n}\times\overline{E}_{ext} = \hat{n}\times\overline{E}_{int} \tag{46}$$

where the subscript *ext* denotes the external fields, and *int* the internal fields. The curl operation is applied to (44) and (45) to determine the tangential component of the internal fields at the surface, applying the change in subscript notation [13]:

$$\hat{n}\times\overline{E}_{int}(k'\overline{r}') = \sum_{\sigma i}^{N}(c_{\sigma i}\hat{n}\times\overline{M}^{(1)}_{\sigma i}(k'\overline{r}') + d_{\sigma i}\hat{n}\times\overline{N}^{(1)}_{\sigma i}(k'\overline{r}')) \tag{47}$$

$$\hat{n}\times\overline{H}_{int}(k'\overline{r}') = -i\left(\frac{\epsilon_r\epsilon_0}{\mu_r\mu_0}\right)^{1/2}\sum_{\sigma i}^{N}(c_{\sigma i}\hat{n}\times\overline{N}^{(1)}_{\sigma i}(k'\overline{r}') + d_{\sigma i}\hat{n}\times\overline{M}^{(1)}_{\sigma i}(k'\overline{r}')) \tag{48}$$

Equations (47) and (48) are now substituted into Equations (42) and (43) because of

the equality in (46). For the first $2N$ terms of $-a_{nm} = -a_{\sigma e}$, we obtain

$$-a_{\sigma e} = \frac{ik^2}{\pi}\int_S \Bigg[\overline{N}^{(3)}_{\sigma e}(k\overline{r}^{'})\cdot(c_{\sigma i}\hat{n}\times\overline{M}^{(1)}_{\sigma i}(k^{'}\overline{r}^{'}) + d_{\sigma i}\hat{n}\times\overline{N}^{(1)}_{\sigma i}(k^{'}\overline{r}^{'})) + \left(\frac{\epsilon_r}{\mu_r}\right)^{1/2}\overline{M}^{(3)}_{\sigma e}(k\overline{r}^{'})\cdot(c_{\sigma i}\hat{n}\times\overline{N}^{(1)}_{\sigma i}(k^{'}\overline{r}^{'}) + d_{\sigma i}\hat{n}\times\overline{M}^{(1)}_{\sigma i}(k^{'}\overline{r}^{'}))\Bigg]dS \tag{49}$$

In order to simplify this expression, the $c_{\sigma i}$ and $d_{\sigma i}$ terms can be grouped. Considering only the $c_{\sigma i}$ term, we have

$$\frac{ik^2}{\pi}c_{\sigma i}\int_S\left[\overline{N}^{(3)}_{\sigma e}(k\overline{r}^{'})\cdot\hat{n}\times\overline{M}^{(1)}_{\sigma i}(k^{'}\overline{r}^{'}) + \left(\frac{\epsilon_r}{\mu_r}\right)^{1/2}\overline{M}^{(3)}_{\sigma e}(k\overline{r}^{'})\cdot\hat{n}\times\overline{N}^{(1)}_{\sigma i}(k^{'}\overline{r}^{'})\right]dS \tag{50}$$

Applying $A\cdot(B\times C) = B\cdot(C\times A) = -B\cdot(A\times C)$, and separating terms, we get

$$-\frac{ik^2}{\pi}c_{\sigma i}\int_S\left[\hat{n}\cdot\overline{N}^{(3)}_{\sigma e}(k\overline{r}^{'})\times\overline{M}^{(1)}_{\sigma i}(k^{'}\overline{r}^{'})\right]dS - \frac{ik^2}{\pi}c_{\sigma i}\left(\frac{\epsilon_r}{\mu_r}\right)^{1/2}\int_S\left[\hat{n}\cdot\overline{M}^{(3)}_{\sigma e}(k\overline{r}^{'})\times\overline{N}^{(1)}_{\sigma i}(k^{'}\overline{r}^{'})\right]dS \tag{51}$$

which can then be condensed to

$$\left[-iK - i\left(\frac{\epsilon_r}{\mu_r}\right)^{1/2}J\right]c_{\sigma i} \tag{52}$$

where [13]

$$\begin{aligned} K &= \frac{k^2}{\pi}\int_S\left[\hat{n}\cdot\overline{N}^{(3)}_{\sigma e}(k\overline{r}^{'})\times\overline{M}^{(1)}_{\sigma i}(k^{'}\overline{r}^{'})\right]dS \\ J &= \frac{k^2}{\pi}\int_S\left[\hat{n}\cdot\overline{M}^{(3)}_{\sigma e}(k\overline{r}^{'})\times\overline{N}^{(1)}_{\sigma i}(k^{'}\overline{r}^{'})\right]dS \end{aligned} \tag{53}$$

Similarly, the remaining $c_{\sigma i}$ and $d_{\sigma i}$ terms for both $a_{\sigma e}$ and $b_{\sigma e}$ can be condensed, so we obtain [13]

$$-ia_{\sigma e} = \left[K + \left(\frac{\epsilon_r}{\mu_r}\right)^{1/2}J\right]c_{\sigma i} + \left[L + \left(\frac{\epsilon_r}{\mu_r}\right)^{1/2}I\right]d_{\sigma i} \tag{54}$$

$$-ib_{\sigma e} = \left[I + \left(\frac{\epsilon_r}{\mu_r} \right)^{1/2} L \right] c_{\sigma i} + \left[J + \left(\frac{\epsilon_r}{\mu_r} \right)^{1/2} K \right] d_{\sigma i} \tag{55}$$

for $\sigma e = 1, 2, \ldots, N$, with (53) and [13]

$$\begin{aligned} L &= \frac{k^2}{\pi} \int_S \left[\hat{n} \cdot \overline{N}^{(3)}_{\sigma e}(k\overline{r}^{\,\prime}) \times \overline{N}^{(1)}_{\sigma i}(k^{\prime}\overline{r}^{\,\prime}) \right] dS \\ I &= \frac{k^2}{\pi} \int_S \left[\hat{n} \cdot \overline{M}^{(3)}_{\sigma e}(k\overline{r}^{\,\prime}) \times \overline{M}^{(1)}_{\sigma i}(k^{\prime}\overline{r}^{\,\prime}) \right] dS \end{aligned} \tag{56}$$

Thus, a set of compact expressions for $a_{\sigma e}$ and $b_{\sigma e}$ has been obtained, in terms of I, J, K, L. These equations can then be solved for the expansion coefficients of the internal field, $c_{\sigma i}$ and $d_{\sigma i}$, which can then be used in (47) and (48) to find $\hat{n} \times \overline{E}_{int}$ and $\hat{n} \times \overline{H}_{int}$, which, in turn, are finally substituted into (25) to obtain the scattered field [13]:

$$\overline{E}^{s}(k\overline{r}) = \sum_{\sigma e=1}^{N} [p_{\sigma e} \overline{M}^{(3)}_{\sigma e}(k\overline{r}) + q_{\sigma e} \overline{N}^{(3)}_{\sigma e}(k\overline{r})] \tag{57}$$

where [13]

$$p_{\sigma e} = -iD_{\sigma e} \sum_{\sigma i}^{N} \left\{ \left[K^{\prime} + \left(\frac{\epsilon_r}{\mu_r} \right)^{1/2} J^{\prime} \right] c_{\sigma i} + \left[L^{\prime} + \left(\frac{\epsilon_r}{\mu_r} \right)^{1/2} I^{\prime} \right] d_{\sigma i} \right\} \tag{58}$$

$$q_{\sigma e} = -iD_{\sigma e} \sum_{\sigma i}^{N} \left\{ \left[I^{\prime} + \left(\frac{\epsilon_r}{\mu_r} \right)^{1/2} L^{\prime} \right] c_{\sigma i} + \left[J^{\prime} + \left(\frac{\epsilon_r}{\mu_r} \right)^{1/2} K^{\prime} \right] d_{\sigma i} \right\} \tag{59}$$

and [13]

$$\begin{aligned} I^{\prime} &= \frac{k^2}{\pi} \int_S \left[\hat{n} \cdot \overline{M}^{(1)}_{\sigma e}(k\overline{r}^{\,\prime}) \times \overline{M}^{(1)}_{\sigma i}(k^{\prime}\overline{r}^{\,\prime}) \right] dS \\ J^{\prime} &= \frac{k^2}{\pi} \int_S \left[\hat{n} \cdot \overline{M}^{(1)}_{\sigma e}(k\overline{r}^{\,\prime}) \times \overline{N}^{(1)}_{\sigma i}(k^{\prime}\overline{r}^{\,\prime}) \right] dS \\ K^{\prime} &= \frac{k^2}{\pi} \int_S \left[\hat{n} \cdot \overline{N}^{(1)}_{\sigma e}(k\overline{r}^{\,\prime}) \times \overline{M}^{(1)}_{\sigma i}(k^{\prime}\overline{r}^{\,\prime}) \right] dS \\ L^{\prime} &= \frac{k^2}{\pi} \int_S \left[\hat{n} \cdot \overline{N}^{(1)}_{\sigma e}(k\overline{r}^{\,\prime}) \times \overline{N}^{(1)}_{\sigma i}(k^{\prime}\overline{r}^{\,\prime}) \right] dS \end{aligned} \tag{60}$$

Note that the difference between the primed I, J, K, L and the unprimed is the pres-

ence of solutions of the first kind versus the third.

The expression for the scattered field contains solutions of the third kind ($\overline{M}_{\sigma e}^{(3)}$ and $\overline{N}_{\sigma e}^{(3)}$), which contain spherical Hankel functions. These Hankel functions can be represented in terms of the exponential e^{ikr}, allowing us to pull the term out and express the scattered field in terms of the vector far-field amplitude times the exponential [13]:

$$\overline{E}^s(k\bar{r}) = \overline{F}(\theta_s, \phi_s/\theta_i, \phi_i)\frac{e^{ikr}}{r}, \qquad kr \to \infty \tag{61}$$

where $\overline{F}(\theta_s, \phi_s/\theta_i, \phi_i)$ is the vector far-field amplitude dependent on the directions of the incident (θ_i, ϕ_i) and scattered (θ_s, ϕ_s) fields.

The differential scattering cross section is [13]

$$\sigma_D = \lim_{r\to\infty}\left[4\pi r^2 \frac{S_s(\theta_s, \phi_s)}{S_i(\theta_i, \phi_i)}\right] \tag{62}$$

where the scattered power density, $S_s(\theta_s, \phi_s)$ is [13]

$$S_s(\theta_s, \phi_s) = \frac{|\overline{F}(\theta_s, \phi_s/\theta_i, \phi_i)|^2}{2Z_0 r^2}, \qquad Z_0 = \sqrt{\mu_0/\epsilon_0} \tag{63}$$

and the incident power density, $S_i(\theta_i, \phi_i)$ is [13]

$$S_i(\theta_i, \phi_i) = \frac{|\overline{E}^i|^2}{2Z_0} \tag{64}$$

Finally, combining these two expressions in (62), with $\overline{E}^i$ having unit amplitude, the differential cross section becomes [13]

$$\sigma_D = 4\pi|\overline{F}(\theta_s, \phi_s/\theta_i, \phi_i)|^2 \tag{65}$$

The derivation of this scattering representation for a dielectric object, particularly within the resonance regions, provides the basis and understanding for Dr. Miranda's scattering model and its through-wall, multipath adaption, presented in the next chapter. Of particular importance is Equation (57) and its associated coefficients. This equation becomes the foundation of our expansion into the multipath representation, discussed in the following chapter, Section 5.1.

V. Research Approach

This chapter describes the approach to the research, as well as considerations leading to certain design decisions. The first section develops the scattering model, the second provides the experimental setup, methods, and procedures, and, finally, the third section presents data processing methods.

The purpose of this project is the development of a child-adult discrimination method via through-the-wall radar. To accomplish this purpose, two main objectives are explored. The first is the development of a through-wall radar scattering model appropriate to a corner space — that is, the ground and an adjacent wall — using the Miranda sphere-cylinder human representation.

The second objective is the investigation of feature sets for child-adult, through-wall classification. In this investigation, radar data of both children and adults will be obtained in through-the-wall experiments. Features will be extracted from the experimentally-obtained radar data and fed into a Support Vector Machine in order to classify the radar data as that of a child or adult. The performance of the SVM on different processed data will be examined.

5.1 Scattering Model

The scattering model builds directly upon the work presented in Barber and Yeh [13] as described in Chapter IV, Section 4.2, as well as Miranda's modification of the work. The Miranda model will be presented first, which models the direct path only. The adaptation to the through-wall, multipath scenario will be presented next.

Miranda Direct-Path Scattering Model

The direct-path scattering model combines the scattering of multiple objects, whose size parameters must obey the cylinder-sphere model described in Chapter III, Section 3.3. For this human model, we have three dielectric objects: the prolate sphere and the two cylinders. Drawing from Equation (57), the scattering for these three objects is the sum of the scattering from the individual objects:

$$\overline{E}^s(k\overline{r}) = \sum_{j=1}^{3}\sum_{\sigma e=1}^{N}[p_{j\sigma e}\overline{M}^{(3)}_{j\sigma e}(k\overline{r}) + q_{j\sigma e}\overline{N}^{(3)}_{j\sigma e}(k\overline{r})] \tag{66}$$

where $\bar{r}$ is the vector denoting the path from the origin to the field point P. Now, for the scattering from multiple objects, this expression is an approximation, involving only the sum of the scattering from individual objects. A more general form involves the secondary scattering from each pair of objects — that is, the scattering from object j due to the scattering from object i. For a number of scattering objects K located at $\bar{r}_1, \bar{r}_2 \ldots \bar{r}_K$, a transmitting antenna located at $\bar{r}_T$ and a receiving antenna located at $\bar{r}_R$, the scalar field that incorporates this secondary scattering can be represented as [1]

$$E^s(\theta_i, \theta_s) = \sum_{i,j=1}^{K}\int_{S_{ij}} |A_{ij}| \frac{e^{ik\Phi_{ij}}}{R_i R_j} dS_{ij} \tag{67}$$

where $\Phi = R_i + R_j$, $R_{i(j)} = \left|\bar{r}_{i(j)} - \bar{r}_{T(R)}\right|$, $|A_{ij}|$ is the amplitude of the scattering from object j due to object i, and S_{ij} represents the space through which the scattering due to the object pairs propagates. E^s is dependent on the angles θ_i and θ_s, describing the incident and scattered vectors from a central reference. For K = 3, as in the human cylinder-sphere model, we obtain a sum of six terms. When $i = j$, we recover the scalar field from (66) due to the sum of the scattering from each individual object.

In the next subsection, we consider the direct-path scattering model extended to multiple paths.

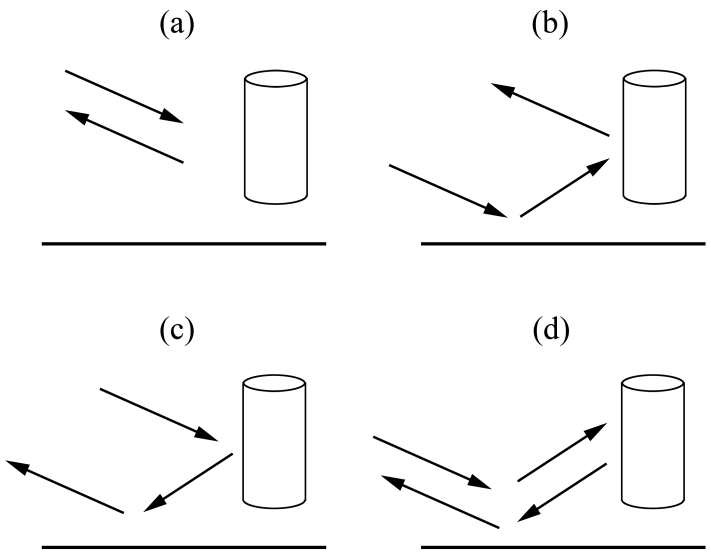

Figure 8. Four-Path Reflections (reproduced from [15]). (a) The direct path, no additional reflections; (b) scattering from the ground to object of interest, and back to the receiver; (c) the reverse of (b), from the object to ground, and back; (d) the most indirect path, reflecting from the ground in both directions.

Multipath Scattering Model

When the source and objects of interest are considered to exist in free space, with no obstructions or surrounding surfaces, Equations (66) or (67) are sufficient to describe the electromagnetic scattering. However, when an object is separated from the source by an obstruction such as a wall, and located near surfaces such as walls and ground, the scattered electromagnetic energy is affected by these additional surfaces. Whenever a wave is incident upon a surface, a portion will be reflected, and a portion transmitted, leading to losses and attenuation of the signal. Hence, the multipath extension of the Miranda scattering model will incorporate the effects of barriers and reflecting surfaces. The expansion due to multiple reflecting paths will be explored first, followed by the incorporation of transmission and reflection losses.

In a multipath environment, the received signal can be thought of as the sum of the multiple paths to and from the object, caused by reflections of the transmitted

and scattered signals from surrounding surfaces. In a simple example, which consists of the radar system, an object of interest, and the ground, there are four possible paths as shown in Figure 8: (a) the most direct path from the radar to the object, which is the case of a target in free space; (b) the path from the radar, reflecting from the ground to the object, and back to the receiver; (c) the reverse of this path; and (d) the most indirect path, which is from the radar, to the ground, object, back to the ground, and finally to the receiver. Of these four paths, we expect the most direct path to give the strongest return because it is the shortest and involves no reflections or absorptions from surfaces other than the object. The most indirect path can be expected to give the weakest return, because it is the opposite case — the longest path with the most reflections and absorptions. [23]

Our experiment, described in Section , introduces a corner arrangement: not only transmission through an obstructing wall, but also reflections from an adjacent wall and ground. The wall through which the radar system radiates can provide reflections, but, for the purposes of the model, the obstructing wall will be assumed to simply attenuate the signal. Therefore, in order to determine the multiple paths to the object of interest, we consider the source, the adjacent wall, the ground, and the object only. A simple notation to represent the paths is constructed: S = source, W = wall, G = ground, and T = object (i.e., target); the path from source to imaged object is then represented as ST. Thus, the four round-trip paths of the previous example can be represented:

Table 2. Paths Between Object of Interest and Ground

Path A (most direct)	STS
Path B	SGTS
Path C	STGS
Path D (least direct)	SGTGS

A similar arrangement is given considering only the wall and the imaged object:

Table 3. Paths Between Object of Interest and Wall

Path E	SWTS
Path F	STWS
Path G	SWTWS

And, finally, the arrangements considering the wall, ground, and imaged object, allowing the wall and ground to be struck only once before and/or after the object, are:

Table 4. Paths Involving Multiple Reflections Between Wall and Ground

# Reflections:	2		3		4	
	Path	**Order**	**Path**	**Order**	**Path**	**Order**
	H	SWGTS	N	SWGTGS	V	SWGTGWS
	I	SWTGS	O	SWGTWS	W	SWGTWGS
	J	SGWTS	P	SWTGWS	X	SGWTGWS
	K	SGTWS	Q	SWTWGS	Y	SGWTWGS
	L	STWGS	R	SGWTGS		
	M	STGWS	S	SGWTWS		
			T	SGTGWS		
			U	SGTWGS		

Thus, there are 25 possible paths from the source to the object, and the total scattering is the sum of the scattering along all paths. Only those paths that are the direct reverses of each other are the same length, such as paths B and C, or W and X, for example.

Because the energy from the radar is attenuated as $\sim 1/R^2$, and by the loss of transmission through surrounding surfaces, we assume that the longest paths — those with the highest numbers of reflections — will contribute the least to the sum, and, so, we neglect them to simplify calculations. We will consider only those paths from Tables 2 and 3, and the paths from Table 4 with two reflections, for a total of thirteen paths.

The representation of the scalar field, now, is relatively simple, as we incorporate

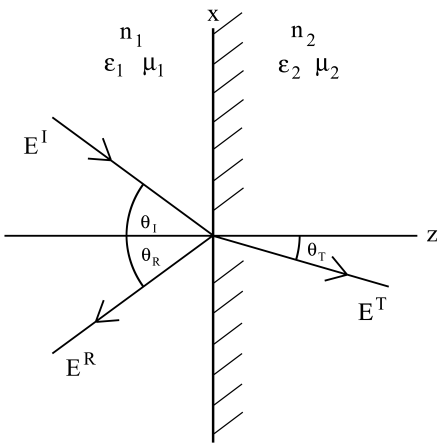

Figure 9. Reflection and Transmission Between Two Media. The incident and reflected fields are E^I and E^R, respectively; the transmitted field is E^T. The index of refraction, permittivity, permeability, for media 1 is n_1, ϵ_1, and μ_1, while those for media 2 are labeled with the subscript 2. The subscripts I, R, T denote the angles of incidence, reflection, and transmission, respectively.

the additional paths:

$$E^s(\theta_i, \theta_s) = \sum_{p=1}^{L} \sum_{i,j=1}^{K} \int_{S_{ij}} |A_{ij}| \frac{e^{ik\Phi_{pij}}}{R_{pi} R_{pj}} dS_{ij} \tag{68}$$

where L is the number of paths chosen to model between the objects of interest and source. The phase Φ_{ij} and distances between the scattering objects and transmitter/receiver $R_{i(j)}$ now depend upon the path taken.

This representation assumes perfect transmission through the wall and perfect reflections from the other surfaces. Since this is not generally the case, we now apply the Fresnel equations for the amplitude of an electromagnetic wave.

Consider a monochromatic plane wave incident on a surface, as shown in Figure 9. For standard wall materials, we assume that the relative permeability is $\mu_r = 1$. We can represent the incident wave as [36]

$$\bar{E}_I(\bar{r}, t) = \bar{E}_{0_I} e^{i(\bar{k}_I \cdot \bar{r} - \omega t)} \tag{69}$$

The reflected and transmitted waves have similar expressions. According to the Fresnel equations, the reflected and transmitted amplitudes are related to the incident amplitude by the reflection and transmission coefficients [36]:

$$E_{0_R} = r_{\parallel(\perp)} E_{0_I}, \qquad E_{0_T} = t_{\parallel(\perp)} E_{0_I} \tag{70}$$

where E_{0_R} and E_{0_T} are the reflected and transmitted amplitudes respectively, E_{0_I} is the incident amplitude, and the reflection and transmission coefficients, r and t, are labeled by the subscripts $\parallel$ or $\perp$ to denote parallel or perpendicular polarization of the incident wave. Parallel polarization is within the plane of incidence, shown as the x-z plane in Figure 9. Perpendicular polarization is perpendicular to this plane.

The coefficients are [36]

$$r_\parallel = \frac{n_2 \cos\theta_i - n_1 \cos\theta_t}{n_2 \cos\theta_i + n_1 \cos\theta_t} \tag{71}$$

$$r_\perp = \frac{n_1 \cos\theta_i - n_2 \cos\theta_t}{n_1 \cos\theta_i + n_2 \cos\theta_t} \tag{72}$$

$$t_\parallel = \frac{2 n_1 \cos\theta_i}{n_2 \cos\theta_i + n_1 \cos\theta_t} \tag{73}$$

$$t_\perp = \frac{2 n_1 \cos\theta_i}{n_1 \cos\theta_i + n_2 \cos\theta_t} \tag{74}$$

where the index of refraction of the first medium is n_1 and that of the second medium is n_2. For unpolarized radiation, we assume an equal mix of parallel and perpendicular polarizations and take the average of the polarized reflection or transmission coefficients:

$$r = \frac{r_\parallel + r_\perp}{2}, \qquad t = \frac{t_\parallel + t_\perp}{2} \tag{75}$$

The relationship between the incident angle θ_i and transmitted angle θ_t is governed

by Snell's law:

$$\frac{\sin\theta_t}{\sin\theta_i} = \frac{n_1}{n_2} \tag{76}$$

and the index of refraction of a material can be found by the relation

$$n = \frac{c}{v} = \sqrt{\epsilon_r \mu_r} \tag{77}$$

where c is the speed of light in vacuum, v is the speed of the electromagnetic wave in the material, and ϵ_r, μ_r are the relative permittivity and permeability of the material respectively.

Using these equations and the knowledge that the un-reflected or un-transmitted wave is related to the reflected or transmitted wave simply by the reflection or transmission coefficients, we can incorporate these coefficients into our expression of the scalar field. Let $t_{ij} = t_i t_j$ represent the combined, round-trip transmission for one path, through an obstructing wall in the forward (i) and return (j) directions, which depends on the path taken and the objects of incidence and scattering, and $r = r_1 r_2 \dots r_B$ is now the combined reflection coefficient due to the total number of reflections B in one path. The individual reflections $r_1, r_2, \dots, r_B$ also depend upon the object of incidence (if moving toward the imaged object) or object of scattering (if returning to the receiver). Then the scalar field E^s becomes

$$E^s(\theta_i, \theta_s) = \sum_{p=1}^{L} \sum_{i,j=1}^{K} t_{pij} r_{pij} \int_{S_{ij}} |A_{ij}| \frac{e^{ik\Phi_{pij}}}{R_{pi} R_{pj}} dS_{ij} \tag{78}$$

Not only do the individual reflections $r_1, r_2, \dots, r_B$ and transmissions t_i, t_j depend upon the path and incident or scattering objects, but also upon the polarization. Hence, the parallel, perpendicular, or average polarization expressions must be used accordingly.

Extending the multipath concept, as well as the transmissions and reflections, to Equation (66), we have

$$\overline{E}^s(k\overline{r}) = \sum_{p=1}^{L}\sum_{j=1}^{K} t_{pj} r_{pj} \sum_{\sigma e=1}^{N} [p_{pj\sigma e}\overline{M}^{(3)}_{pj\sigma e}(k\overline{r}) + q_{pj\sigma e}\overline{N}^{(3)}_{pj\sigma e}(k\overline{r})] \tag{79}$$

Now, the combined transmission and reflection coefficients depend only upon the path, object of incidence (the incident and scattering object are the same, since $i = j$), and polarization. Expanding the coefficients $p_{pj\sigma e}$ and $q_{pj\sigma e}$, the remainder of the expression for the scattered field is

$$p_{pj\sigma e} = -iD_{\sigma e}\sum_{\sigma i}^{N}\left\{\left[K'_{pj} + \left(\frac{\epsilon_r}{\mu_r}\right)^{1/2} J'_{pj}\right] c_{pj\sigma i} + \left[L'_{pj} + \left(\frac{\epsilon_r}{\mu_r}\right)^{1/2} I'_{pj}\right] d_{pj\sigma i}\right\} \tag{80}$$

$$q_{pj\sigma e} = -iD_{\sigma e}\sum_{\sigma i}^{N}\left\{\left[I'_{pj} + \left(\frac{\epsilon_r}{\mu_r}\right)^{1/2} L'_{pj}\right] c_{pj\sigma i} + \left[J'_{pj} + \left(\frac{\epsilon_r}{\mu_r}\right)^{1/2} K'_{pj}\right] d_{pj\sigma i}\right\} \tag{81}$$

where

$$\begin{aligned}
I'_{pj} &= \frac{k^2}{\pi}\int_S \left[\hat{n}\cdot\overline{M}^{(1)}_{pj\sigma e}(k\overline{r}')\times\overline{M}^{(1)}_{pj\sigma i}(k'\overline{r}')\right]dS \\
J'_{pj} &= \frac{k^2}{\pi}\int_S \left[\hat{n}\cdot\overline{M}^{(1)}_{pj\sigma e}(k\overline{r}')\times\overline{N}^{(1)}_{pj\sigma i}(k'\overline{r}')\right]dS \\
K'_{pj} &= \frac{k^2}{\pi}\int_S \left[\hat{n}\cdot\overline{N}^{(1)}_{pj\sigma e}(k\overline{r}')\times\overline{M}^{(1)}_{pj\sigma i}(k'\overline{r}')\right]dS \\
L'_{pj} &= \frac{k^2}{\pi}\int_S \left[\hat{n}\cdot\overline{N}^{(1)}_{pj\sigma e}(k\overline{r}')\times\overline{N}^{(1)}_{pj\sigma i}(k'\overline{r}')\right]dS
\end{aligned} \tag{82}$$

The coefficients $c_{pj\sigma i}$ and $d_{pj\sigma i}$ are found by solving the system of equations

$$-ia_{j\sigma e} = \left[K_{pj} + \left(\frac{\epsilon_r}{\mu_r}\right)^{1/2} J_{pj}\right] c_{pj\sigma i} + \left[L_{pj} + \left(\frac{\epsilon_r}{\mu_r}\right)^{1/2} I_{pj}\right] d_{pj\sigma i} \tag{83}$$

$$-ib_{j\sigma e} = \left[I_{pj} + \left(\frac{\epsilon_r}{\mu_r}\right)^{1/2} L_{pj}\right] c_{pj\sigma i} + \left[J_{pj} + \left(\frac{\epsilon_r}{\mu_r}\right)^{1/2} K_{pj}\right] d_{pj\sigma i} \tag{84}$$

where

$$
\begin{aligned}
K_{pj} &= \frac{k^2}{\pi}\int_S \left[\hat{n}\cdot\overline{N}^{(3)}_{pj\sigma e}(k\overline{r}')\times\overline{M}^{(1)}_{pj\sigma i}(k'\overline{r}')\right]dS \\
J_{pj} &= \frac{k^2}{\pi}\int_S \left[\hat{n}\cdot\overline{M}^{(3)}_{pj\sigma e}(k\overline{r}')\times\overline{N}^{(1)}_{pj\sigma i}(k'\overline{r}')\right]dS \\
L_{pj} &= \frac{k^2}{\pi}\int_S \left[\hat{n}\cdot\overline{N}^{(3)}_{pj\sigma e}(k\overline{r}')\times\overline{N}^{(1)}_{pj\sigma i}(k'\overline{r}')\right]dS \\
I_{pj} &= \frac{k^2}{\pi}\int_S \left[\hat{n}\cdot\overline{M}^{(3)}_{pj\sigma e}(k\overline{r}')\times\overline{M}^{(1)}_{pj\sigma i}(k'\overline{r}')\right]dS
\end{aligned}
\tag{85}
$$

Finally, the expressions for $\overline{M}_{pj\sigma}(\overline{r})$ and $\overline{N}_{pj\sigma}(\overline{r})$ are given by

$$\overline{M}_{pj\sigma}(k\overline{r}) = \nabla\times\overline{r}f_\sigma(r,\theta_{pj},\phi_{pj}) \tag{86}$$

$$\overline{N}_{pj\sigma}(k\overline{r}) = \frac{1}{k}\nabla\times\overline{M}_{pj\sigma}(k\overline{r}) \tag{87}$$

$$f_\sigma(r,\theta_{pj},\phi_{pj}) = \sum_{n=0}^{\infty} z_n(kr)\left[a_{n0}P_n(\cos\theta_{pj}) + \sum_{m=1}^{n}(a_{nm}\cos m\phi_{pj} + b_{nm}\sin m\phi_{pj})P_n^m(\cos\theta_{pj})\right] \tag{88}$$

where σ denotes the combined mn index. θ and ϕ denote the scattered elevation and azimuth angles, respectively, and depend upon the path p, imaged object j, and source; and $\bar{r}$ is primed when referring to a source, and unprimed when referring to the field point. The spherical Bessel function $z_n(kr)$ is either the first or third kind (Hankel function), depending on the superscript of $\overline{M}$ or $\overline{N}$.

Equation (79), together with supporting Equations (80)-(88), is our final representation of the scattering from an object in a corner wall scenario. This theoretical contribution may be used for any arrangement of K volumes comprising an object, and any number of paths L between the radar source and scattering volumes. These expressions will be used in future work to model the electromagnetic scattering of a human as represented by the Miranda cylinder-sphere model, in a corner-wall arrangement with the scattering paths given by Tables 2 and 3, and the two-reflection paths of Table 4.

5.2 Experimental Setup

The test locations and radar equipment were provided by the Air Force Research Lab (AFRL), Wright-Patterson AFB. Two locations at AFRL were tested. Preliminary line-of-sight radar tests were carried out at the Human Signatures Lab at AFRL's RHXBA both to replicate a more realistic, cluttered environment, and to accommodate additional researchers who desired to operate experiments in conjunction with ours when the children subjects were available. The initial radar equipment operating at 1 Watt was able to resolve objects of interest, despite the noise and clutter of the location. However, this equipment was requisitioned for other projects, and we were only able to obtain a milliwatt system for the remainder of our study. At such low power, the high noise level of the location was unmanageable. Extensive efforts were made to determine cause of the noise and times of the day when it might drop to a manageable level. These efforts were unsuccessful: Unfortunately, the tests for causes were inconclusive, and the low noise time periods remained unreliable.

Restrictions to operate at the original location were lifted, however, so, in light of the noise levels, the experiment was moved to RYM's Indoor Range, an anechoic chamber lined with radar-absorbing foam. Signals were much-improved in this new location, so all human testing was performed here.

An ultra-wide band, UHF frequency range is used in this project. The chosen range was deemed ideal for through-wall penetration, 400 MHz to 800 MHz, based on prior work of Schmitt [37]. From Equation (1), this range provides a fractional bandwidth of 66.7%, which fits the definition of UWB radar. The range resolution at this bandwidth, from Equation (2), is 0.375 m, sufficient for resolving two adjacent humans, as long as they are outside this range.

The following subsections describe the experimental setup in the Indoor Range in detail, covering the equipment and testing environment. We then discuss consider-

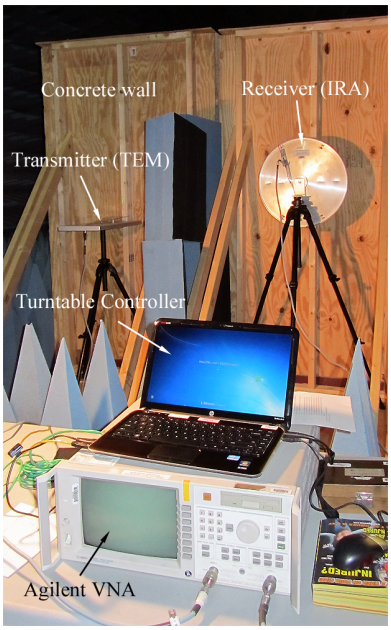

Figure 10. Equipment Used. The above photograph displays the equipment, as it was arranged in the Indoor Range. The transmitting and receiving antennas were located behind a concrete wall (framed by plywood, so the concrete is not visible in this image), and aimed along a path parallel to an adjacent wall (on the right, not shown). The Agilent VNA provided and received the radar signals, while the laptop was used to control the turntable and download radar data. The pale blue pyramids are the absorbing foam, surrounding the entire setup, and a stack of foam was placed between the antennas in order to cut down some of the interference between them.

ations made in choosing wall material and building the wall, and conclude with the process of working with human volunteers, particularly children.

Equipment

The radar system used is a simple, two-antenna system powered by a Vector Network Analyzer (VNA). Originally, a Doppler radar system was to be used. However, this system was not available for this thesis, so the static, non-Doppler VNA system was used instead.

The equipment is displayed in Figure 10. The VNA used is an Agilent 8714ES RF Network Analyzer, capable of operating at a range from 300 kHz to 3000 MHz. During all experiments, it operated at 0 dBm (1 mW) power, in S21 (transmission)

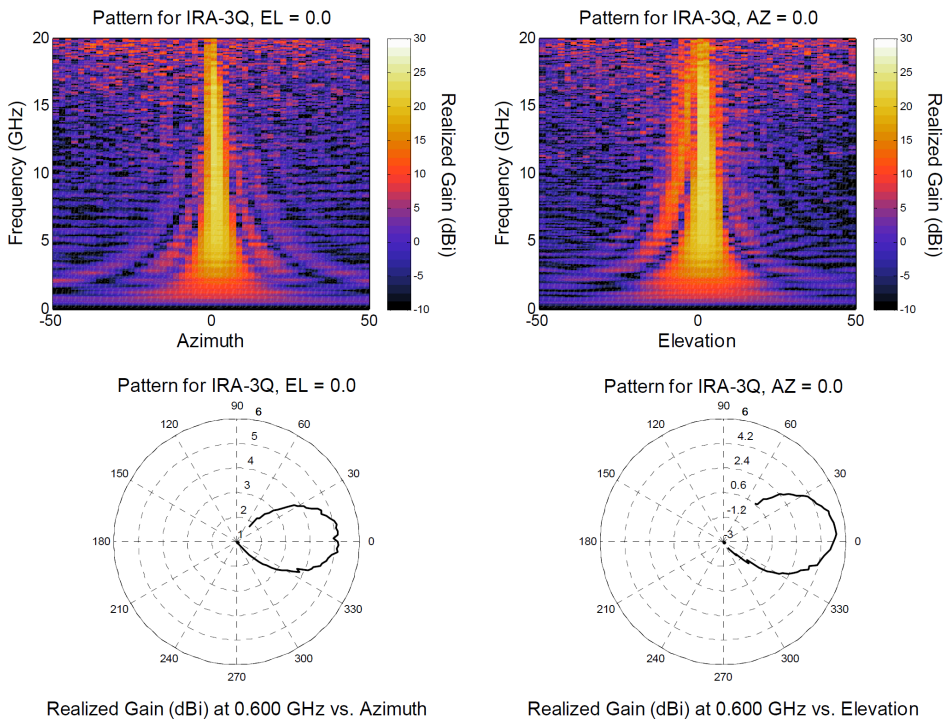

Figure 11. IRA-3Q (Receiving) Antenna Pattern. The realized gain as a function of frequency and azimuth is shown on the top left, and as a function of frequency and elevation on the top right. The realized gain at 600 MHz, the center of our 400-800 MHz frequency range, is shown below, as functions of azimuth and elevation.

.

mode. An ultra-wide band, UHF frequency range was employed at 400 - 800 MHz. The two antennas available for the experiment were commercial-off-the-shelf (COTS) Farr Fields, LC antennas, a model TEM-1 and a model IRA-3Q. The model TEM-1 is capable of transmitting from 0.586 GHz to 20.1 GHz and was used as the output, or transmitting, antenna. The IRA-3Q was used as the input, or receiver, because it possessed the wider frequency range spanning 250 MHz to 20 GHz. The gain for the receiver is shown in Figure 11. Both antennas were connected to the VNA via SMA connectors. A laptop was networked to the VNA via an Ethernet cable in order to obtain data files from the VNA for processing.

A small turntable, built and provided by Matrix Research Associates (MRA), was used as the platform for all human subjects. The VNA is capable of recording

only static, non-Doppler signals from objects. Therefore, several angular views of the subjects were taken, in order to better characterize their radar signatures, as any particular view of a human subject could be presented to a radar system in real-world scenarios. The turntable facilitates the gathering of data at precise angular increments. It is fully capable of rotation through 360°, as well as supporting the weight of an adult human; it rotated at a slow, stable speed to prevent unbalancing of the subject. We hardwired the turntable to a power supply and controlled it, through a USB cable, by the laptop mentioned above. The controlling software, customized by MRA, ran in LabView.

Subject Environment

The layout of the experimental setup is illustrated in Figure 12. An array of eight concrete wall sections were built from 4"x8"x16" solid concrete blocks and arranged in a corner shape in order to test the through-wall, multipath scattering model. These walls were built by MRA. Because they form a temporary structure, the walls were constructed on pallets, in sections three blocks wide (roughly 48" or 1.2 m) and eleven blocks tall (88" or 2.2 m), for maneuverability. The 4-inch dimension was used as the thickness of the wall. Two wall sections formed the short side of the corner arrangement, where the radar system was placed (seen in the left side of Figure 12), and six sections form the long side of the corner (bottom of the figure).

The testing location was the anechoic chamber of the Indoor Range at AFRL, Wright-Patterson, AFB. The concrete walls were placed in a corner of the chamber, blocking off a testing area of about 5.7 m x 9.4 m, measured from the inside surface of the concrete walls to the walls of the anechoic chamber. The concrete walls formed a corner of about 2.54 m x 7.3 m; the opposite sides of the testing area were bordered by radar absorbing foam. We laid a layer of thick aluminum foil on the floor between the

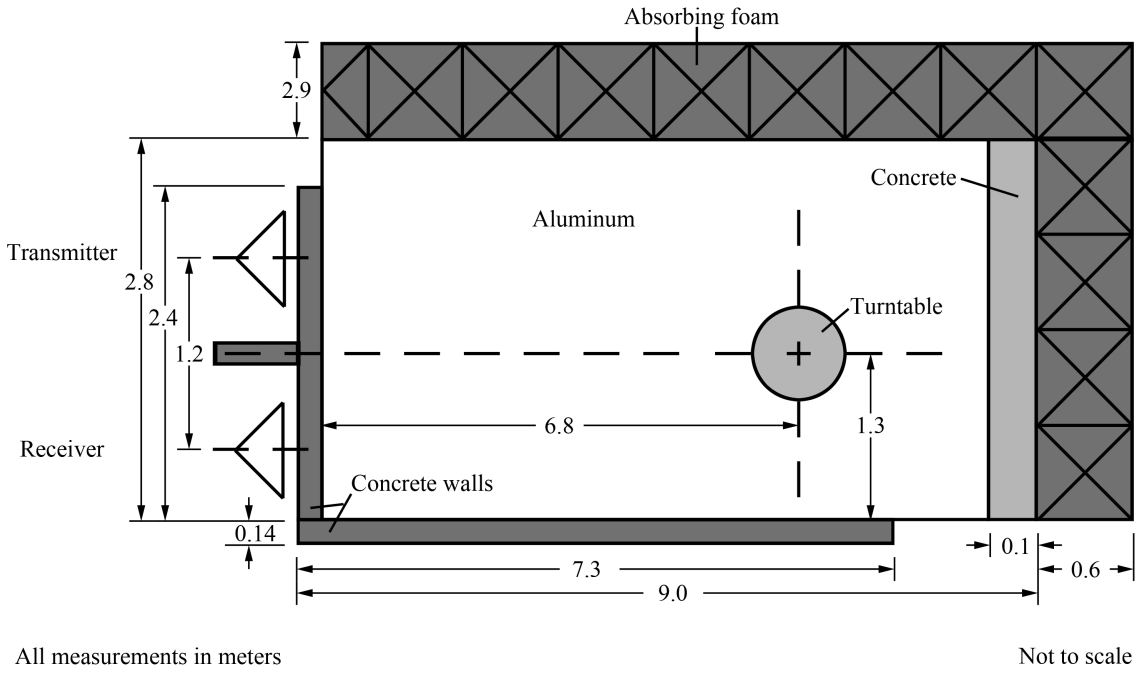

Figure 12. Experimental Setup. Custom-built concrete wall sections were erected in a corner arrangement as seen above. There were eight wall sections, built out of 4"x8"x16" solid concrete blocks; wall sections were 1.2 m wide x 2.2 m tall x 0.087 m thick (the 0.14 m thickness presented in the figure includes supporting plywood on either side of the concrete blocks). Two of the sections form the short length of the wall on the left of the figure; six of the sections form the long side on the bottom. The antennas were placed 1.2 m apart, centered on the short wall, with a 0.17-m thickness of absorbing foam between them (unlabeled in the figure). The ground was covered with a layer of thick aluminum foil to present a uniform surface. An edge of concrete at the side of the range opposite the radar was left uncovered to reduce corner reflections between the ground and foam. A boundary of absorbing foam borders the sides of the range opposite the concrete walls. The walls opposite the concrete walls are covered with absorbing foam, as well. The turntable, upon which human subjects stood, was located between the two antennas, at a distance of 6.8 m.

concrete walls and the foam in order to present a uniform ground surface. A concrete surface was our preference; however, the Indoor Range possesses large, metal grating in the concrete floor, which would introduce anomalies in the radar signals. The need for a uniform ground surface took precedence over the desire for concrete, so the entire surface was covered. At the far end of this radar range, a small strip of the original concrete surface was left uncovered. This uncovered concrete had the effect of presenting a somewhat more gradual transition from the reflecting surface of the aluminum to the absorbing foam and, thus, reducing the amplitude of the peak caused by the corner reflection at the boundary there.

The antennas were placed in the center of each of the two concrete wall sections, in the left side of Figure 12, separated by 1.2 m. They were placed as close as possible to the concrete wall, given the positioning of the tripods, at 0.12 m. The antennas were located on the pallets supporting the walls, which placed them at 1.19 m above the floor, roughly chest-height with an adult standing on the turntable. A 0.17-m thick piece of absorbing foam was placed between the antennas to reduce some of the interference between them, but a great deal of interference was still seen. However, the human subject was located outside the range of the residual interference, so the amount did not hamper the detection of the subject.

The turntable was placed between the two antennas at a distance of 6.8 m. In preliminary testing, large reflection peaks were seen from the corner boundary between the ground and the absorbing foam and from a location at roughly 5 m (cause as yet unidentified). The subject location was chosen to lie between these two peaks for ease of identification and to aid in data processing. Additionally, this distance places the subject in the far field of the antennas which was desired; the assumption that the incident field is a plane wave can then be reasonably made. For antennas physically larger than half the wavelength of the emitted radiation (which holds for

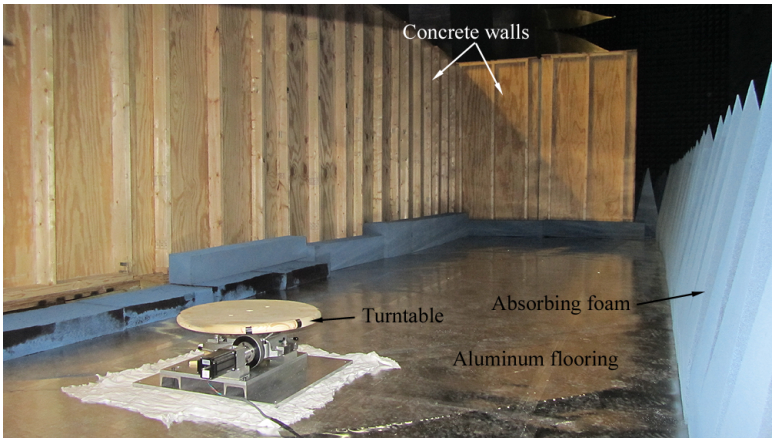

Figure 13. Radar Range. The radar range is viewed from the opposite side of the short concrete wall seen in Figure 10. The long, adjacent wall is seen, along with the turntable on which the human subjects were positioned. The ground is layered with a thick aluminum sheet, and absorbing foam surrounds the perimeter.

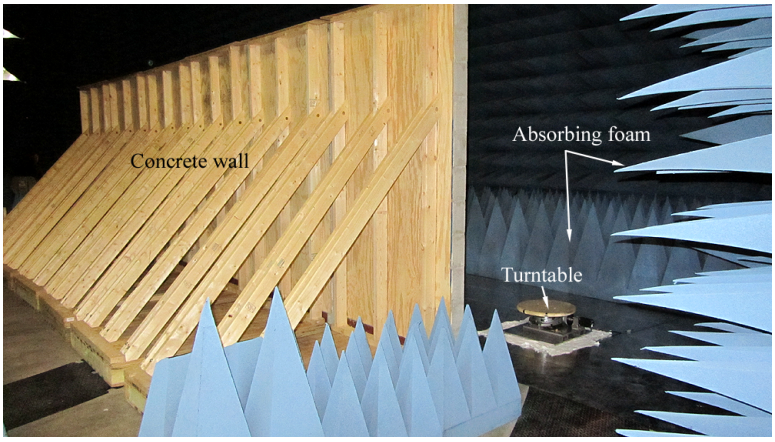

Figure 14. Radar Range and Wall Exterior. Another view of the radar range is seen, displaying the construction of the concrete walls. These walls were built in sections, made of solid concrete blocks sandwiched between plywood and braced by additional wood. The construction avoids any metal hardware within the plane of the wall; hardware is used only in the top and the base of the wall. Additional absorbing foam can be seen, which lines the walls and ceiling of the chamber.

our wavelength range of 0.375-0.75 m), the distance to the far field is given as

$$d_{FF} \geq \frac{2D^2}{\lambda} \tag{89}$$

where d_{FF} is the far field distance, D is the largest dimension of the transmitter, and λ is the wavelength of the emitted radiation. The largest dimension of the transmitting TEM-1 antenna is 0.61 m (24 in). Considering our shortest radiated wavelength of 0.375 m, the greatest distance to the far field is 1.98 m. Thus, the turntable is well within the far field region.

Because the base of the turntable is solid metal, we hoped that placing absorbing foam around the base would help to minimize its radar signal. However, additional peaks were formed due to the corner reflection between ground and foam. These additional reflections were less desirable, so the additional foam was not used. Instead, we chose to subtract the radar signal of the turntable from those of the subjects during the data processing. Photographs of the range displaying the turntable, walls, and surrounding foam are shown in Figures 13 and 14.

Wall Considerations

Next, we will discuss decisions made regarding wall material, construction, portability, and safety. One of the primary goals of this thesis is to model the through-wall, multipath scattering from a human subject. To validate this model, an appropriate wall needed to be constructed for these experiments. Two main considerations went into the selection of material for this wall: the need for a relatively high permittivity to make a multipath model valuable, and the need for a material similar to that used in typical cost-efficient construction.

Propagation of electromagnetic energy through materials depends on the permittivity and the conductivity of the materials. For most building materials, conductivity

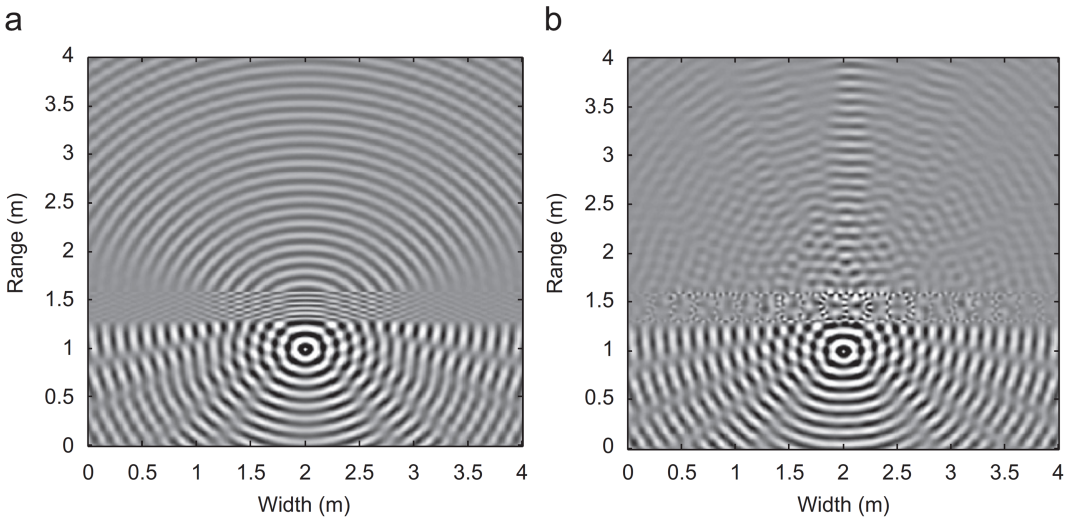

Figure 15. FDTD Concrete Wall Wave Propagation Simulation (reproduced from [2]). a) Homogeneous concrete wall, b) inhomogeneous cinder block wall. For the simulation, both walls were 30 cm, and relative permittivity was 5; a 2.4 GHz sinusoidal source was placed 30 cm from the wall. A well-behaved, spherical wavefront through the solid concrete wall is observed, while the wavefront through the cinder block wall is complex and displays reverberation near the wall. [2]

is low, so permittivity primarily determines the propagation. Concrete has a comparatively high permittivity, compared to materials such as wood. The permittivity of concrete is frequency dependent — it increases with lower frequencies — and varies by composition and moisture content. The composition also varies by supplier. Relative permittivities for concrete vary between 4.5–11 [38, 39, 40, 41].

Given the choice between solid concrete blocks and hollow cinder blocks, the solid concrete was determined to be the material of choice. To simplify modeling, we wanted to have as homogeneous a material as possible, and we expected the large air holes in cinder blocks to introduce unwanted reflections. Ram [2] demonstrated finite difference time domain (FDTD) simulations for both a homogeneous concrete wall and an inhomogeneous cinder block wall (See Figure 15). For this simulation, a 2.4 GHz sinusoidal source was used, the wall thickness was 30 cm, and the relative permittivity was five. As can be seen in Figure 15, the wavefront through the solid

concrete wall remains well-behaved and spherical. The wavefront through the cinder block wall, on the other hand, is complex and shows reverberation near the wall, though it does approach a well-behaved spherical front in the far field. To avoid the complexities introduced by the cinder blocks, solid concrete blocks were chosen as the wall material. These blocks were standard, commercially available, pre-made 4"x8"x16" solid concrete. The relative permittivity of the concrete used in these blocks was estimated to be about 5-6, based on examination of several papers [38, 39, 40, 41].

Due to the size and weight of the concrete wall sections, custom pallets were built to provide the level, durable surface needed to build the sections on, as well as to transport them. Each wall section was located along one edge of its pallet, and extra concrete blocks were built and sealed into the base of the pallet to provide the counterbalance necessary to prevent the wall from tipping. This design resulted in a very safe, sturdy construction. Additionally, the use of metal hardware and fasteners was minimized in the plane of the wall, to prevent anomalous reflections. Metal hardware was used only in the pallets and at the very top of the wall.

Institutional Review Board/Subject Considerations

In order to carry out radar tests on human subjects, Institutional Review Board (IRB) approval is required. The radar was independently tested for safe power levels, and the testing environment was deemed safe for all participants. Additionally, the child tests required the presence of an ombudsman acting as an impartial observer. Extensive coordination was required between these parties, the children and their parents, and care must be taken to plan for this task in future work.

For the duration of the child experiments, the child's parent was required to be in eye-contact with his/her child. To meet this requirement, two locations, chosen

to not interfere with the child's radar signal, were designated as optional observing locations for the parent. One location was about 1 m to the side of the transmitting antenna; the second location was several meters beyond the turntable, and around the corner of the wall, out of direct line of sight of the radar. We determined that each location was sufficiently far from the subject that possible scattering from the parent would not greatly interfere with the subject's signal.

Because of the static nature of the VNA, a continuous 360° image of a subject was not possible, so multiple azimuth measurements were made. We did not expect the subjects, particularly the children, to maintain a stationary position for an extended period of time, so every effort was made to minimize time spent on the turntable. We assumed that humans are bilaterally symmetric with respect to electromagnetic radiation, so only an azimuth range of 180°, front to back, was required. This range was divided into 30 segments of six degrees each for adequate azimuthal resolution, so 31 radar "images" were taken of each subject (30 segments plus the initial starting point). For adequate frequency resolution, we decided that the maximum number of frequency points allowed by the VNA in our bandwidth, 1601, was needed. At this number of points, the VNA takes several seconds to save data. Averaging each radar image was possible in order to reduce spurious signals, but, since this procedure tacks on several additional seconds per collection, it was not done. Additionally, the internal space of the VNA could hold not quite half of the 31 files, so transferring these files to free space during the test took extra time. With these considerations, efficient operation of the VNA and turntable set the minimum time for one subject at about 15 minutes. Subjects could, of course, request that the test stop at any time. Since children were more likely to be unable to stay in one position than adults were, a half-way break time was offered. Footprints were placed on the turntable surface to help the subject return to the same position that was left.

5.3 Experimental Methods and Procedures

Each experiment consisted of measuring the through-wall radar scattering data of a human subject. Thirteen adults and ten children were measured. Each subject (or the child's guardian), was given a consent form to read and sign, their tasks explained, and were offered opportunities to voice any questions or concerns. Afterward, several physical anthropometric measurements were taken and recorded, along with age, for possible correlation with radar data. The measurements were identified only with a letter, F or M to indicate female or male, and a number. Child data was kept separate from adult data. The measurements were done with a tape measure and a flexible measuring tape, over the subject's clothing. They are as follows:

- Height
- Arm length, measured from the tip of shoulder to the tip of middle the finger
- Leg length, measured from the top of the leg, where the leg bends from the hip when lifted, to the floor
- Two torso measurements: around the shoulders and around the waist/belly
- Head circumference, measured just above the brows

The average measurements and age ranges are displayed in Table 5. After collecting the measurements, the subject was led to the turntable to begin the radar tests.

Before each block of tests for the day, the calibration of the VNA was ensured, as well as the following operating parameters:

- Frequency range set to 400–800 MHz
- S21 transmission (S21 is the response at port 2 due to a signal at port 1, essentially the forward transmission)
- Averaging set to OFF
- Number of Points set to 1601

Table 5. Average Anthropometric Measurements.

	Range or Avg. Value	
Measurement (years or inches)	**Adult**	**Child**
Age	20-52	5-12
Height	69.6	52.8
Arm length	27.6	20
Leg length	37.1	26.9
Shoulder circ.	47.4	32
Stomach circ.	39.6	23.8
Head circ.	23	20.8

- Save format set to ASCII, Touchstone (saves the real and imaginary components of the signal)

After clearing the buffer in the custom LabView turntable software via the laptop and setting the rotation to 6°, the experiment was ready to begin.

A typical experiment began with the subject on the turntable, facing the antennas through the concrete wall, at 0°. The command "START" was given, which indicated to the subject that the signal was about to be recorded. At this command, the subject was requested to maintain a stationary, natural position with arms at sides, facing forward. After the data was recorded, the command "REST" was given. This command indicated that the turntable would be advanced 6° and that the subjects could move as they liked. We asked that the subjects not shift their feet in order to aid in returning to the former stationary position when the next "START" command was given. The test proceeded with alternating START and REST commands, for 31 total positions, until the last position was reached at 180°. For child subjects, parents were offered the option of relaying the commands to their child. The option of a "Simon Says" game was suggested in order to help make the process more enjoyable and the child more likely to participate effectively.

Two minor delays in each data collection were experienced as a result of transferring data files from the VNA's internal memory to an external drive via the networked laptop. Additional short delays were possible due to occasional hang-ups in the turntable software. These hang-ups did not interfere with the operation of the turntable itself, but they did require that the turntable be unplugged from the laptop and plugged back in, in order to reset the software.

Once the data collection was complete, the radar data was transferred to a secure hard drive for safe keeping and data processing. The procedure for the data processing is explained in the following section.

5.4 Data Processing

All data processing was accomplished in Matlab. The processing of the radar data aided in identification of the subject in the data, as well as identification of radar characteristics of the subject, such as resonance regions. Additionally, we explored various processing workflows before applying the SVM classifier, in order to determine the type of processing that allows the SVM to operate at peak performance. Processing generally included windowing, filtering, and sphere calibration, as well as isolation of only the data points immediately surrounding the subject, in the range (time) domain. Further, to reduce the dimensionality of the data with the goal of minimizing the training process, certain characteristic features of the range domain data were chosen for testing, as well. In general, background subtraction was not performed, as it would have removed the effects of the walls in the data. Additionally, background subtraction may not be available in many real-world scenarios. In some of the processing, however, the subtraction of the turntable signal was done. The primary processing steps of windowing, filtering, and sphere calibration are described below, followed by the isolation of surrounding data points and feature extraction.

Windowing

The application of a data window is useful in situations where low-level signals become masked by contributions from nearby high-level signals, causing the lower signals to be difficult to identify. Data windowing isolates the signal of interest while gracefully degrading the contribution of nearby secondary signals. [42]

Due to the signals from the walls, floor, and boundaries between the floor and the absorbing foam, windowing was chosen as the primary data processing step in order to better separate the signals of the human subject from the environment. To provide graceful degradation, the window used was a Hamming window [42]:

$$w(k) = \begin{cases} 0.54 + 0.46 \cos \frac{\pi k}{M} & \text{if } |k| \leq M \\ 0 & \text{if } |k| > M \end{cases} \tag{90}$$

where M is the length of the window. We applied the built-in function *hamming* in Matlab to the frequency domain data.

Filtering

Windowing in the frequency domain filters in the range domain and visa versa, so we will refer to windowing in the range domain as filtering. Due to through-wall effects and radar system resolution, the subject at 6.8 m appeared in the radar data at about 8.1 m. The filter was centered at this location and is displayed in Figure 16. In order to include additional reflections due to the area immediately surrounding the subject, the filter width chosen was 3 m, with a taper to zero at 5-m width found to produce a satisfactory result. The filter was created with Matlab's *firpm* and *freqz* functions, and multiplied against the range-domain data. In Figure 16, the Ideal filter is the smooth, step-like function. The Matlab *firpm* filter is the oscillatory function.

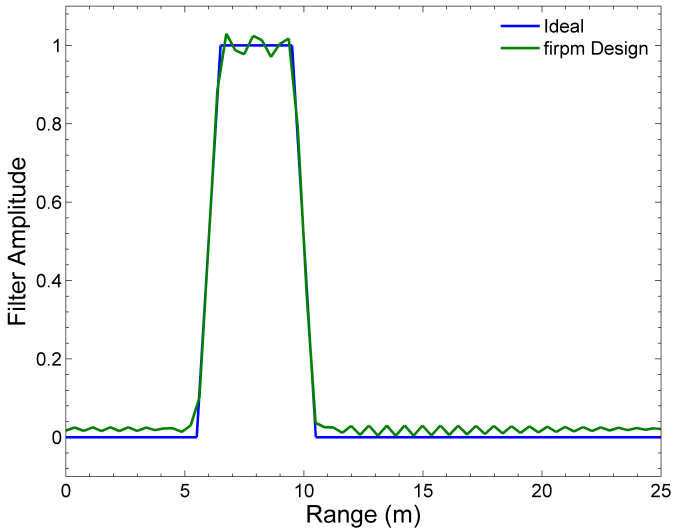

Figure 16. Matlab Filter. The frequency filter was designed with Matlab's *firpm* and *freqz* functions. Shown as a window in the range domain, each filter spans the full range of the inverse Fourier transformed data (range/time domain), but only the range of interest is displayed here, showing the difference between the ideal filter (smooth line), and the accepted filter produced by the Matlab functions (oscillatory line). This filter provides a 30 dB suppression of data surrounding the subject location.

Sphere Calibration

Mie scattering is an analytical solution to Maxwell's equations based on the scattering of electromagnetic radiation from a sphere. Because we can calculate the Mie scattering from a sphere in free space, the comparison of this scattering solution to the measured scattering of a sphere in some other environment can demonstrate how that environment impacts the scattering of the sphere. The difference between the Mie and measured scattering, once known, can also approximate the difference between a human subject measured in the same environment, and the "perfect" scattering from a human subject that would be observed in free space. The following calibration technique is based on [43].

Let us call the measured scattering from a sphere in our chosen environment S_{sph}, and the calculated Mie scattering from a sphere of the same size S_M. The ratio

between these is the calibration factor C_F:

$$\frac{S_{sph}}{S_M} = C_F \tag{91}$$

During the experiment, S_{sph} was collected from a 25-cm calibration sphere, in the same environment as our test subjects, with the corner-wall setup. Thus, because the calculated scattering S_M is that of a sphere in free space, the calibration factor will essentially remove the effects of the walls from the calibrated human radar data.

Now, the measured scattering from a human subject in our chosen environment is S_{meas} and the "perfect" scattering from the same subject in free space is S_p. Employing the approximation that these two scattering profiles are related by the same calibration factor, we have:

$$S_p = \frac{S_{meas}}{C_F} \tag{92}$$

Thus, we can determine the "perfect" scattering of our subject with knowledge of the measured scattering of the subject, the measurement of a calibration sphere in the same environment, and calculation of the Mie scattering from that sphere.

When our scattered signal is represented by the received signal power from Equation (16), reproduced here,

$$P_r = \frac{P_t G_t}{4\pi R^2} \frac{\sigma}{4\pi R^2} A_e \tag{93}$$

the signal ratio becomes a ratio of the radar cross sections σ of the subjects. Furthermore, when operating in log-magnitude, the ratio becomes a simple subtraction.

Since this calibration includes the effect of the walls, this processing method is not ideal for comparing the differences between child and adult subjects when the impacts of the through-wall and wall scattering are under consideration. However, it can be employed to observe the changes that the through-wall environment makes on the radar signature of a person.

Feature Extraction

Feature extraction refers to the isolation of certain features seen in the data which represent the essential characteristics of the subject's radar signatures. Feature extraction can be done in either the time or the range domain; here, it was done in the range domain.

A simple method of feature extraction is simply the isolation of the data points near the peak representing the subject's location in the range domain. This extraction is similar to another window applied to the time domain (filtering in the previous discussion), but points other than those of interest are thrown out, rather than having their amplitudes suppressed. For this simple isolation, seventeen points were chosen, spanning the width of three peaks — those of the subject, the reflection at the boundary between the aluminum flooring and the absorbing foam behind the subject, and another reflection in front of the subject. These features were chosen based on the idea that the presence of the subject may have the most influence on its immediate surroundings due to multiple reflections. The other points were discarded.

Another attempt at feature extraction was the determination of values describing the main peak of the subject in the range domain: the magnitude of the subject's peak and the two nearby peaks, the height of the subject's peak, referenced from the valleys on either side, and the width of this peak. These values represent six features in total.

There were not any recognizable features in the frequency domain for the through-wall data, so manual feature extraction was not applied directly to this domain. However, when this data is calibrated using the Mie scattering, resonance peaks are observed, which may allow for feature extraction. The goal of the classifier, however, was to classify when effects of through-wall scattering are present. Because Mie calibration reduces these effects, feature extraction was not used on this data.

5.5 Principal Components Analysis

Principal Components Analysis (PCA) is a common statistical technique to identify patterns in data with high dimension, and to express the data in a way that illustrates those patterns. A graphical representation of the data can be achieved by reducing the dimensions of the data to allow plotting in two or three dimensions. In our particular case, the radar data is high dimensional, consisting of 1601 dimensions — one for each frequency step from 400 to 800 MHz. Since the Support Vector Machine also operates in a high-dimensional space, it does not allow the convenient visualization of the data to show the derived hyperplane boundary that separates data classes. In contrast, PCA aids in reducing data dimensionality to allow a visual representation of the data, and any separation that exists, provided this separation can be expressed in two or three dimensions. The following briefly describes the steps of PCA. These steps are reproduced from Smith's *A Tutorial on Principal Components Analysis* [44], with some change in notation.

Suppose our data consists of measurements x_i, where $i = 1, \ldots, n$, where n is the total number of measurements. For each measurement, we can represent a specific data point as x_{ij}, where $j = 1, \ldots, m$ is the dimension of the measurement. In the example of the radar data, each measurement x_i consists of the scattering data for a single azimuthal view of a subject, and the dimensions $1, \ldots, m$ are the value at each frequency step for that azimuthal view.

The first step of PCA is to subtract the mean from each data dimension [44]. We can represent our entire data set as a matrix D, with each measurement a row vector

i, and each column a dimension j of the data:

$$D = \begin{Bmatrix} x_{11} & x_{12} & x_{13} & \dots \\ x_{21} & x_{22} & x_{23} & \dots \\ & \vdots & & \ddots \end{Bmatrix} \tag{94}$$

Each dimension can be represented generally as d_j, so that the mean of each dimension is $\bar{d}_j$. We then subtract the dimensional mean from each column and obtain the mean adjusted data matrix:

$$D_{adj,ij} = D_{ij} - \bar{d}_j \tag{95}$$

The second step is to find the covariance matrix of the data [44]. The covariance measures the variation of the dimensions with respect to each other. The elements of the $m \times m$ covariance matrix C are given as

$$C_{pq} = \mathrm{cov}(x_p, x_q) = \frac{1}{n-1} \sum_{i=1}^{n} (x_{ip} - \bar{d}_p)(x_{iq} - \bar{d}_q) \tag{96}$$

where the elements C_{pq} are the covariances of the columns or dimensions $j = p$ and $j = q$ of the data matrix D.

The next step is the calculation of the eigenvectors and eigenvalues of the covariance matrix. This will allow the expression of the data in terms of the orthogonal eigenvectors rather than the original dimensions, which may or may not be orthogonal. Additionally, the eigenvectors describe patterns in the data, and those eigenvectors with the largest eigenvalues describe the strongest patterns. The highest eigenvalue is then the *principal component* of the data set. [44]

5.6 Classification Process

Classification of the radar scattering data involved the use of the Support Vector Machine (SVM) program created by Erdmann [45]. A Support Vector Machine is a binary classification tool and its concept is described in Appendix B.

The SVM trains on a subset of the data, and tests on another subset, which is distinct from the training set. In order to train on the data, adult vectors were identified with a classification of -1, and child vectors a classification of $+1$. The SVM then tested on an unclassified set of the data, and compared its success with the known classification vector to determine its accuracy.

In order to generalize the performance of the SVM, the classifier was run for four different combinations of testing and training data, with the testing set comprising 25% of the adult vectors and 25% of the child data vectors, and the training set comprising the other 75% of both adult and child data vectors, for each combination. The training sets did not contain any of the data from their corresponding test sets. These sets are visually illustrated in Figure 17. The accuracies for all four combinations were averaged in order to determine the overall accuracy of the SVM.

This classification was done for various data processing methods. In the time domain (consisting of 1601 points), the levels used were unprocessed data, windowed data, windowed plus filtering, and windowed and filtering combined with Mie calibration. These four levels were also tested with frequency domain data. Additionally, a set of windowed and filtered data was isolated to seventeen data points surrounding the subject's range domain peak for another classification attempt. The final classification attempt involved a set of six features extracted from the range domain windowed data.

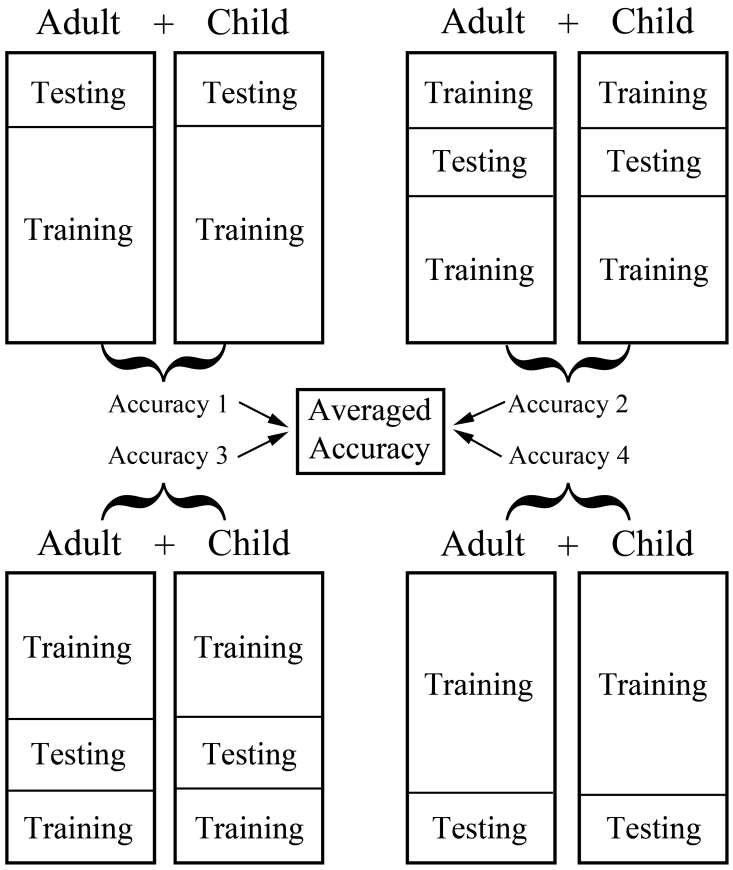

Figure 17. SVM Implementation Procedure. Each classification attempt followed the procedure illustrated above. Both the child and adult data were divided into fourths, which represented blocks of data that would test the SVM. For a single SVM run, one fourth of both the child and adult data was tested on, with the remaining 3/4 acting as training data. Four SVM runs were accomplished, each run testing on a different fourth of the data. The accuracies from the four runs were averaged to determine the overall accuracy. This process characterized the procedure for classifying the data at each processing level.

5.7 Procedure Summary

The summary of the above experimental procedures is as follows:

1. Ensure calibration of radar equipment; set operating parameters (Section 5.3).
2. Introduce tasks to the volunteer, explain the consent form and have the form signed.
3. Take anthropometric measurements (Section 5.3).
4. Lead the volunteer to the turntable.
5. Take radar measurements following the "START/REST" procedure (Section 5.3).
6. Continue from #2 with testing additional volunteers as needed.
7. Process radar data: windowing, filtering, Mie calibration, and/or feature extraction (Section 5.4).
8. Perform SVM classification of radar data (Section 5.6).
9. Perform PCA analysis of radar data (Section 5.5).

The radar scattering profiles, Support Vector Machine classification, Principal Components Analysis results, and final discussion are presented in the next chapter.

VI. Results and Discussion

This chapter presents the results of the through-wall adult and child radar measurements, in both the frequency and range (time) domains. These scattering profiles are processed for better visual identification of the subject, and application of Mie calibration recovers the free space human scattering profile for comparison with the through-wall profile. Support Vector Machine (SVM) classification is done for various processing levels in order to determine the processing necessary for ideal SVM performance, and to determine the success rate of identifying a child or adult presence from behind a wall. This method was initially chosen because of the availability of existing SVM code and because it is a common classification method. Finally, Principal Component Analysis (PCA), a statistical technique for examining high-dimensional data, is performed on selected processing levels in order to aid the investigation into the SVM performance.

The first section displays typical child and adult measurements seen during the experiment, and the second section reports the classification results. The last section discusses PCA results and connects these with SVM classification performance.

To get copies of any radar or anthropometric measurements used in this project, please contact AFRL/RYMD. In accordance with IRB protocols, all data are non-identifiable and cannot be traced back to any of our volunteers.

6.1 Measurements

The data consists of thirteen adults and six children. The children were aged 5-12 years, and adults 20-52 years, so there was an age difference of at least 8 years between the oldest child and youngest adult. Each subject was observed by the radar at multiple angles. For most subjects, we have 31 vectors of data, corresponding to

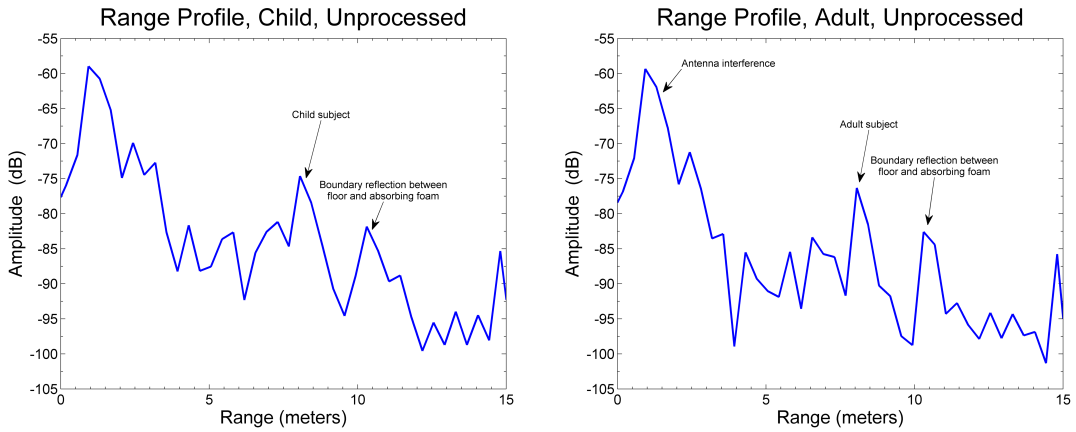

Figure 18. Typical Range Profiles of Adult and Child Subjects, Unprocessed. The subject peak can be seen at about 8 m, with the boundary reflection between the aluminum flooring and absorbing foam at about 10.3 m. The cross-talk between the transmitting and receiving antennas is seen at 1.3 m.

30 individual angles through a 180 degree azimuth sweep, plus the starting angle at zero degrees. However, two of the adult subjects had missed views; and for two of the children we needed to cut down the total number of views to five and ten, respectively, since they were too energetic to remain a test subject for long. Altogether, we had 389 adult vectors and 139 child vectors, each with 1601 frequency points spanning 400×10^6 to 800×10^6 Hz.

For the goal of child/adult classification, the most useful type of imaging for our radar data is the display of the signal amplitude in either the time or frequency domains. Unprocessed, the frequency domain displays no obvious points of interest, so we begin by examining the time domain. Figure 18 shows the unprocessed time domain data in our range of interest, from 0 to 15 m, for a typical frontal view (0 degrees azimuth) for a child and adult. The peak at 8 m is the subject; the peak at 10.3 m is the boundary reflection between the aluminum flooring and the absorbing foam, determined through experiment. The peak at about 1.3 m represents the combined interference between the antennas and the obstructing wall. In the unprocessed data, some overlap between the subject's signal and other peaks, particularly at shorter

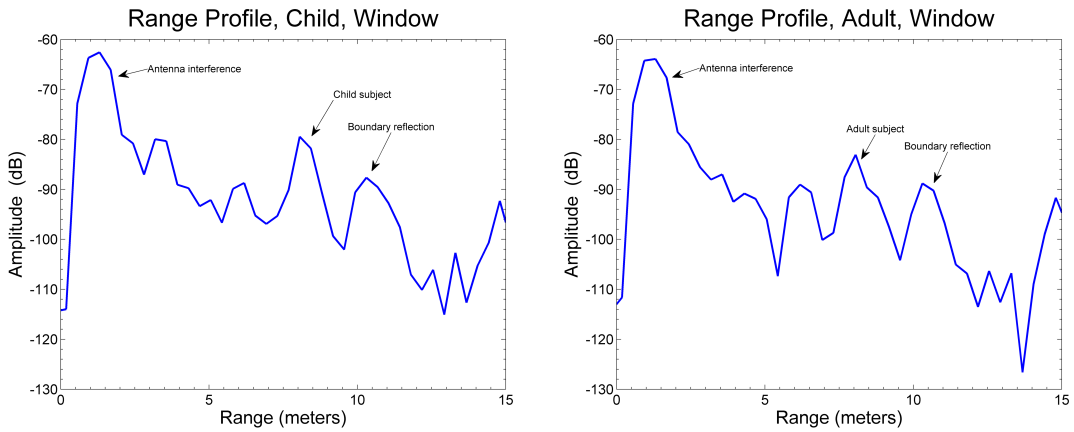

Figure 19. Typical Range Profiles of Adult and Child Subjects, Windowed. The same peaks are observed as in the unprocessed data, however, the target peak has been separated more cleanly from the surrounding signal. A Hamming window was used in the processing of all windowed data. There is no obvious feature to distinguish the peak of a child from that of an adult.

distances, can be seen.

Typical windowed data is shown in Figure 19, for the same data as that displayed in the previous figure. The windowing in the frequency domain has the effect of smoothing many of the jagged peaks seen in Figure 18. Inspection reveals no obvious differences, although the child peak appears thinner, without the shoulder characterizing the adult peak. Averaging the child and adult data results in even broader peaks and is not very enlightening (Figure 20). The shape, on average, of the child peak is very similar to the adult's, thought it does tend to be slightly lower. We see that the evidence we seek is not in the average but perhaps we can find it in the detail. Either further processing is required, or a simple visual inspection is insufficient to reliably distinguish child from adult.

Figure 21 displays the effect of filtering on the windowed data, for the same adult data seen previously. The filter provides about a 30 dB suppression of the signal surrounding the subject peak. As indicated in Section 5.4, the peaks immediately surrounding that of the subject are intentionally preserved. Although filtering en-

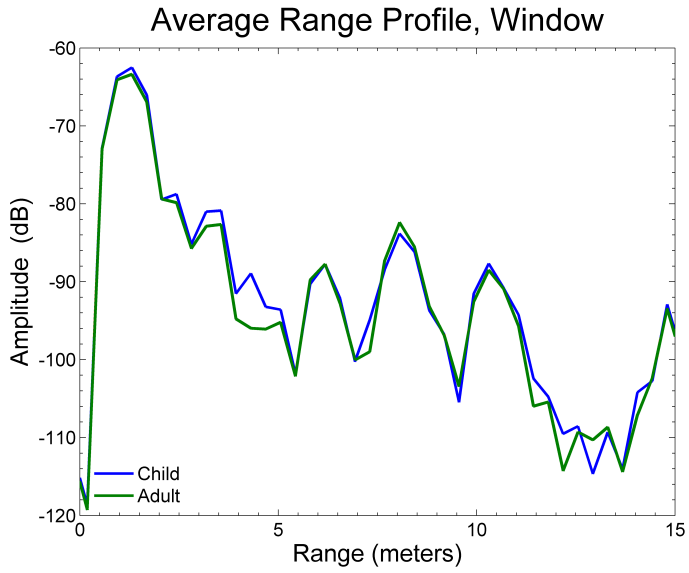

Figure 20. Average Child, Adult Time Domain Data. When averaged, the child and adult time domain data are shown to be very similar — the profiles lie almost on top of each other. A simple visual inspection is not enough to distinguish the child profile from that of the adult.

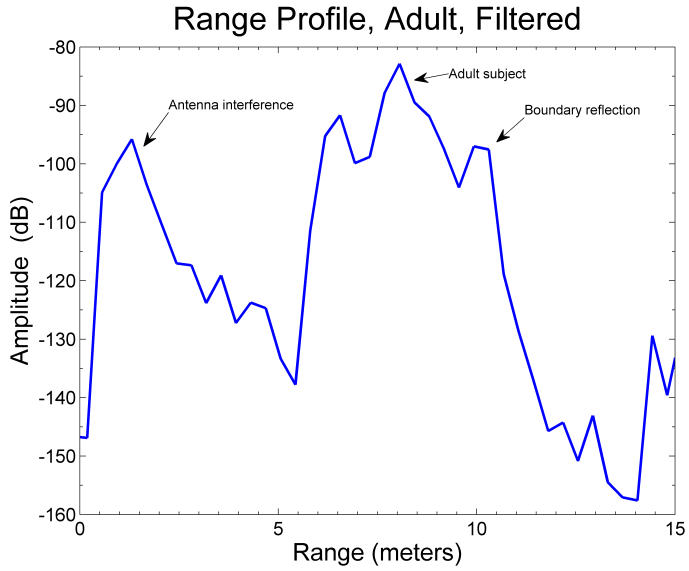

Figure 21. Typical Range Profile of Adult, Windowed and Filtered. Again, the subject, boundary reflection, and cross-talk peaks are observed. The peaks comprising the subject and surrounding reflections have been enhanced compared to the rest of the signal, which has been suppressed by about 30 dB. This plot displays the same data as that seen in Figures 18 and 19.

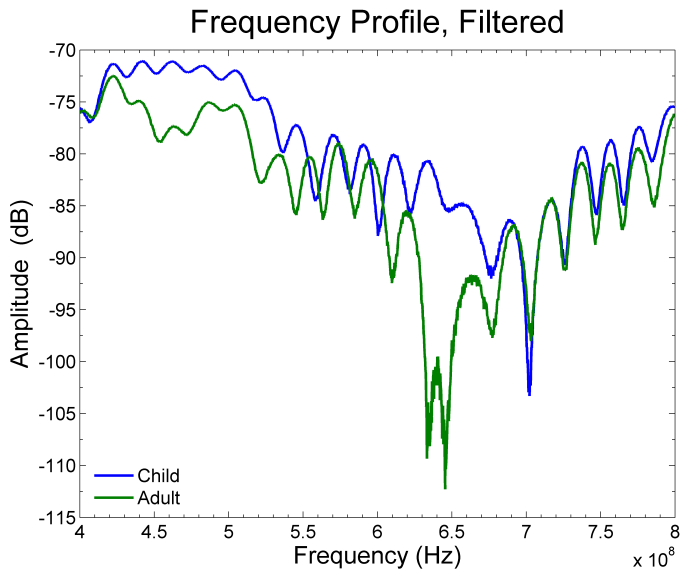

Figure 22. Typical Frequency Profile of Adult and Child, Windowed and Filtered. The processed data from the prior figures is shown. In comparison with the Mie calibrated data in Figure 23, the well-formed resonance peaks have been suppressed by the effects of radar propagation through the obstructing wall, although matching rounded peaks are still observed. The overall oscillatory behavior between the two figures is preserved, as well as the valleys at 650 and 700 MHz.

hances the view of the subject in the range domain, we will see in the next section that it has little effect on the classification success of the Support Vector Machine. Figure 22 shows the filtered data in the frequency domain, for the same views of the child and adult seen so far. In comparison with unfiltered, unwindowed data (not shown), the filtered data in the frequency domain displays much more structure, as the contribution of the frequencies from the subjects are enhanced compared to those from surrounding surfaces.

The final processing step is Mie calibration. From work described in Section 3.2, we know that an ideal, free space human scattering signature will display resonances at roughly 550 MHz. After calibration, we see this same signature in both the child and adult data (Figure 23). Rescaling the horizontal axis and overlaying with the frequency plots from Section 3.2 reveals that these are the same resonance peaks. The rest of the scattering structure also matches quite well with the prior data.

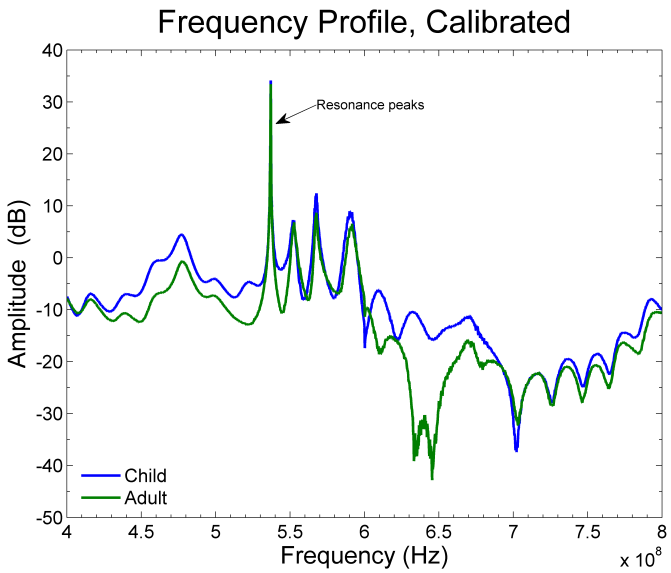

Figure 23. Typical Frequency Profile of Adult and Child, After Mie Calibration. The Mie calibrated data from the prior figures is shown. Resonance peaks and the overall behavior of the plot match those seen in Figures 3 and 4 of the line-of-sight scattering of the child and adult substitutes, in the frequency range of 400-800 MHz.

Although the goal is to classify child and adult signatures with the effects of the walls included, comparison of the Mie calibration results and the uncalibrated results of Figure 22 (which both include windowing and filtering as part of the processing) display the effect that the obstructing wall and multipaths have on the data. The well-formed resonance peaks are masked by the wall, although we do see a collection of four rounded peaks between about 520 MHz and 620 MHz which match those in the calibrated data. The drops in amplitude of the child and adult data near 650 and 700 MHz are preserved, as well as the overall oscillatory nature and general shape of the data. Although specific features of the frequency domain data have not yet been extracted for the purposes of classification, the location and magnitude of the peaks and valleys, in either the uncalibrated or calibrated data, may provide a reliable feature set with which to classify child from adult.

To demonstrate the overall comparison between child and adult data, the average unprocessed frequency data and the average Mie-calibrated frequency data are shown

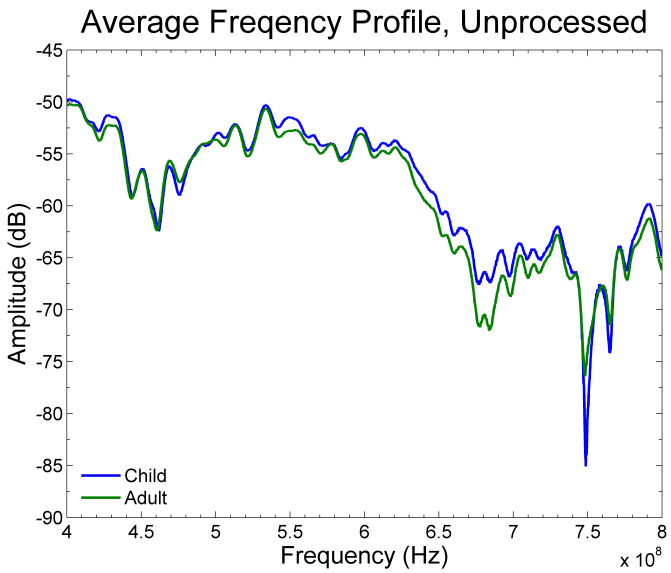

Figure 24. Average Frequency Profiles of Adult and Child Subjects, Unprocessed. This data has been averaged over all azimuthal views of each child and adult subject. On average, the child profile is higher than that of the adult, with a deeper valley at 750 MHz.

in Figures 24 and 25, respectively. Overall, the child signature remains slightly higher than the adult signature in Figure 24. Comparing this figure with the average of the Mie calibration, we see that, not only is the adult magnitude higher in the averaged, calibrated data, but some of the variation between the two signatures appears to have diminished. Additional processing in the frequency domain may reduce the variation between the child and adult data with the loss of scattering information. Evidence of this reduction will be seen in the next section with the performance of the Support Vector Machine.

6.2 Subject Classification

The purpose of the Support Vector Machine is a binary classification of child/adult, so the SVM essentially views each vector as a separate data point with 1601 features or dimensions. We needed the SVM to view each vector as a unique adult or child,

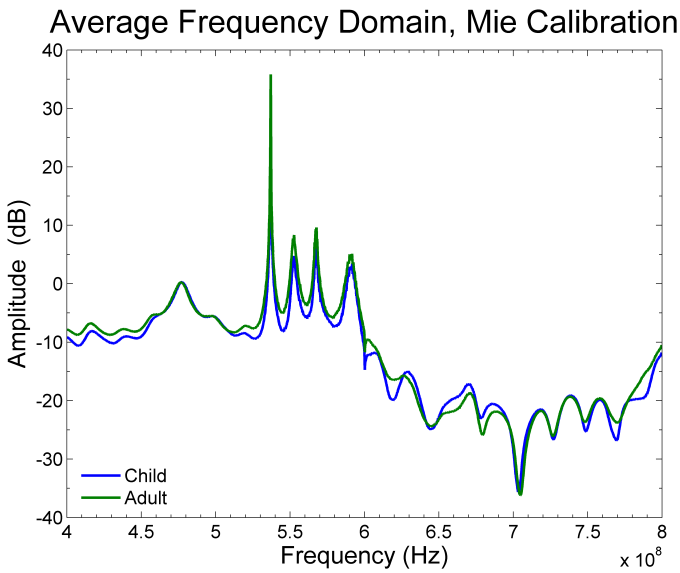

Figure 25. Average Frequency Profiles of Adult and Child Subjects, Mie Calibration. This data has been averaged over all azimuthal views of each child and adult subject. In comparison with Figure 24, the Mie-calibrated data appears to display less variation between child and adult.

as well. Because there may be correlations between azimuthal vectors of the same subject, the vectors of each subject were concatenated together, forming one long vector for that subject, consisting of the scattering data at each frequency, at each azimuthal angle. This process is illustrated in Figure 26. Additionally, because the SVM required all data sets to be of the same length, we needed to reduce the number of azimuthal angles presented to the SVM to those of the subject with the fewest available angles. This subject was the child with only five angles of data: at 0, 45, 90, 135, and 180 degrees, azimuth. To keep consistent angular data across all subjects, the concatenated data vectors were created with the five angles chosen to match, as closely as possible, those of the child. The angles did not match exactly, because most subjects were measured at azimuthal increments of 6 degrees, rather than 45. However, the angles chosen were within 10 degrees of the child data. One adult subject did not have azimuthal data above 90 degrees, so this subject's data was not included in the final set of data presented to the SVM. The final data set consisted of

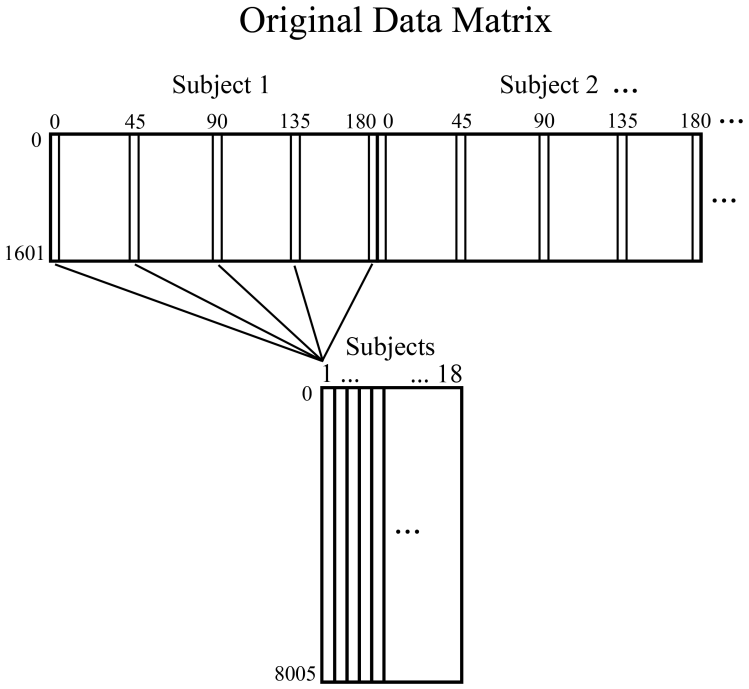

Figure 26. SVM Data Matrix Construction. The original radar data matrix consisted of 31 vectors for each subject, spanning 0 to 180 degrees azimuth, each vector consisting of 1601 points. For the SVM to classify based on individual subjects, the vectors closest to 0, 45, 60, 135, and 180 degrees were extracted to form a single vector for each subject, consisting of 8005 points. The final data matrix then consisted of 18 vectors, one for each of the 12 adults and 6 children.

12 adult vectors and 6 child vectors, one vector per subject. Each vector consisted of five azimuthal views — 0, 45, 90, 135, and 180 degrees — for 8005 frequency points in total.

Table 6 displays the classification accuracy results of the SVM, based on this reduced data set. The accuracies are listed with the overall accuracy first, which is then broken down into the individual adult and child accuracies. These accuracies describe how well the SVM was able to classify the given child and adult data.

Table 6. SVM Results. Win = Windowing, Filt = Filtering, Mie = Mie calibration, Iso = Isolation of a range of data points, Feat. Ext. = Extraction of certain features from the data.

			Avg. Accuracy (%)		
Background Subtraction	**Domain**	**Processing**	**Overall**	**Adult**	**Child**
None	**Time**	**None**	60	100	0
		Window	60	100	0
		Win+Filt	60	100	0
		Win+Filt+Mie	70	92	38
	Freq	**None**	100	100	100
		Win	100	100	100
		Win+Filt	95	100	88
		Win+Filt+Mie	45	75	0
Turntable Only	**Time**	**Win**	60	100	0
		Win+Filt+Iso	100	100	100
		Win+Feat. Ext.	95	100	75
	Freq	**Win**	100	100	100

First, a note of caution on relying upon these SVM results. Our data set was very small, and the test sets consisted of only three adults and two children upon which to base the classification accuracies. Additionally, the training set of adults was larger than that of the children, introducing bias toward adult classification. This bias likely accounts for instances such as in the time domain data with no processing, where the accuracies list 100% for adults, but 0% for children.

With regards to time domain classification and no background subtraction, the

highest accuracy is obtained with Mie calibration, with no gain from either windowing or filtering, for an accuracy of 92% (adult) and 38% (child). Accuracy of 100% is obtained for both unprocessed and windowed frequency data; further processing reduces this accuracy. When the signature of the turntable is subtracted from the time domain data, we see no improvement in accuracy until the two feature extraction methods are done. "Iso" refers to isolating the data points immediately surrounding the subject peak with all other points removed. "Feat. Ext." refers to extracting the characteristic dimensions of the subject peak, such as height and width. These techniques provide the highest accuracy seen for time domain data: 100% for peak-isolation, and 100% (adult)/75% (child) for the peak dimensions. Although this accuracy requires additional processing and is not as high as that obtained by the unprocessed time domain data in the case of the peak dimensions, the SVM is significantly reduced in its complexity due to the low dimensionality — i.e., 1% of the total data set. The SVM is also more likely to classify without memorization or overtraining. Turntable subtraction has no effect on the frequency domain data.

In an effort to better understand the nature of the data, and to determine why there is an apparent better separation between child and adult data in the unprocessed frequency domain than in the time domain, we conducted an investigation using Principal Components Analysis (PCA). This investigation allows us to examine the performance of the SVM with a method that, because of our small data set, is more reliable. The following section briefly describes the implementation of PCA, and provides a visualization of the data separation and further discussion of differences observed between the data sets.

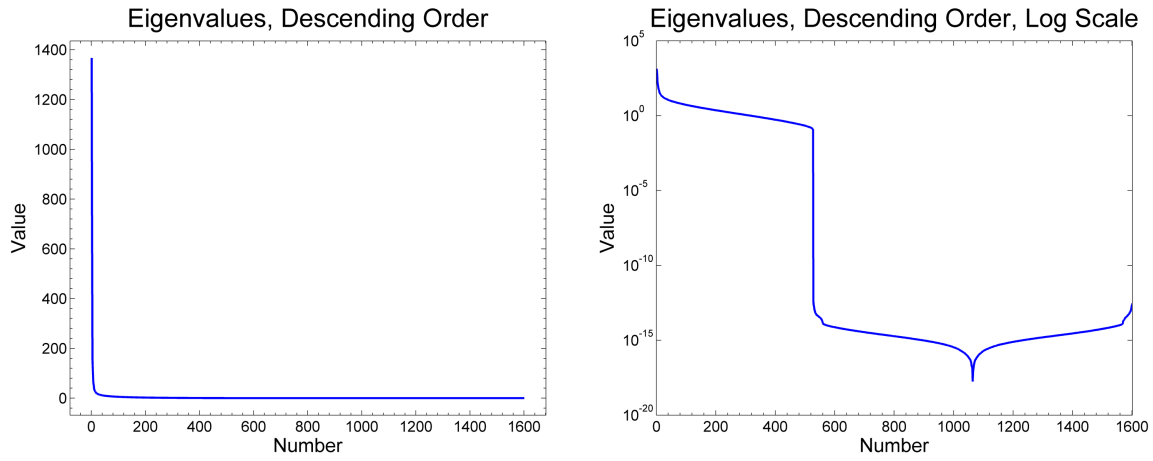

Figure 27. Eigenvalues of Unprocessed Frequency Data. The ordered eigenvalues of the unprocessed frequency data covariance matrix are shown. A non-logarithmic plot is shown on the left. It is shifted slightly from the left axis to better display the line. The same plot is shown on the right with a logarithmic scale. The absolute value of the eigenvalues were plotted here; negative values account for the "reversal" of the line near 1040 on the x-axis. The eigenvalues are numbered along the x-axis from 1 to 1601. The three highest eigenvalues are on the order of 10^3, and were used to choose the eigenvectors to form the reduced data sets.

6.3 Principal Components Analysis Results

Using the Principal Components Analysis (PCA) procedure described in Section 5.5, we calculated eigenvectors for the radar data. The eigenvalues are shown in Figure 27.

Once the eigenvalues and their corresponding eigenvectors have been found, we order the vectors in descending order according to their eigenvalues. From this ordered set, we can choose to ignore the vectors of lesser significance — those with small eigenvalues. This selection process leaves us with a set of reduced dimensions. Information is lost, but the amount we hope is minimal if the removed eigenvalues are small. The eigenvectors kept form a $m \times k$ *feature vector* F, where k is the number of eigenvectors kept [44]:

$$F = \left\{ eig_1 \quad eig_2 \quad \dots \quad eig_k \right\} \tag{97}$$

The eigenvectors are the columns of the feature vector matrix. For the purposes of displaying the data in a three-dimensional plot, we keep only the three eigenvectors associated with the three largest eigenvalues; the dimensions of our feature vector for the radar data is therefore 1601×3. These eigenvectors will form the axes of our plot. [44]

The final step is the derivation of the new data set. This final data set is [44]

$$D_F^T = F^T \times D_{adj}^T \tag{98}$$

where T represents the matrix transpose, and D_{adj} is the mean adjusted data matrix, found in Step 1. With this operation, we obtain our reduced dimensionality data set D_F in terms of the chosen eigenvectors. Limiting the eigenvectors to three allows a visual representation expressing the three dominant data dimensions.

A visual representation has now been achieved. We can determine the effect that the reduced dimensionality has on the original data set by the following operation [44]:

$$D_R^T = F \times D_F^T + \bar{D} \tag{99}$$

where D_R is the recovered, reduced dimensionality data, transformed by the feature vector, and $\bar{D}$ is the matrix of the means of the original data. This expression allows us to reverse the PCA process. This recovered data may be compared to the original data to determine what information was eliminated by the PCA process. Ideally, the number of eigenvectors chosen will result in minimal information loss, and the recovered and original data will be similar in structure [44]. Our choice of three of 1601 eigenvectors is due to the need to visually represent the data, and is not meant to be an optimal data reduction. However, comparison of the original radar data with the recovered data shows minimal changes.

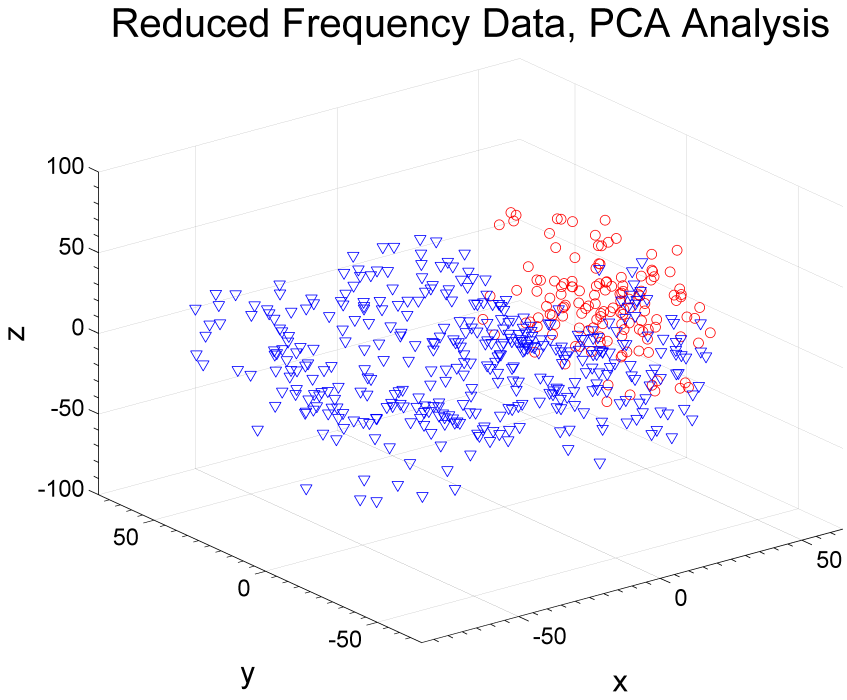

Figure 28. PCA of Child and Adult Frequency Data. The data represented in the plot is D_F, obtained during the final step of the PCA process. Child data is shown as the red circles, and adults as the blue triangles. Each point represents one azimuthal view of a subject, plotted with respect to the three largest eigenvectors. The eigenvectors form the axes of the plot: the x-axis is the largest eigenvector, y-axis the second largest, and z-axis the third. From this view, we see that the child data forms a distinct cluster.

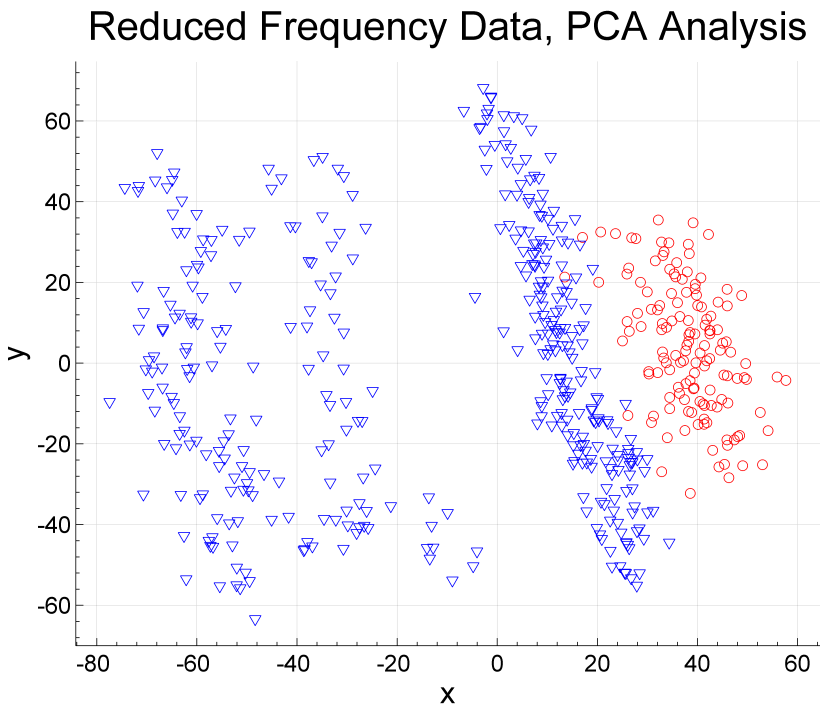

Figure 29. PCA of Child and Adult Frequency Data, XY Plane. This displays the data seen in Figure 29, but now viewing only the xy-plane, which contains the strongest relationships between the data. The data separation is much clearer in this view; the child data is restricted to the right of the plot (red circles), demonstrating that a reasonable separation plane may be placed between the child and adult data (blue triangles). From this view, we can see that the strongest pattern in the data lies along the x-axis, as expected; this is primarily where the division between child and adult data can be seen. Additionally, there exists at least two, possibly three distinct groupings of adult data, also shown primarily along the x-axis.

The PCA process was conduced on the unprocessed frequency data, in order to provide a way of visualizing the separation between the child and adult classes, and to explore whether the Support Vector Machine was overtraining on the data. The relationship between the data obtained during the PCA process is shown in Figure 28, specifically the data contained in D_F. In Figure 28, the x, y, and z-axes are the first, second, and third-largest eigenvectors, respectively, and each point represents one azimuthal view of a subject, plotted with respect to the three largest eigenvectors. This representation displays the three strongest patterns contained in the data. A strong grouping of the child data is seen (red circles) toward the right of the plot.

We hypothesized that the strongest pattern in the data (the x-axis), has the most potential to demonstrate any strong differences, such as that found by the Support Vector Machine between the child and adult frequency data, leading to the highest classification accuracy. Indeed, when we rotate the view to show the xy-plane (Figure 29), this is clearly seen. The separation is much more evident in this view, with a clear boundary between the adult data on the left, and the child data on the right demonstrating strong clustering. The y-axis also demonstrates a pattern, but to a lesser extent, indicated by the more condensed grouping of child data in the y-direction, compared to the adult data. Additionally, two to three distinct groupings of adult data can be seen, suggesting that further classification between adults may be possible. This clear separation in the data, combined with the SVM process of averaging quarters of the data, helps to demonstrate that the SVM did resolve structure in the data and may not have overtrained. There is, indeed, a strong division between unprocessed child and adult frequency data.

Additional investigation into results of two other data processing techniques was conducted to visually determine the differences in SVM accuracy, and to further support the observation that unprocessed frequency data allows the highest SVM performance. These two data sets were the unprocessed time domain data, which had an SVM classification accuracy of 78%, and the isolated time domain subject peak data, which achieved an accuracy of 94%. The results are shown in Figures 30 and 31. Comparing the two figures, we see that the time domain data shows very little clustering in the classes, though child data appears shifted more toward the positive x-direction than the adult data. The peak-isolated data demonstrates better clustering, specifically in the child data. This corresponds with the SVM's relatively poor accuracy in time domain classification, but improved accuracy when only peak data points are considered. Additionally, the extra groupings of adult data are lost.

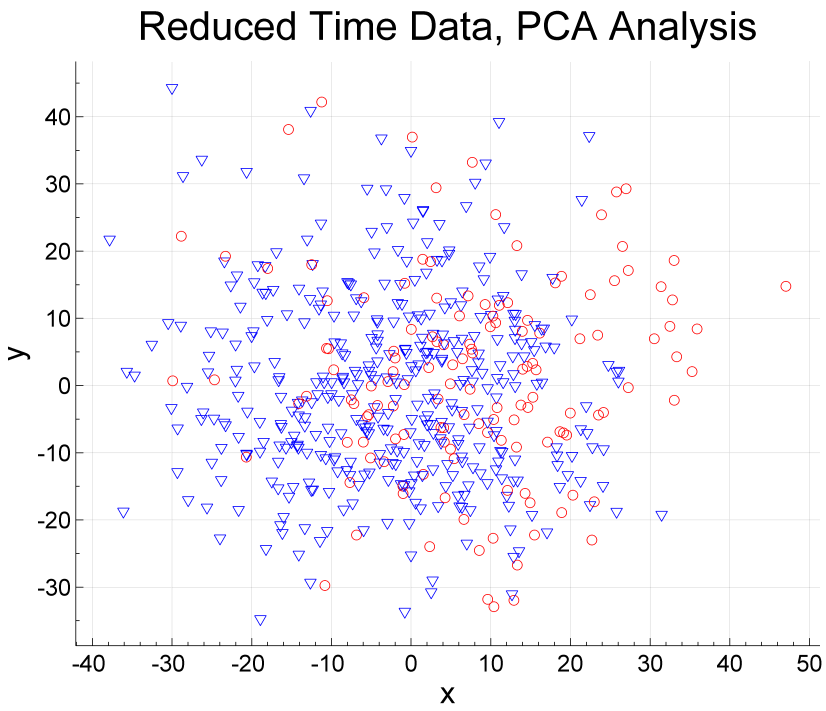

Figure 30. PCA of Child and Adult Time Domain Data, XY Plane. As seen before, this plot displays the child (red circles) and adult (blue triangles) data in the xy-plane, as functions of the strongest eigenvectors. Compared to the frequency domain data, there is very little separation between the two classes. The child data does tend more toward the positive x-direction than the adult data, indicating that some separation is possible; however, it is clear that the time domain data possesses far less distinction between classes than the frequency domain data.

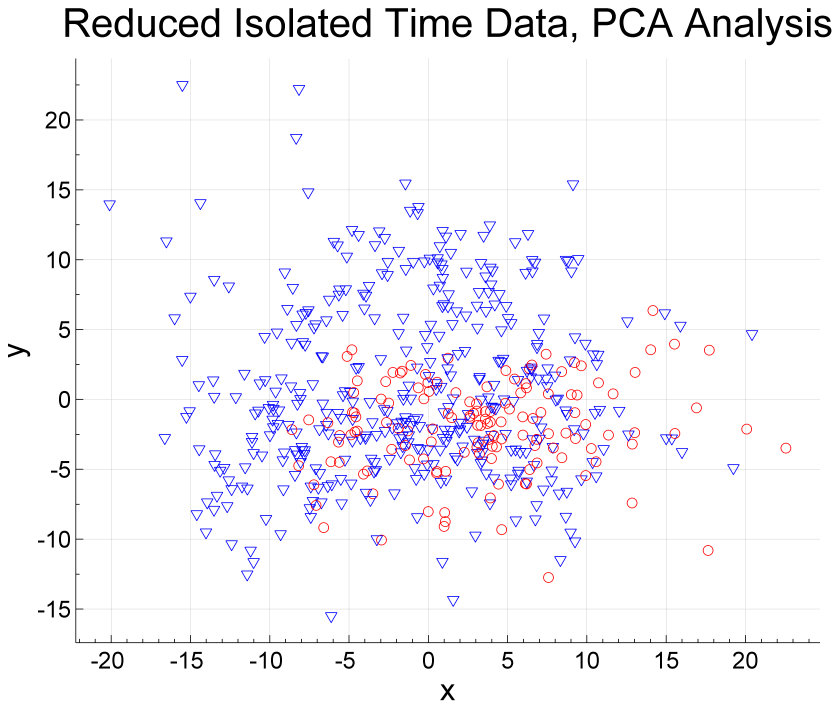

Figure 31. PCA of Child and Adult Peak-Isolated, Time Domain Data, XY Plane. Again, this plot displays the child and adult data (red circles and blue triangles, respectively) in the xy-plane, where the strongest patterns in the data are seen. This isolated data, surrounding only the target peak in the time domain, does show better separation than unprocessed time domain data, yet less separation than the frequency domain data, verifying the SVM's mid-range accuracy with this processing technique.

The strongest eigenvectors in each of the PCA investigations are associated with the covariances of the scattering data at the three frequencies nearest the high end of our frequency range: 800 MHz, 799.75 MHz, and 799.5 MHz. We interpret this finding in the following way: As the scattering at these three frequencies varies, the strongest corresponding change in scattering at other frequencies (either increasing or decreasing) is seen. This finding suggests that, at least in the megahertz range, the higher frequencies provide more information about the differences between children and adults. The result makes sense when one considers that higher frequencies allow finer resolution of the target scene. Additionally, these higher frequencies contain the shortest wavelengths — near 0.375 m. At these wavelengths, the scattering from comparatively large objects, such as adults, tends more toward optical scattering, whereas the scattering from a comparatively smaller object, such as a child, would tend more toward the resonance or Rayleigh region. This could provide an additional reason for the strongest difference between child and adult data at these frequencies. Thus, there may be an ideal range that combines optimal through-wall frequencies (where low frequencies are ideal) and frequencies that allow efficient discrimination between subjects behind a wall.

In an effort to link these results to the physical dimensions of the subjects, an investigation into possible reasons for the three adult groupings in unprocessed frequency data was done. The adult data was identified with several parameters, including gender and physical measurements, and re-plotted to determine whether the groupings were the result of these parameters. These plots are not shown, because it was evident that the groupings were not related to any individual gender or physical measurement. In fact, only once the ratios of the physical measurements are considered does a potential pattern emerges.

Both the leg-length/arm-length and leg-length/head-circumference ratios provide

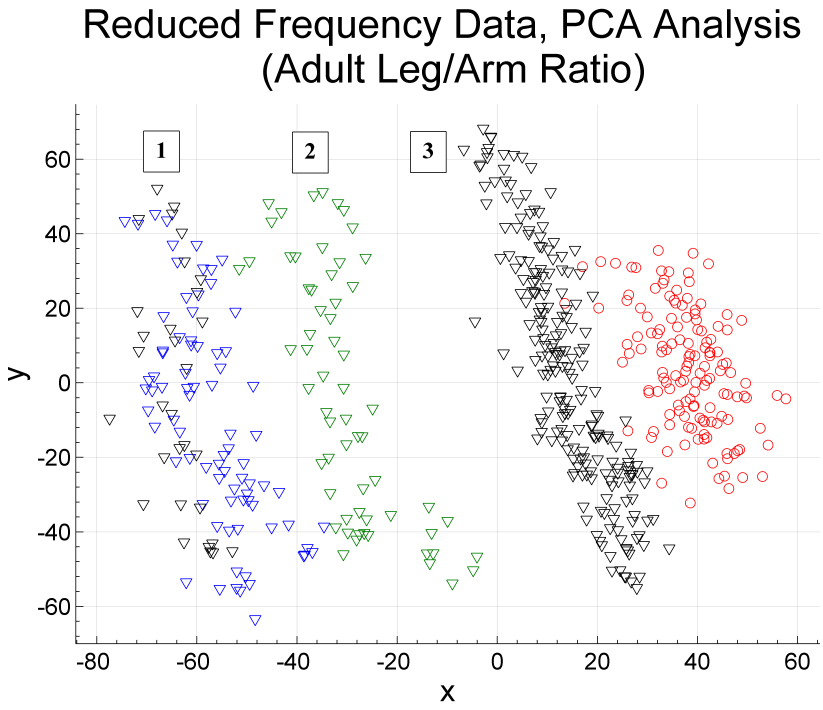

Figure 32. PCA of Child and Adult Frequency Domain Data, Leg/Arm Ratio. This plot visually demonstrates the adult groupings based on leg-length/arm-length ratio. Group 1 (blue) is a ratio of 1.22-1.30, Group 2 (green) is $>$ 1.44, and Group 3 (black) is 1.30-1.44. Note that the measurement categories do not increase linearly along the x-axis. One outlier set can be seen (black triangles in Group 1); these points come from a single subject. Rather than being due to a real phenomenon, this discrepancy may simply be the result of imprecise physical measurements. A slight adjustment of the leg and arm lengths (0.75 inches or less), places this set in the blue 1.22-1.30 category.

the data separation that corresponds best to the groupings observed in Figure 29. The leg-length/arm-length results are shown in Figure 32, color-coded and labeled according to the ratio value. Group 1 (blue) corresponds to a leg/arm ratio of 1.22-1.30, Group 2 (green) to > 1.44, and Group 3 (black) to 1.30-1.44. The first observation is that these ratios do not increase linearly with the x-axis; Groups 1 and 2 represent smaller and larger ratios, respectively, than Group 3. The second observation is that there is one set of outliers in Group 1 (misplaced black triangles). However, this discrepancy may be due more to imprecise physical measurements than an actual phenomenon. For instance, when the leg and arm lengths are adjusted by 0.75 inches (1.9 cm) or less, the ratio then falls appropriately into Group 1. The physical measurements of the subjects were made through clothing, so some amount of error exists in the measurements, and a change of 0.75 inches in either the leg or arm value is not unreasonable.

The leg/head ratio displays a similar pattern to the leg/arm ratio, and is shown in Figure 34. In this case, there are two outlying sets; however, this discrepancy may also be due to error in the physical measurements.

We expected that the measurements responsible for the primary difference in adult groupings would also be responsible for the strong difference between child and adult data. When extending the physical measurement analysis to include the child data, a strong separation in height, arm, and leg length was found between child and adult data. However, this separation, as stated before, was not enough to explain the adult groupings; therefore, one of the two ratios needed to play a role. The leg/arm length ratio, which provided the strongest groupings with minimal measurement adjustment for the adults, did *not* hold with the addition of child data (Figure 33). However, the leg/head ratio *did*. There was only one child outlier, which could be "corrected" by a small adjustment of 0.5 inches (1.2 cm) to the leg length, within possible measurement

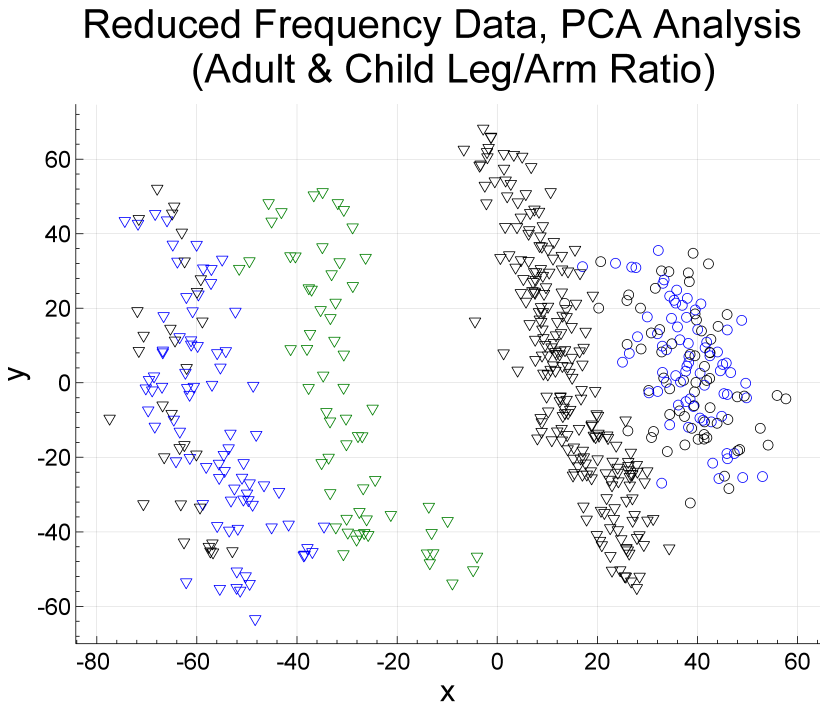

Figure 33. PCA of Child and Adult Frequency Domain Data, Leg/Arm Ratio. This plot once again demonstrates the adult groupings based on leg-length/arm-length ratio, but now the child data is included with the ratios. For the child data to hold with the leg/arm ratio, it was expected that the child group would fall within a new ratio, or possess primarily a single color of one of the adult groups. This does not occur; the child group is an even mix of the blue and black groups, indicating that the leg/arm ratio does not describe the pattern in child/adult separation.

.

error. With outlier adjustment, the leg/head ratio then results in four distinct groups, shown in Figure 34. From left to right, we have Group 1 with a ratio of 1.43–1.57, Group 2: > 1.70, Group 3: 1.57–1.70, and Group 4 which contains all child data: < 1.43. Although other physical relations may play a role, as the relationship of the leg/head ratio with the x-axis is not linear, the apparent link between the data groupings and the leg length, head circumference is consistent with the observations made by Bowden [30] in Section 3.1. He derived a successful age-based classifier based only on femur length and skull length. Our measurements are not identical, but both experiments independently indicate that the leg and skull dimensions are the primary parameters that may determine whether an individual is a child or adult, and perhaps lead to further categorization of adults. Furthermore, radar classification appears to be more sensitive to anthropometric measurement error — shifts in category were seen with errors of about 1-4 cm, compared with 4-8 cm in [30].

Table 7. Covariances of Subject Anthropometric Measurements

	Age	**Height**	**Arm Leng.**	**Leg Leng.**	**Shoulder Circ.**	**Stomach Circ.**	**Head Circ.**
Age	246.06	118.38	51.74	71.60	90.40	110.01	13.18
Height	118.38	92.05	39.40	53.28	76.71	80.66	11.55
Arm Leng.	51.74	39.40	17.62	22.63	32.87	34.87	4.95
Leg Leng.	71.60	53.28	22.63	32.52	43.51	44.25	6.58
Shoulder Circ.	90.40	76.71	32.87	43.51	73.04	72.69	10.92
Stomach Circ.	110.01	80.66	34.87	44.25	72.69	91.18	11.16
Head Circ.	13.18	11.55	4.95	6.58	10.92	11.16	1.73

One final analysis step was done, in order to link the Principal Component Analysis with what is observed in the frequency domain data, and understand more precisely how the frequency profile changes with age. In general, one expects that the physical dimensions of a human increase with age. This expectation was confirmed with data from a National Health Statistics Report by the Centers for Disease Control and Prevention (CDC), titled *Anthropometric Reference Data for Children and*

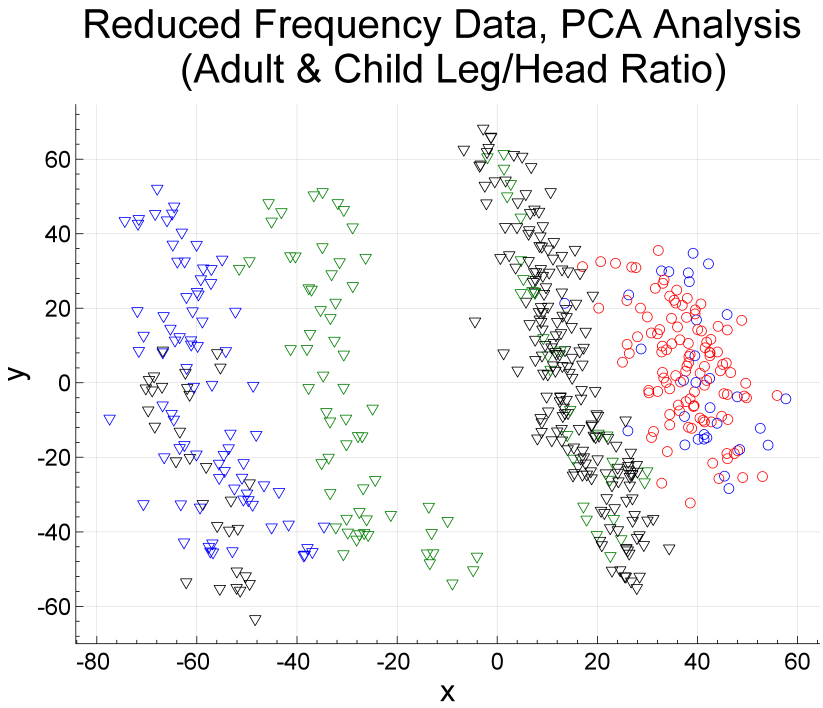

Figure 34. PCA of Child and Adult Frequency Domain Data, Leg/Head Ratio. This plot visually demonstrates the adult groupings based on leg-length/head-circumference ratio. From left to right, Group 1 (blue) is a ratio of 1.43-1.57, Group 2 (green) is $>$ 1.70, Group 3 (black) is 1.57-1.70, and the final child group, Group 4, is $<$ 1.43. Note that the measurement categories do not increase linearly along the x-axis. Two adult outlier sets can be seen (black triangles in Group 1, and green triangles in Group 3). Rather than being due to a real phenomenon, this discrepancy may simply be the result of imprecise physical measurements. An adjustment of the leg length (2 inches or less) and head circumference (0.75 inches or less), places these sets within the proper categories. Likewise an adjustment of 0.5 inches to the leg length of the single child outlier (blue circles in Group 4) corrects the ratio.

.

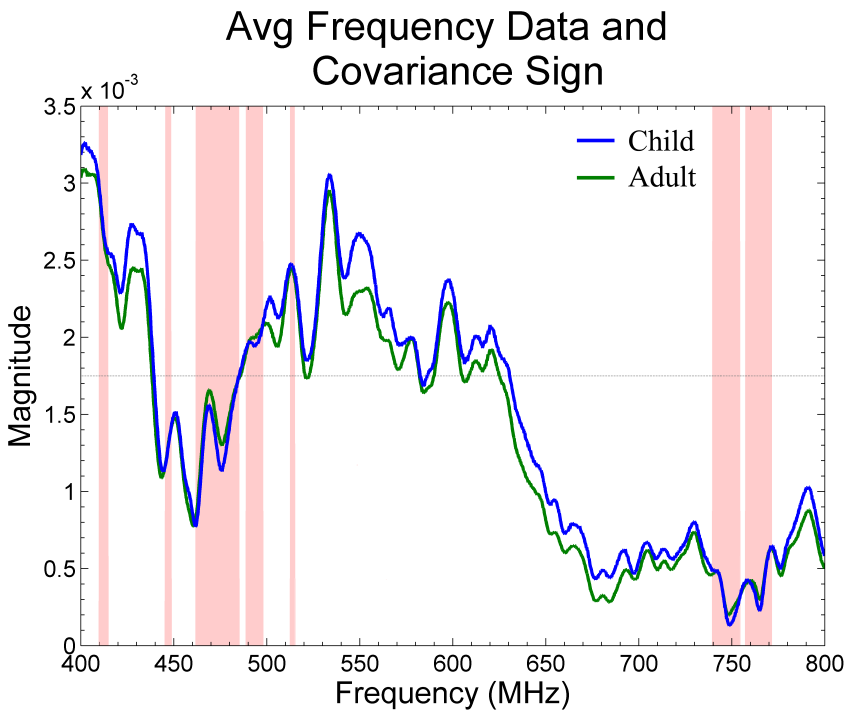

Figure 35. Averaged Child and Adult Frequency Domain Data with Covariance Sign. This plot is similar to the frequency profiles shown previously, except the intensity values are not scaled logarithmically, in order to more easily visualize the true relation between child and adult data. The pale red bars indicate frequency spans where the data shows a positive covariance between age and frequency (higher adult values). All other frequencies show a negative covariance.

Adults: United States, 2003-2006 [33]. This report contained a number of average and percentile physical measurements for several age groups. A covariance matrix was calculated for the average measurements, shown in Appendix C, which resulted in a positive definite matrix — without exception, all measurements had a positive correlation with age. This behavior was reproduced with the physical measurement data obtained from the subjects participating in our radar experiment. The covariances for the test subject measurments are shown in Table 7; note that the table is symmetric. Finally, the covariance between the subjects' age, physical dimensions, and frequency was investigated.

We hypothesized that, based on the overall lower intensities of adult scattering

in the frequency domain (refer to Figure 24), adults act as a larger dielectric object, thus attenuating the signal more than would a child. From this, we expect that, as the physical dimensions (or age) of a human increase, the overall frequency amplitude will decrease. In the examination of the covariance of frequency with age, we find that there is an 83% negative correlation, and a 15% positive correlation (the remaining percentage is weak correlation). These values are very similar to those obtained for covariance of frequency with height. The age-frequency correlation direction is shown in Figure 35. This plot is similar to the frequency profiles displayed previously, but no longer on a logarithmic scale, in order to better visualize the true difference between child and adult frequency profiles. The pale red bars indicate frequency spans where a positive covariance occurs between age and frequency (where the adult profile is higher than the child profile). In some cases, due to the thickness of the lines, this is difficult to see. Uncolored frequencies show negative covariance. Overall, we see that the covariance values match well with the average frequency profiles, and that, in general, the scattering intensity decreases with age as the physical dimensions of the subjects grow. There are certain frequency spans, however, that display the opposite behavior.

To summarize this discussion, there are features in the frequency domain that, overall, possess more structure than those in the time domain. This structure is why we see a clear visual separation between the child and adult data classes with the PCA of frequency domain data, and the strongest classification accuracy from the SVM. There is comparable structure in the reduced time domain set, consisting of those points making up the subject peaks, but perhaps not the amount of structure that may allow further adult classification, as indicated in Figure 32. This structure is also most strongly associated with the highest frequencies of our chosen range, which may serve to guide future investigation. Additionally, the structure in the frequency

domain appears to be primarily the result of a complex dependence on the leg and head dimensions of the subject. This dependence is not readily observed in the time domain, but we found the frequency domain results consistent with Bowden's findings that the leg and head dimensions are the primary indicators of age classes. Finally, there is a general negative dependence of scattering intensity in the frequency domain with age, although small regions of positive correlation do exist.

VII. Conclusions

This chapter presents the conclusions and recommendations for further work derived in the course of this thesis. The first section summarizes the work and major results, the next describes the contribution of this work, and the final section recommends topics for future study.

7.1 Summary and Conclusions

The work accomplished in this thesis builds upon prior work by Miranda, and is a part of the larger framework of the through-wall detection problem. We found, specifically, that the identification and discrimination of children or adults behind an obstructing wall and inside a building is possible using radar.

Obstructions such as walls introduces attenuation and multipath effects to radar data. To investigate the child/adult discrimination problem in a through-wall, multipath scenario, the Miranda cylinder-sphere human scattering model was expanded to incorporate multiple paths, and the effects of transmission through, and reflections from, walls and ground. Twenty-five reflection paths were identified, involving the direct paths, as well as reflected paths between the ground and an adjacent wall. All paths included two-way transmission through an obstructing wall.

In addition to the model expansion, radar scattering measurements were conducted on human volunteers in order to investigate the classification of child and adult, through-wall radar data. Classification of above 95% was reached in both the time and frequency domains, indicating that, with minimal processing, we can infer whether the subject behind a wall, in a real-world, multipath environment, is a child or adult. Isolation of points surrounding the subject provides what may be the best balance between accuracy and efficient Support Vector Machine operation.

The strong division between child and adult classes was replicated in Principal Component Analysis of the data, which strongly suggests that the features in frequency domain data possess more structure than those in time domain data, with regard to child and adult classification. Additionally, structure was found in the frequency data that appears to have a strong dependence on leg and head dimensions, and may be primarily responsible for the child/adult division, which independently verifies previous work. Up to three additional adult classes were found to depend upon these physical dimensions. Finally, the frequency domain data has a general negative dependence with age, likely due to the higher attenuation of the radar signal by larger dielectric forms (adults), although certain frequency spans do exhibit positive correlation.

7.2 Significance

While other work has provided four-path ground-only scattering models, this work expands upon the concept to provide a scattering model incorporating the effects of both the ground and an adjacent wall, for a human subject approximated as an array of dielectric cylinders and a prolate sphere. Additionally, although through-wall radar testing of humans has been accomplished before, to our knowledge this work is the first to collect radar scattering data from children and present the results. Further, there has been little work on child/adult discrimination via radar; this thesis expands upon that subject to present characteristic through-wall scattering profiles of children and adults, and demonstrates reliable classification via a Support Vector Machine. Finally, a strong structure in frequency domain data was found which separates not only children from adults, but demonstrates additional classification ability between adults. Both the separation between children and adults, and the adult groupings, appear to depend primarily upon leg and head dimensions, which is consistent with

prior work and provides an avenue for additional investigation. We now believe we can extract some measure of human physical dimensions from radar scattering data.

7.3 Future Work

Many aspects to this thesis have potential to be expanded and further investigated. In the modeling area, more complete human models exist that consist of several cylinders defining the legs and arms of the human body; a new study would be worthwhile to combine these detailed models with the multipath scattering model presented in this thesis in order to obtain a more accurate multipath, human scattering model. Futher, numerical simulations of the scattering model presented in this thesis are desired, in order to validate the model with comparison to experimental data.

Experimentally, additional through-wall human tests, on both adults and children, are required to obtain a statistically robust set of data. The thirteen adults and six children tested here are not representative of the variation in size and shape of the human body, and collections from other body types may significantly differ, affecting the classification accuracy.

Further testing should be done with an eye toward determining whether the structure seen in the Principal Component Analysis of the frequency domain data remains consistent over a wider population, and whether the basis for this structure can be refined. Another suggestion is the examination of anthropometric measurement — that is, the sensitivity of these measurements and the accuracy needed to appropriately classify child-adult groups within the radar data.

Additionally, a multiclass radar classifier based on age should be investigated, to determine the range of ages that may be correctly identified. The boundary between what defines a child and an adult, in radar data, may be narrowed from the work

presented in this thesis, to discover the range of overlap that may exist. Further, the performance of the SVM classifier may be explored in order to refine its accuracy and identify the most important frequency or time domain features required in the discrimination of child from adult, which may aid in the correlation of radar features to physical size, body-limb size ratio, or age of the subjects. More data from a larger pool of subjects will also help to determine whether the importance of the leg and head dimensions proposed here continue to hold.

Perhaps the largest advancement that future work may bring is the use of Doppler radar in child/adult identification. Many efforts in through-wall human identification center around the micro-Doppler movements performed by a human, which distinguish the person from the surrounding environment, and even other moving creatures or objects. A follow up investigation is worthwhile in determining whether these micro-Doppler characteristics may also be used to classify child data from adult data. Because of the differing body proportions of children, one can expect that their micro-Doppler signatures would be unique. Additionally, micro-Doppler is a more flexible tool, overall, for subject identification — younger subjects are less likely to remain still, as required for the work in this thesis, and subject movement adds to a more realistic environment. A movement component is almost always present that may be isolated in order to aid classification.

Finally, discrimination between multiple children and adults is the ultimate goal. The child/adult classification effort needs to be combined with the effort to distinguish between multiple people in a through-wall setting via radar. The discrimination between a person with and without a weapon, such as a firearm, is also an important goal. As resonances were seen in human data, there may be resonances associated with firearms; these resonances may be used in a through-wall problem, or at a distance, to identify the presence of such a weapon. Our results are particularly relevant to

many situations already encountered, such as school shootings and other incidents where the ability to quickly identify an armed person, from a distance and behind a wall, may save lives.

Appendix A. The Wave Equation and Scattered Field Representation

This appendix provides the background for the derivation of the scattered fields in Section 4.2. It begins with the derivation of the familiar wave equation, continues with the vector wave equation and the representation of the wave equation in spherical coordinates, then finishes with a representation of the scattered fields presented in [13].

1.1 The Wave Equation

In order to fully understand some of the upcoming mathematical derivations and notation, it is necessary to take a step back and examine the wave equation and its vector solution, particularly the solution in spherical coordinates. The derivation of the wave equation follows Tcheslavski [46], outlined in this section. It is followed, in the next section, by the derivation of the vector solution and expansion of the electromagnetic fields as given in Stratton's *Electromagnetic Theory* [35].

We first introduce the electromagnetic (EM) fields and their basic relations. The electromagnetic field is commonly associated with six quantities:

$\overline{E}$, the electric field intensity

$\overline{H}$, the magnetic field intensity

$\overline{D}$, the electric flux density

$\overline{B}$, the magnetic flux density

$\overline{J}$, the electric current density

ρ_v, the volume charge density.

In free space, the relationships between the fields are

$$\left.\begin{aligned} \overline{D} &= \epsilon_0 \overline{E} \\ \overline{B} &= \mu_0 \overline{H} \\ \overline{J} &= 0 \end{aligned}\right\} \text{ in free space} \tag{100}$$

where ϵ_0 is the permittivity of vacuum, and μ_0 is the permeability of vacuum. These values are constants, where the velocity of light $c = 1/\sqrt{\epsilon_0 \mu_0}$. In simple matter, the relations are similar:

$$\left.\begin{aligned} \overline{D} &= \epsilon \overline{E} \\ \overline{B} &= \mu \overline{H} \\ \overline{J} &= \sigma \overline{E} \end{aligned}\right\} \text{ in simple matter} \tag{101}$$

where ϵ is the absolute permittivity of the medium, μ is the absolute permeability of the medium, and σ is the medium's conductivity. The absolute permittivity is related to the vacuum permittivity through the factor ϵ_r, which is the relative permittivity: $\epsilon_r = \epsilon/\epsilon_0$. Similarly, the relative permeability of the medium is given by $\mu_r = \mu/\mu_0$. Note that, for free space or perfect dielectrics, $\sigma = 0$, and for perfect conductors, $\sigma = \infty$. [47] A lossy dielectric material will have a nonzero conductivity [46].

Armed with the fundamental EM field relations, we are now prepared to develop the wave equation. The following derivation of the wave equation is that given by Tcheslavski. We consider an environment consisting of a homogeneous media that may have possible losses ($\sigma \neq 0$). There are no free charges in the region of interest, so sources are excluded; thus, the volume charge density is zero:

$$\rho_v = 0 \tag{102}$$

Additionally, there are no external currents.

Maxwell's equations are

$$\begin{aligned} \nabla \times \overline{E} &= -\frac{\partial \overline{B}}{\partial t} & \nabla \cdot \overline{B} &= 0 \\ \nabla \times \overline{H} &= \frac{\partial \overline{D}}{\partial t} + \overline{J} & \nabla \cdot \overline{D} &= \rho_v \end{aligned} \tag{103}$$

Applying the relations in Eqs. (101) and the assumption in Eq. (102), Maxwell's equations for our environment become

$$\begin{aligned} \nabla \times \overline{E} &= -\mu \frac{\partial \overline{H}}{\partial t} & \nabla \cdot \overline{H} &= 0 \\ \nabla \times \overline{H} &= \epsilon \frac{\partial \overline{E}}{\partial t} + \sigma \overline{E} & \nabla \cdot \overline{E} &= 0 \end{aligned} \tag{104}$$

$\nabla \times \overline{E}$ and $\nabla \times \overline{H}$ are two first-order partial differential equations in terms of two dependent variables. They can be combined into one second-order PDE in terms of one variable by applying the curl to $\nabla \times \overline{E}$:

$$\nabla \times (\nabla \times \overline{E}) = -\mu \frac{\partial}{\partial t}(\nabla \times \overline{H}) \tag{105}$$

and substituting $\nabla \times \overline{H}$:

$$\nabla \times (\nabla \times \overline{E}) = -\mu \frac{\partial}{\partial t}(\epsilon \frac{\partial \overline{E}}{\partial t} + \sigma \overline{E}) = -\mu\epsilon \frac{\partial^2 \overline{E}}{\partial t^2} - \mu\sigma \frac{\partial \overline{E}}{\partial t} \tag{106}$$

We then apply the vector identity

$$\nabla \times \nabla \times \overline{E} = \nabla(\nabla \cdot \overline{E}) - \nabla^2 \overline{E} \tag{107}$$

which reduces to $-\nabla^2 \overline{E}$ because $\nabla \cdot \overline{E} = 0$, and finally obtain the wave equation

$$\nabla^2 \overline{E} - \mu\varepsilon \frac{\partial^2 \overline{E}}{\partial t^2} - \mu\sigma \frac{\partial \overline{E}}{\partial t} = 0 \tag{108}$$

The wave equation for H has the same form, and can be derived in a similar fashion, by taking the curl of $\nabla \times \overline{H}$ and substituting. Thus, all the vectors that characterize the electromagnetic field, $\overline{E}$, $\overline{B}$, $\overline{D}$, and $\overline{H}$, satisfy the same differential wave equation with the general form:

$$\nabla^2 \overline{C} - \mu\varepsilon \frac{\partial^2 \overline{C}}{\partial t^2} - \mu\sigma \frac{\partial \overline{C}}{\partial t} = 0 \tag{109}$$

The vector solution to this wave equation will be explored in the next section.

1.2 Vector Wave Equation Solution and Representation of the EM Fields

This section derives the vector solution of the wave equation, and the expansion of the electromagnetic fields, as in Stratton's *Electromagnetic Theory*. Once again, our environment consists of a closed domain, and a homogeneous, isotropic medium. Any sources of electromagnetic radiation are excluded. As in Section 1.1, the vectors in the medium that characterize an existing electromagnetic field, such as $\overline{E}$, $\overline{B}$, $\overline{D}$, and $\overline{H}$, all satisfy the same differential wave equation:

$$\nabla^2 \overline{C} - \mu\varepsilon \frac{\partial^2 \overline{C}}{\partial t^2} - \mu\sigma \frac{\partial \overline{C}}{\partial t} = 0 \tag{110}$$

where $\overline{C}$ is any one of those vectors. Time variation can be separated as a harmonic solution $e^{-i\omega t}$, and $\overline{C}$ can be assumed to contain this factor. Then, after taking the first and second derivatives of $\overline{C} = \overline{C}' e^{-i\omega t}$ and substituting, Eq. (110) becomes:

$$\nabla^2 \overline{C} + (\mu\varepsilon\omega^2 + \mu\sigma i\omega)\overline{C} = \nabla^2 \overline{C} + k^2 \overline{C} = 0 \tag{111}$$

where $k^2 = \mu\varepsilon\omega^2 + \mu\sigma i\omega$. Vector algebra gives $\nabla^2 \overline{C} = \nabla(\nabla \cdot \overline{C}) - \nabla \times \nabla \times \overline{C}$ [35], so substituting this identity into Eq. (111), we get:

$$\nabla(\nabla \cdot \overline{C}) - \nabla \times \nabla \times \overline{C} + k^2 \overline{C} = 0 \tag{112}$$

which is the vector wave equation.

When $\overline{C}$ is resolved into rectangular components (x, y, z), then (111) or (112) can be broken into three independent scalar equations, the familiar $\nabla^2 C_i + k^2 C_i = 0$, where i denotes any one of the three coordinates. However, we are interested in independent *vector* solutions of (112).

To obtain the vector solutions, first assume Ψ is a scalar function, and a solution to:

$$\nabla^2 \Psi + k^2 \Psi = 0 \tag{113}$$

and $\overline{a}$ is any constant unit vector. Three independent vector solutions of (112) can now be constructed:

$$\overline{L} = \nabla \Psi, \qquad \overline{M} = \nabla \times \overline{a} \Psi, \qquad \overline{N} = \frac{1}{k} \nabla \times \overline{M} \tag{114}$$

$\overline{L}$, $\overline{M}$, or $\overline{N}$ can replace $\overline{C}$ in (112) to satisfy it, as long as condition (113) is met. Additionally, because $\overline{a}$ is a constant vector of unit length,

$$\overline{M} = \nabla \times \overline{a} \Psi = \nabla \Psi \times \overline{a} = \overline{L} \times \overline{a} = \frac{1}{k} \nabla \times \overline{N} \tag{115}$$

and, for a consistent Ψ, $\overline{L}$ is perpendicular to $\overline{M}$, so

$$\overline{L} \cdot \overline{M} = 0 \tag{116}$$

Some additional properties are:

$$\nabla \times \overline{L} = 0, \qquad \nabla \cdot \overline{L} = \nabla^2 \Psi = -k^2 \Psi \tag{117}$$

$$\nabla \cdot \overline{M} = 0, \qquad \nabla \cdot \overline{N} = 0 \tag{118}$$

Any single solution or characteristic function Ψ_n of (113) is associated with three vector solutions, $\overline{L}_n$, $\overline{M}_n$, $\overline{N}_n$, which are not colinear. Thus, any arbitrary wave function can be represented as a linear combination of these characteristic vector functions, with coefficients of expansion to be determined.

With the definitions of $\overline{L}_n$, $\overline{M}_n$, and $\overline{N}_n$ established, we can now move on to a representation of the electric and magnetic field vectors $\overline{E}$ and $\overline{H}$ in terms of the characteristic vector functions. Keeping in mind the time factor $e^{-i\omega t}$ implicitly contained inside each vector, and assuming a homogeneous, isotropic medium of conductivity σ and free-charge density $\rho = 0$, we begin with:

$$\overline{E} = \frac{i\omega\mu}{k^2}\nabla \times \overline{H}, \qquad \overline{H} = \frac{1}{i\omega\mu}\nabla \times \overline{E} \tag{119}$$

Because each is proportional to the curl of the other, $\overline{M}$ and $\overline{N}$ are appropriate to represent the fields $\overline{E}$ and $\overline{H}$. The vector potential $\overline{A}$, where $\overline{H} = \frac{1}{\mu}\nabla \times \overline{A}$, can then be represented by an expansion in the characteristic vector functions:

$$\overline{A} = \frac{i}{\omega}\sum_n (a_n\overline{M}_n + b_n\overline{N}_n + c_n\overline{L}_n) \tag{120}$$

where a_n, b_n, and c_n are the coefficients of expansion, which depend upon the current distribution. $\overline{H}$ can now be found by the relation between $\overline{H}$ and $\overline{A}$:

$$\overline{H} = \frac{1}{\mu}\nabla \times \overline{A} = \frac{-1}{i\omega\mu}\sum_n (a_n\nabla \times \overline{M}_n + b_n\nabla \times \overline{N}_n + c_n\nabla \times \overline{L}_n) \tag{121}$$

Finally, from the relations between $\overline{M}$ and $\overline{N}$ in (114) and (115), and because the curl of $\overline{L}$ is zero:

$$\overline{H} = \frac{-k}{i\omega\mu}\sum_n (a_n\overline{N}_n + b_n\overline{M}_n) \tag{122}$$

From (119), a similar procedure results in the expression for $\overline{E}$:

$$\overline{E} = -\sum_n (a_n \overline{M}_n + b_n \overline{N}_n) \tag{123}$$

It is these expansions (122) and (123) for $\overline{H}$ and $\overline{E}$ that will become important later in the paper.

1.3 Wave Equation in Spherical Coordinates

Another important equation to understand is the scalar wave equation treated in spherical coordinates, as this will be another piece used in upcoming derivations. This section explores the derivation of the spherical wave equation, again as given in [35].

A wave can be represented as $\Psi = f(R, \theta, \phi)e^{-i\omega t}$, and, in a homogeneous, isotropic medium, $f(R, \theta, \phi)$ must satisfy

$$\nabla^2 f + k^2 f = 0 \tag{124}$$

Expanding $\nabla^2 f$ in spherical coordinates, this equation becomes

$$\frac{1}{R^2}\frac{\partial}{\partial R}\left(R^2 \frac{\partial f}{\partial R}\right) + \frac{1}{R^2 \sin\theta}\frac{\partial}{\partial \theta}\left(\sin\theta \frac{\partial f}{\partial \theta}\right) + \frac{1}{R^2 \sin^2\theta}\frac{\partial^2 f}{\partial \phi^2} + k^2 f = 0 \tag{125}$$

Separation of variables can be applied, giving $f = f_r(R) f_\theta(\theta) f_\phi(\phi)$ and a set of three equations:

$$R^2 \frac{\mathrm{d}^2 f_r}{\mathrm{d}R^2} + 2R\frac{\mathrm{d}f_r}{\mathrm{d}R} + (k^2 R^2 - p^2) f_r = 0 \tag{126}$$

$$\frac{1}{\sin\theta}\frac{\mathrm{d}}{\mathrm{d}\theta}\left(\sin\theta \frac{\mathrm{d}f_\theta}{\mathrm{d}\theta}\right) + \left(p^2 - \frac{q^2}{\sin^2\theta}\right) f_\theta = 0 \tag{127}$$

$$\frac{\mathrm{d}^2 f_\phi}{\mathrm{d}\phi^2} + q^2 f_\phi = 0 \tag{128}$$

where p and q are separation constants.

For a medium whose properties are independent of ϕ, f_ϕ must be periodic with period 2π, and q then equals $m = 0, \pm 1, \pm 2, \ldots$. To determine p, (127) must be re-written as the Legendre equation; the solution f_θ will then be identified as the associated Legendre polynomials. To re-write the equation, we first substitute $\cos\theta$ for η in (127). After some work, this gives

$$(1-\eta^2)\frac{\mathrm{d}^2 f_\theta}{\mathrm{d}\eta^2} - 2\eta\frac{\mathrm{d}f_\theta}{\mathrm{d}\eta} + \left(p^2 - \frac{m^2}{1-\eta^2}\right) f_\theta = 0 \tag{129}$$

where $\eta \neq \pm 1, \infty$. If $m = 0$, and we choose $p^2 = n(n+1)$ for $n = 0, 1, 2, \ldots$, then equation (129) becomes

$$(1-\eta^2)\frac{\mathrm{d}^2 f_\theta}{\mathrm{d}\eta^2} - 2\eta\frac{\mathrm{d}f_\theta}{\mathrm{d}\eta} + n\,(n+1)\, f_\theta = 0 \tag{130}$$

This is the Legendre equation for $p^2 = n(n+1)$. The polynomial solutions satisfying this converge and are the Legendre polynomials $P_n(\eta)$. In differentiating this equation m times, we recover (129) as

$$(1-\eta^2)\frac{\mathrm{d}^2 f_\theta}{\mathrm{d}\eta^2} - 2\eta\frac{\mathrm{d}f_\theta}{\mathrm{d}\eta} + \left[n(n+1) - \frac{m^2}{1-\eta^2}\right] f_\theta = 0 \tag{131}$$

The solutions of this equation must be finite at $\eta = \pm 1$ and periodic in θ; these are now seen to be the associated Legendre polynomials:

$$f_\theta(\eta) = P_n^m(\eta) = (1-\eta^2)^{\frac{m}{2}} \frac{\mathrm{d}^m P_n(\eta)}{\mathrm{d}\eta^m} \tag{132}$$

The above definition holds only if n and m are positive integers. To maintain a positive n and m, the particular solutions of (128) are chosen to be $\cos m\phi$ and $\sin m\phi$, and m, n are restricted to $0, 1, 2, \ldots$. $P_n^m(\eta)$ denotes an nth degree polynomial, $P_n(\eta)$,

derived m times, so it vanishes when $m > n$. Because of this, $P_n^m(\eta)$ becomes

$$P_n^m(\eta) = \frac{(1-\eta^2)^{\frac{m}{2}}}{2^n \eta!} \frac{\mathrm{d}^{n+m}(\eta^2-1)^n}{\mathrm{d}\eta^{n+m}} \tag{133}$$

Now, the functions $\cos m\phi P_n^m(\cos\theta)$ and $\sin m\phi P_n^m(\cos\theta)$ (for $\eta = \cos\theta$) are periodic on the surface of a unit sphere, with the indices m and n determining the number of nodal lines. A linear combination of these functions forms the spherical surface harmonics of degree n:

$$Y_n(\theta,\phi) = \sum_{m=0}^{n} (a_{nm}\cos m\phi + b_{nm}\sin m\phi) P_n^m(\cos\theta) \tag{134}$$

The functions f_θ and f_ϕ have now been determined. Their combined form is (134) with (133). It now remains to specify f_r. If we let $f_r = \frac{1}{\sqrt{kR}} v(R)$, then $v(R)$ satisfies

$$R^2 \frac{\mathrm{d}^2 v}{\mathrm{d}R^2} + R\frac{\mathrm{d}v}{\mathrm{d}R} + \left[k^2R^2 - \left(n+\frac{1}{2}\right)^2\right] v = 0 \tag{135}$$

and is a cylinder function of half order:

$$f_r(R) = \frac{1}{\sqrt{kR}} Z_{n+\frac{1}{2}}(kR) \tag{136}$$

The cylinder function of $Z_{n+\frac{1}{2}}(kR)$ is chosen to be a Bessel function of the first kind inside domains that include the origin, and a Bessel function of the third kind wherever the field is to be represented as a traveling wave.

Bessel functions of the first kind are given by

$$J_n(\rho) = \sum_{m=0}^{\infty} \frac{(-1)^m}{m!(n+m)!} \left(\frac{\rho}{2}\right)^{n+2m} \tag{137}$$

for $n = 0, 1, 2, \ldots$, and $J_n(\rho)$ is a single-valued function of position. Bessel functions

of the third kind (Hankel functions) are associated with traveling waves, and are given by

$$H_n^{(1)}(\rho) = J_n(\rho) + iN_n(\rho) \tag{138}$$

$$H_n^{(2)}(\rho) = J_n(\rho) - iN_n(\rho) \tag{139}$$

where

$$N_n(\rho) = \frac{1}{\sin n\pi}[J_n(\rho)\cos n\pi - J_{-n}(\rho)] \tag{140}$$

which is a Bessel function of the second kind, and $J_{-n}(\rho) = (-1)^n J_n(\rho)$.

Spherical Bessel functions are additionally denoted by the general representation

$$z_n(\rho) = \sqrt{\frac{\pi}{2\rho}} Z_{n+\frac{1}{2}}(\rho) \tag{141}$$

where z_n may be replaced by j_n, n_n, h_n, and $Z_{n+\frac{1}{2}}$ by the corresponding $J_{n+\frac{1}{2}}$, $N_{n+\frac{1}{2}}$, or $H_{n+\frac{1}{2}}$. More specifically,

$$j_n(\rho) = 2^n \rho^n \sum_{m=0}^{\infty} \frac{(-1)^m (n+m)!}{m!(2n+2m+1)!} \rho^{2m} \tag{142}$$

$$n_n(\rho) = -\frac{1}{2^n \rho^{n+1}} \sum_{m=0}^{\infty} \frac{\Gamma(2n-2m+1)!}{m!\Gamma(n-m+1)!} \rho^{2m} \tag{143}$$

Finally, with the knowledge of f_r, f_θ, and f_ϕ, the full representation of $f(R,\theta,\phi)$ as a sum of elementary spherical wave functions is

$$f(R,\theta,\phi) = \sum_{n=0}^{\infty} z_n(kR) \left[a_{n0} P_n(\cos\theta) + \sum_{m=1}^{n} (a_{nm}\cos m\phi + b_{nm}\sin m\phi) P_n^m(\cos\theta) \right] \tag{144}$$

Case 1, f is finite at the origin, and z_n is a spherical Bessel function of the first kind:

$$z_n(kR) \to j_n(kR) \tag{145}$$

Case 2, f describes a field whose surfaces of constant phase travel *outward*, and involves a spherical Bessel function of the third kind:

$$z_n(kR) \rightarrow h_n^{(1)}(kR) = j_n(kR) + in_n(kR) \tag{146}$$

Note that, in Yeh [13] and Stratton [35], which the work in this thesis follows, the expression for $f(R, \theta, \phi)$ is also presented as

$$f_{\substack{e \\ o}mn} = \begin{matrix}\sin \\ \cos\end{matrix}(m\theta) P_n^m(\cos\theta) z_n(kR) \tag{147}$$

where the notation $\begin{matrix}e \\ o\end{matrix}$ denotes the even or odd form of the function. This is the form more useful for coding applications.

1.4 Scattered Fields: A Simple Representation

Before beginning to build the mathematical model of the scattered electromagnetic fields from an object representing a human, it is worthwhile to first take a look at a simple representation of the problem, followed by the derivation of the mathematical representation of the associated scattered fields. In this section, a representation of the problem will be developed, following the method outlined in [13].

The problem consists of an arbitrary dielectric object, with permeability μ and permittivity ϵ, radiated by an electromagnetic wave. This incident wave is denoted by $\overline{E}^i$, and the surrounding medium is assumed to be free space with permeability and permittivity μ_0 and ϵ_0, respectively. This situation is depicted in Figure 36, along with the spherical coordinate system. The goal is to determine the scattered field at all points P on an imaginary sphere surrounding the object.

This problem can be illustrated schematically as in Figure 37. The sum of the incident and scattered fields (denoted by the superscripts i and s, respectively) gives

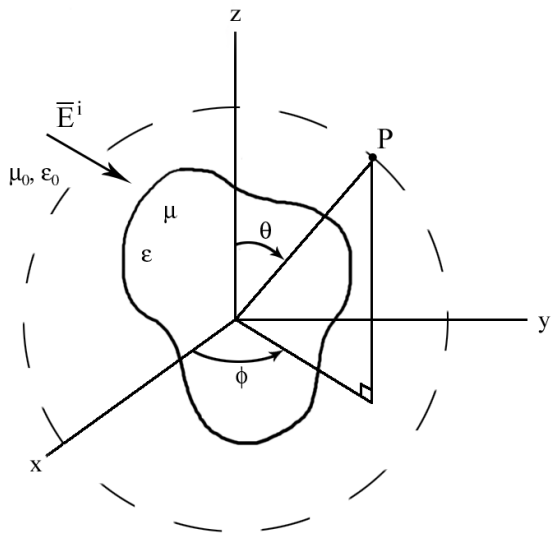

Figure 36. Initial problem representation (reproduced from [13]). A plane electromagnetic wave is incident upon an arbitrary dielectric object, which is homogeneous and isotropic. The object has permeability μ and permittivity ϵ, while the respective parameters in the surrounding free space are μ_0 and ϵ_0. P represents one point on a sphere surrounding the object.

the total fields:

$$\overline{E}_{tot} = \overline{E}^i + \overline{E}^s, \qquad \overline{H}_{tot} = \overline{H}^i + \overline{H}^s \tag{148}$$

This is the full representation of the problem and the one that will be recovered through the process of developing additional representations that *separate* the sources of the fields (incident and scattered) and then *recombine* them. Ultimately, we will find the scattered field in terms of the incident field and the object's properties, through the following process:

Incident fields ⇒ Internal fields ⇒ Surface currents ⇒ Scattered fields.

First, a representation of the scattered field is developed (Figure 38, left side). The scattered field, $\overline{E}^s$ and $\overline{H}^s$, can be thought of as the field produced by internal polarization currents. $\overline{J}$ and $\overline{M}$ are introduced as these polarization currents, the direct sources of the scattered field, which were induced by the incident field. Schelkunoff's equivalence theorem can now be applied to this representation. This theorem states

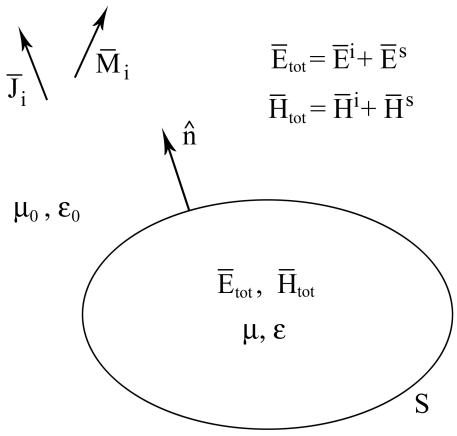

Figure 37. The scattering problem (reproduced from [13]). The object is depicted by the surface S with normal unit vector $\hat{n}$. The total fields $\overline{E}_{tot}$ and $\overline{H}_{tot}$ are made up of the incident and scattered fields. $\overline{J}_i$ and $\overline{M}_i$ are the sources of the incident field. The parameters of the scattering object and the surrounding free space are μ, ϵ and μ_0, ϵ_0, respectively.

that the field in a source-free region bounded by a surface S can be produced by electric and magnetic currents on this surface. So, following this reasoning, with the area outside S said to be bounded by S (so that there are no sources in this area), the polarization currents are replaced by equivalent surface currents with boundary conditions that indicate a null field is radiated inside S, and the scattered field is radiated external to S (Figure 38, right side). The source of the scattered field is now this set of surface currents:

$$\overline{J}_s = \hat{n} \times \overline{H}^s, \qquad \overline{M}_s = \overline{E}^s \times \hat{n} \tag{149}$$

where $\overline{J}_s$ is the electric current sheet, and $\overline{M}_s$ is the magnetic current sheet; $\hat{n}$ points into the source-free region.

Next, a second set of fields is developed, with the end goal of combining the representations with the incident field to result in zero field inside S. In order to do this, we need a field $-\overline{E}^i$ and $-\overline{H}^i$ produced by $-\overline{J}_i$ and $-\overline{M}_i$ (the negative of the

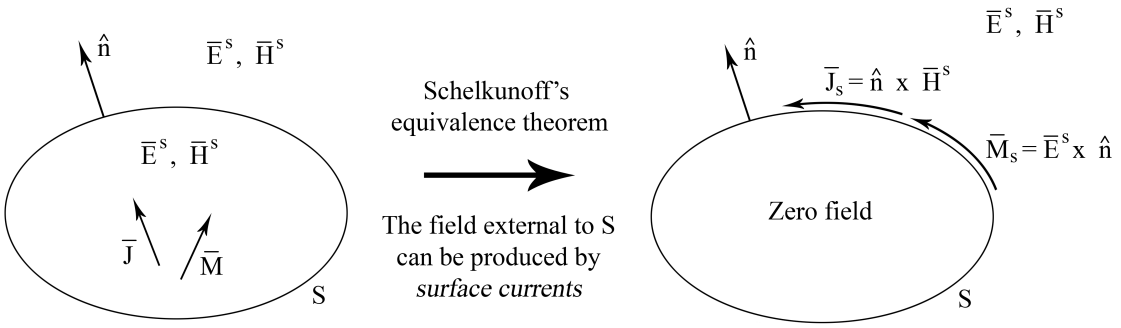

Figure 38. Scattered Fields (reproduced from [13]). The left side depicts an initial representation of the scattered fields $\overline{E}^s$ and $\overline{H}^s$, produced by internal polarization currents $\overline{J}$ and $\overline{M}$, which were induced by the incident field. Schelkunoff's equivalence theorem is then applied, replacing the polarization currents with surface currents $\overline{J}_s$ and $\overline{M}_s$, which then radiate the scattered field outside S, and zero field inside (right).

incident field). This is depicted in Figure 39, left side. The normal $\hat{n}_2$ points into the source-free area, now inside S. Schelkunoff's equivalence theorem is again applied, replacing $-\overline{J}_i$ and $-\overline{M}_i$ by the surface currents

$$\overline{J}_i = \hat{n}_2 \times (-\overline{H}^i), \qquad \overline{M}_i = (-\overline{E}^i) \times \hat{n} \tag{150}$$

which radiate the fields $-\overline{E}^i$ and $-\overline{H}^i$ inside S, and a null field outside.

Finally, the representations of these individual fields are combined. Superposition of the scattered and negative fields and sources gives the situation depicted in the left side of (Figure 40), a temporary step. This gives a set of surface currents

$$\overline{J}_+ = \overline{J}_i + \overline{J}_s = \hat{n} \times (\overline{H}^i + \overline{H}^s) = \hat{n} \times \overline{H}_+ \tag{151}$$

$$\overline{M}_+ = \overline{M}_i + \overline{M}_s = \hat{n} \times (\overline{E}^i + \overline{E}^s) = \hat{n} \times \overline{E}_+ \tag{152}$$

that radiate the scattered field outside S, as well as the negative of the incident field inside. However, a null field within S is required. If the incident sources and fields are now added (Figure 40, right side), the null field within S is obtained, and the

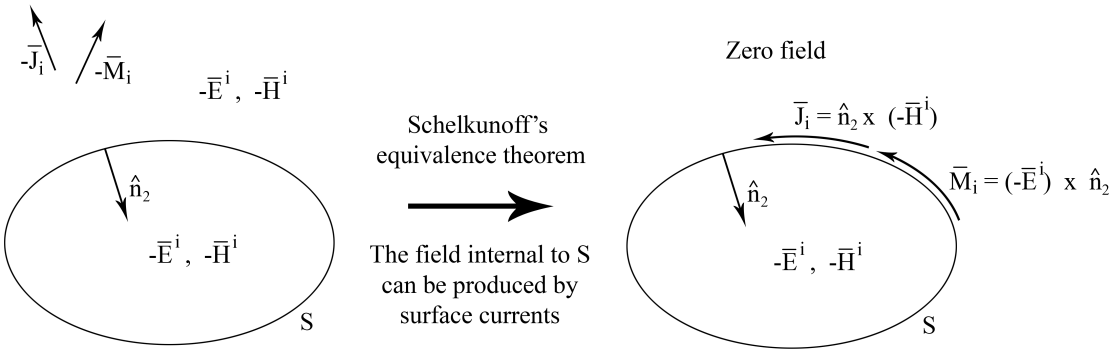

Figure 39. Negative Fields (reproduced from [13]). The negative of the incident field, $\overline{J}_i$ and $\overline{M}_i$, produces $-\overline{E}^i$ and $-\overline{H}^i$ (left). Notice that the normal $\hat{n}_2$ now points internal to S. The equivalence theorem is again applied, replacing the sources by surface currents $\overline{J}_i$ and $\overline{M}_i$ (right). These currents radiate the negative of the incident field inside S, and zero field outside.

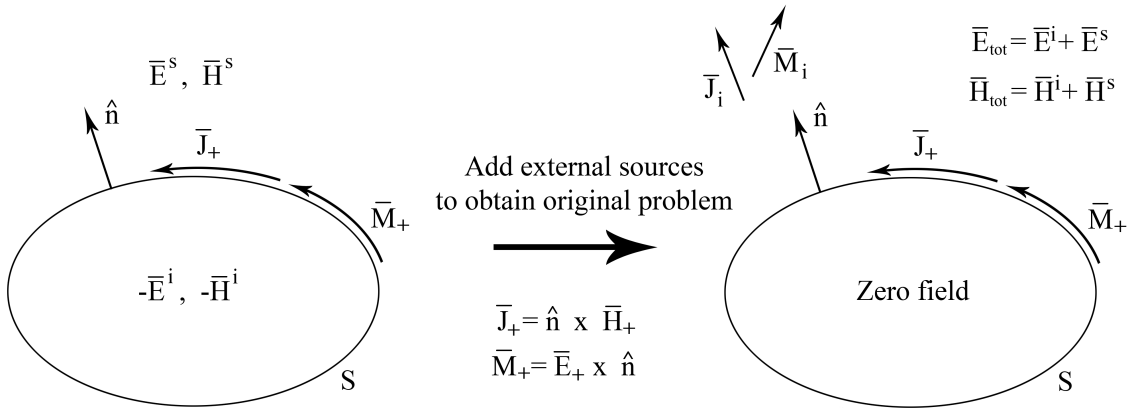

Figure 40. Combined Fields (reproduced from [13]). The scattered and negative fields from the right sides of Figs. 38 and 39 are combined (left). This gives the scattered field external to S, and the negative of incident field internal to S, as well as the sum of the surface currents, $\overline{J}_+$ and $\overline{M}_+$. The original sources and incident field are then added (right). Fields inside S sum to zero, resulting in a null field, and fields outside S give $\overline{E}_{tot}$ and $\overline{H}_{tot}$, the sum of the incident and scattered fields, which recovers those in the original scattering problem.

original problem representation is recovered. Outside S, the sources and fields are identical to those in the original problem, and the scattering object has been replaced by a set of surface currents over a surface, which radiate the scattered field outside S, and the negative of the incident field inside.

Appendix B. Support Vectors and Pattern Recognition

This appendix provides background information on the concept of the Support Vector Machine, the classification tool used in this paper to distinguish child and adult radar data. A Support Vector Machine (SVM) accepts data as an input and returns the classification as the output, through the examination of similarities, or patterns, in the data. Figure 41 displays the concept of a Support Vector Machine. Before the SVM can be described in detail, it is necessary to provide a basic background on pattern recognition and how data is represented. The following subsections describe the representation of data and its transformation into a form that can be classified via pattern recognition, and then relates pattern recognition to Support Vector Machines. The following derivation and terminology is described in Scholkopf's and Smola's *Learning with Kernels* [48].

2.1 Data Representation

We begin with a set of data that can be divided into two categories or classes - a binary classification, which is what we are interested in. The data points are given as the observations $x_1, \ldots, x_m$, from domain χ, and the two classes are represented simply by $+1$ or -1, as a convenience. These designations could, for example, represent the child and adult classes. We form an ordered pair of the data and its classification designation by (x_i, y_i), where x_i is a single observation from the data, and $y_i \in \{\pm 1\}$ is the classification output, which can take on only one of the two values. This is the training data, whose classification is already known. [48]

We now have a new data point x that needs to be assigned to one of the two classes. In other words, we need to predict the corresponding $y \in \{\pm 1\}$ such that (x, y) is similar in some way to the training data. We need a similarity measure. [48]

The similarity measure is represented by a function $k(x, x')$, which returns a real

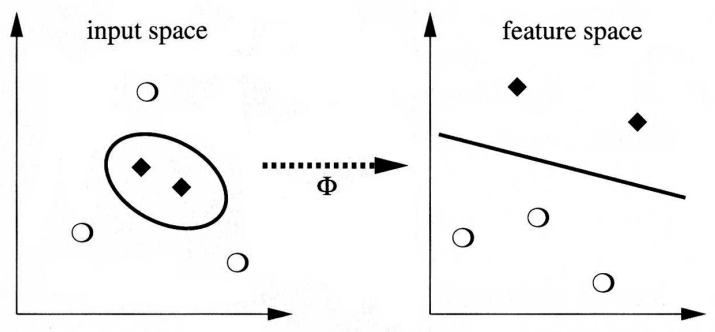

Figure 41. SVM Concept (reproduced from [48]). Data is mapped from the input space into a higher-dimensional feature space H by Φ. Whereas the separation between the data may be very complicated and not obvious in the original input space, the mapping allows the data to be more readily classified in the feature space, and a dividing hyperplane with a maximum margin can be constructed. A kernel function $k(x, x')$ allows the hyperplane to be calculated without explicitly mapping each point.

number characterizing the similarity of the observations x and x'. The function k is symmetric for this classifier: $k(x, x') = k(x', x)$, and is called a *kernel*. [48]

In order to better illustrate a similarity measure, we consider the dot product:

$$\bar{x} \cdot \bar{x}' = \langle \bar{x}, \bar{x}' \rangle = \sum_{i=1}^{N} x_i x_i' \tag{153}$$

where i denotes the ith component of vector $\bar{x}$. Equation (153) is a very simple type of similarity measure. The dot product is related to the cosine of the angle between vectors $\bar{x}$ and $\bar{x}'$:

$$\langle \bar{x}, \bar{x}' \rangle = \|\bar{x}\| \, \|\bar{x}'\| \cos\theta \tag{154}$$

and to the length, or norm, of the vector:

$$\|\bar{x}\| = \sqrt{\langle \bar{x}, \bar{x} \rangle} \tag{155}$$

Thus, the dot product can be used as a tool to provide some sense of the similarity between two vectors, in terms of angles and distances. [48]

Now, the data or observations themselves may or may not already exist in dot product space. To use the dot product as a similarity measure, we need to represent the observations as vectors in dot product space. In other words, we need to map the observations to this space. If the dot product space is represented as H and our mapping function is Φ, then this mapping can be represented in mathematical notation as [48]

$$\begin{aligned} \Phi : \chi &\to H \\ x &\mapsto \bar{x} := \Phi(x) \end{aligned} \tag{156}$$

The first line describes the function. It says that Φ is a function that accepts variables from the domain χ and returns values in the domain H. The second line describes what happens to the input data x. It says that x maps to the vector $\bar{x}$ through the function $\Phi(x)$.

The dot product space H is the feature space through which the patterns or features in the data are studied. The similarity measure of our dot product is now

$$k(x, x') = \langle \bar{x}, \bar{x}' \rangle = \langle \Phi(x), \Phi(x') \rangle \tag{157}$$

Through this relation, we can find either a kernel k to represent a certain feature space, or we can identify a feature space to represent a kernel [45]. Now that we can use the dot product on the data, patterns in the data can be dealt with geometrically. We can also choose any mapping Φ that is most suitable for a given problem. [48]

A few common kernel examples for $x \in \mathbb{R}^n$ are [45]:

- $k(x, x') = \langle x, x' \rangle^d$, as in Equation (157), corresponding to the feature vector $\Phi(x)$ of all dth degree monomials of the components of x.
- $k(x, x') = (\langle x, x' \rangle + 1)^d$, corresponding to the feature vector $\Phi(x)$ of all dth degree and lower monomials of the components of x.

- $k(x, x') = e^{-\|x-x'\|^2/(2\sigma^2)}$, a Gaussian radial basis function; $\Phi(x)$ is complicated, but not required to know.

2.2 Binary Classification Example

As a simple example pattern recognition algorithm to illustrate the concept, we consider the problem of classifying a new data point into an existing binary classification scheme. The approach of our simple classification method is to place the new point into the class with the mean closest to the point. The data is already assumed to be mapped into a dot product space in three dimensions H^3. The new data point, whose classification is unknown, is represented by $\bar{x}$; existing data points, whose classifications are known, are given by $\bar{x}_1, \ldots, \bar{x}_m$. [48]

Again, the two classes are designated by ± 1. The means of the classes are

$$\bar{c}_+ = \frac{1}{m_+} \sum_{\{1|y_i=+1\}} \bar{x}_i \tag{158}$$

$$\bar{c}_- = \frac{1}{m_-} \sum_{\{1|y_i=-1\}} \bar{x}_i \tag{159}$$

where m_+ and m_- are the number of observations with $+1$ or -1 classification, respectively, and $m_+, m_- > 0$. The new data point can be placed by considering the geometry of the situation, illustrated in Figure 42. The vectors $\bar{c}_+$ and $\bar{c}_-$ point to the means of their respective classes. The point halfway between the means, on the vector $\bar{w}$ connecting them, is given by vector $\bar{c}$. [48]

$$\bar{w} = \bar{c}_+ - \bar{c}_- \tag{160}$$

$$\bar{c} = (\bar{c}_+ + \bar{c}_-)/2 \tag{161}$$

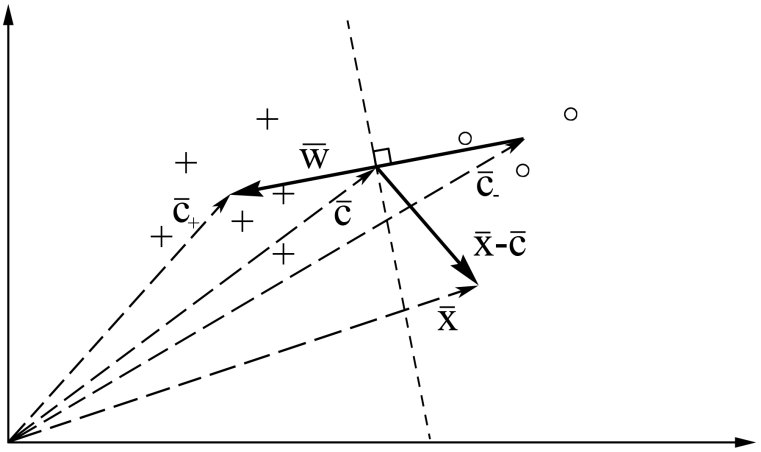

Figure 42. Simple Geometric Classification (reproduced from [48]). Data points are divided into two classifications, represented by + and ∘, which denote the +1 and -1 classifications, respectively. Vectors $\bar{c}_+$ and $\bar{c}_-$ point to their corresponding means, $\bar{w} = \bar{c}_+ - \bar{c}_-$, $\bar{c}$ points to the midpoint of $\bar{w}$, and $\bar{x}$ points toward the data point needing to be classified. The angle between $\bar{x} - \bar{c}$ and $\bar{w}$ determines the classification of $\bar{x}$, calculated via the dot product. In this particular case, the angle is greater than $\pi/2$, so the point will be classified as -1. The dotted line denotes the decision boundary; it is a hyperplane, and orthogonal to $\bar{w}$.

To determine the class of the new point $\bar{x}$, we determine whether the angle formed by $\bar{x} - \bar{c}$ and w is greater or less than $\pi/2$:

$$y = \text{sgn}\left(\langle \bar{x} - \bar{c}, \bar{w} \rangle\right) \tag{162}$$

where

$$\text{sgn}\,(x) = \begin{cases} -1 & \text{if } x < 0 \\ 0 & \text{if } x = 0 \\ 1 & \text{if } x > 0 \end{cases} \tag{163}$$

An angle less than $\pi/2$ will give a positive dot product, resulting in $y = +1$, while a greater angle will give a negative result and $y = -1$. This is our classifier. We can

expand and rewrite, incorporating (160) and (161), as

$$\begin{aligned} y &= \operatorname{sgn}\left(\left\langle \bar{x} - \frac{\bar{c}_+ + \bar{c}_-}{2}, \bar{c}_+ - \bar{c}_- \right\rangle\right) \\ &= \operatorname{sgn}\left(\langle \bar{x}, \bar{c}_+ \rangle - \langle \bar{x}, \bar{c}_- \rangle + b\right) \end{aligned} \tag{164}$$

where b is the offset

$$b = \frac{1}{2}(\|\bar{c}_-\|^2 - \|\bar{c}_+\|^2) \tag{165}$$

with the length of the vectors defined in (155). If the lengths are equal, i.e. the means have the same distance to the origin, b will be zero. Equation (164) is further expanded by incorporating (158) and (159):

$$y = \operatorname{sgn}\left(\frac{1}{m_+}\sum_{\{\imath|y_i=+1\}}\langle \bar{x}, \bar{x}_i\rangle - \frac{1}{m_-}\sum_{\{\imath|y_i=-1\}}\langle \bar{x}, \bar{x}_i\rangle + b\right) \tag{166}$$

But the dot product is the kernel $k(x, x_i)$, by Equation (157), so

$$y = \operatorname{sgn}\left(\frac{1}{m_+}\sum_{\{\imath|y_i=+1\}} k(x, x_i) - \frac{1}{m_-}\sum_{\{\imath|y_i=-1\}} k(x, x_i) + b\right) \tag{167}$$

Through a similar expansion, Equation (165) becomes

$$b = \frac{1}{2}\left(\frac{1}{m_-^2}\sum_{\{(i,j)|y_i=y_j=-1\}} k(x_i, x_j) - \frac{1}{m_+^2}\sum_{\{(i,j)|y_i=y_j=+1\}} k(x_i, x_j)\right) \tag{168}$$

In general, the classifier (167) takes the form of a kernel expansion on the input domain,

$$y = \operatorname{sgn}\left(\sum_{i=1}^{m}\alpha_i k(x, x_i) + b\right) \tag{169}$$

which corresponds to the hyperplane dividing the classes in the feature space. The coefficients α_i are then the dual representation of the hyperplane's normal vector.

This classifier is an example-based classifier because it requires classified training data with which to test unclassified points against. Unclassified points are compared to all training points. [48]

The pattern recognition classifier in the example above is a very simple type of classifier. More complicated classifiers can differ in the patterns upon which the kernels are centered, and the weights α_i ($1/m_+$ and $1/m_-$ in the given example). In essense, we obtain a general linear combination of training patterns. We can further choose to remove the influence of patterns that are far from the decision boundary, in order to simplify the computation. In this case, the hyperplane will depend on a subset of training points that are called Support Vectors. [48]

2.3 Hyperplanes and Support Vectors

The remainder of this section will introduce the optimization problems used to determine dividing hyperplanes for data sets with good separation between classes, and those with poor separation. We will also expand upon the concept of Support Vectors.

Let $f(\bar{x})$ be a predicition of the true classification value $y \in \{\pm 1\}$. From Equation (164) and the definition of $\bar{w}$ in Equation (160), we can restate the decision function y as its prediction

$$f(\bar{x}) = \operatorname{sgn}\left(\langle \bar{w}, \bar{x} \rangle + b\right) \tag{170}$$

We know this takes on the value ± 1 or 0. A value of ± 1 means that a point $\bar{x}$ gets classified and is placed on either side of the dividing hyperplane. A value of 0 means that the point is placed on the hyperplane itself; thus, the hyperplane is designated by all points such that

$$\langle \bar{w}, \bar{x} \rangle + b = 0 \tag{171}$$

where $\bar{w} \in H$, $b \in \mathbb{R}$. The optimal hyperplane has the maximum margin of separation between the training points and the hyperplane. In other words, we want to find the minimum distance between each training point $\bar{x}_i$ and a point on the hyperplane (a perpendicular line in three-dimensional space), and maximize this collection of distances. In mathematical notation, this optimal hyperplane is the solution of [48]

$$\text{maximize } \min \{\|\bar{x} - \bar{x}_i\| \mid \bar{x} \in H, \langle \bar{w}, \bar{x} \rangle + b = 0, i = 1, \ldots, m\} \tag{172}$$

Finding the normal vector $\bar{w}$ of the optimal hyperplane is not as simple as calculating the normal vector from the class means, as given in the previous example (Equation (160)). To find the normal that provides the largest margin for the optimal hyperplane as specified above, it is necessary to solve [48]

$$\text{minimize } \tau(\bar{w}) = \frac{1}{2} \|\bar{w}\|^2 \tag{173}$$

$$\text{subject to } y_i(\langle \bar{w}, \bar{x}_i \rangle + b) \geq 1 \text{ for all } i = 1, \ldots, m \tag{174}$$

Equations (173) and (174) form a constrained optimization problem. This problem is handled using Lagrange multipliers $\alpha_i \geq 0$ and the Lagrangian

$$L(\bar{w}, b, \bar{\alpha}) = \frac{1}{2} \|\bar{w}\|^2 - \sum_{i=1}^{m} \alpha_i (y_i(\langle \bar{w}, \bar{x}_i \rangle + b) - 1) \tag{175}$$

where $\bar{\alpha} = (\alpha_1, \ldots, \alpha_m)$. A saddle point must be found in order to minimize the Lagrangian with respect to $\bar{w}$ and b, and maximize with respect to α_i. At the saddle point, the derivatives of L with respect to $\bar{w}$ and b must vanish. $\frac{\partial}{\partial b} L(\bar{w}, b, \bar{\alpha}) = 0$ gives

$$\sum_{i=1}^{m} \alpha_i y_i = 0 \tag{176}$$

while $\frac{\partial}{\partial \bar{w}} L(\bar{w}, b, \bar{\alpha}) = 0$ gives

$$\bar{w} = \sum_{i=1}^{m} \alpha_i y_i \bar{x}_i \tag{177}$$

Equation (177) demonstrates that the normal vector has an expansion in terms of a subset of the training points $\bar{x}_i$, those with non-zero α_i. These points are the Support Vectors mentioned at the end of the previous example. The Support Vectors obey the condition

$$\alpha_i \left[y_i \left(\langle \bar{x}_i, \bar{w} \rangle + b \right) - 1 \right] = 0 \text{ for all } i = 1, \ldots, m \tag{178}$$

where $\alpha_i \neq 0$. Thus, they lie on the margin defining the hyperplane, which is scaled to have the value 1. All other training points that do not meet this condition have $\alpha_i = 0$ and do not appear in the expansion of the hyperplane's normal vector, Equation (177). The hyperplane does not depend on these points; it depends only on the points closest to it. [48]

We can substitute Equations (176) and (177) into Equation (175) in order to arrive at the form that is normally solved [48]:

$$\text{maximize } W(\bar{\alpha}) = \sum_{i=1}^{m} \alpha_i - \frac{1}{2} \sum_{i,j=1}^{m} \alpha_i \alpha_j y_i y_j \langle \bar{x}_i, \bar{x}_j \rangle \tag{179}$$

$$\text{subject to } \alpha_i \geq 0 \text{ for all } i = 1, \ldots, m \text{ and } \sum_{i=1}^{m} \alpha_i y_i = 0 \tag{180}$$

for $\bar{\alpha} \in \mathbb{R}^m$. This is a dual optimization problem. Finally, Equation (177) can be substituted into Equation (170) in order to obtain the decision function [48]

$$f(\bar{x}) = \text{sgn} \left(\sum_{i=1}^{m} \alpha_i y_i \langle \bar{x}, \bar{x}_i \rangle + b \right) \tag{181}$$

where b is found using condition (178). However, we wish to express the optimization problem and the decision function in terms of the input data rather than the feature

space vectors. To do this, we recall Equation (157) and employ the same substitution used in the simple dot product example, which is called the *kernel trick*. The optimization problem and decision function become [48]

$$\begin{aligned} &\text{maximize } W(\bar{\alpha}) = \sum_{i=1}^{m} \alpha_i - \frac{1}{2} \sum_{i,j=1}^{m} \alpha_i \alpha_j y_i y_j k(x_i, x_j) \\ &\text{subject to condition (180)} \end{aligned} \tag{182}$$

$$f(\bar{x}) = \text{sgn}\left(\sum_{i=1}^{m} \alpha_i y_i k(x, x_i) + b \right) \tag{183}$$

Figure 43 is a visual example of a Support Vector classifier, which illustrates the concepts described thus far. It uses the kernel: $k(x, x') = e^{-\|x-x'\|^2}$. The center line is the dividing hyperplane. The outer lines trace the margins, which are the distance of the closest points to the hyperplane. The margins have the value 1, and the circled data points that lie on the margins are the Support Vectors. [48]

Classification is simple when there is a clear separation between data. However, it becomes more difficult, and a hyperplane may not exist, if there is a high noise level or overlap of the two classes. In order to allow for this overlap and data that violates condition (174), we introduce *slack variables*:

$$\xi_i \geq 0 \text{ for all } i = 1, \ldots, m \tag{184}$$

which cause the constraint (174) to become

$$y_i(\langle \bar{w}, \bar{x}_i \rangle + b) \geq 1 - \xi_i \text{ for all } i = 1, \ldots, m \tag{185}$$

Then, a good "soft margin" classifier is found by controlling both $\|\bar{w}\|$ and the sum of the slacks $\sum_i \xi_i$. The sum provides an upper bound on the number of training errors.

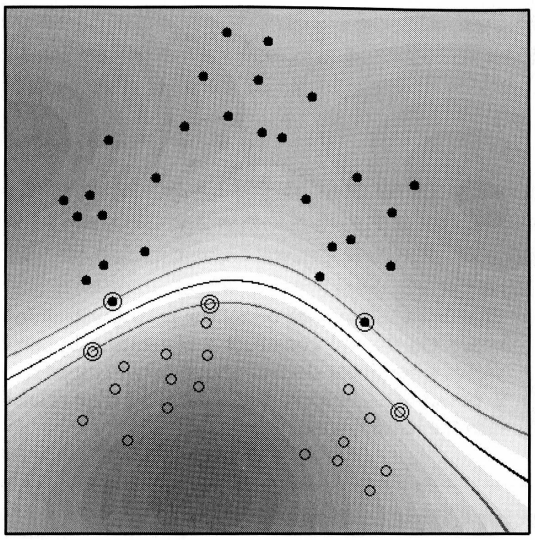

Figure 43. SV Classifier Example (reproduced from [48]). Two classes, represented by empty and filled circles, are classified using a radial basis function kernel $k(x, x') = e^{-\|x-x'\|^2}$. The center line is the decision hyperplane; the outer lines represent the constraint (174) and have the value 1. The data points located on these outer lines are marked by additional circles; these are the Support Vectors found by the classification algorithm. Note that they are the data points closest to the boundary between the classes.

[48]

The simplest case of a soft margin classifier is the C-Support Vector, or C-SV, classifier, which multiplies the sum of the slack variables by a constant $C > 0$ that determines the trade-off between the maximum margin and minimum training error. The hyperplane is found by solving

$$\text{minimize } \tau(\bar{w}, \bar{\xi}) = \frac{1}{2} \|\bar{w}\|^2 + \frac{C}{m} \sum_{i=1}^{m} \xi_i \tag{186}$$

where $\bar{w} \in H^m$, and $\xi \in \mathbb{R}^m$ (compare to Equation (173)), subject to the constraints (184) and (185). A point $\bar{x}_i$ with $\xi_i = 0$ is then not a margin error, but a Support Vector, because (185) will simplify to (174). The solution of Equation (186) has the same expansion of Equation (177), and the coefficients α_i are found by solving the quadratic optimization problem of Equation (182). This time, however, α_i has the additional constraint $0 \leq \alpha_i \leq \frac{C}{m}$ for all $i = 1, \ldots, m$. [48]

To find the threshold b, we consider Support Vectors $\bar{x}_j$, for which $\xi_j = 0$, and the equality holds in Equation (185). Equation (185) becomes

$$y_j(\langle \bar{w}, \bar{x}_j \rangle + b) = 1 \tag{187}$$

Note the change in index to distinguish the subscript j from the subscript i in the expansion in the following step. We expand using Equations (177) and (157):

$$y_j \left(\sum_{i=1}^{m} \alpha_i y_i k(x_i, x_j) + b \right) = 1 \tag{188}$$

and divide by y_j to obtain

$$\sum_{i=1}^{m} \alpha_i y_i k(x_i, x_j) + b = y_j \tag{189}$$

keeping in mind that $y_i = \pm 1$ which allows the simplification of $1/y_i$ to y_i on the right-hand side. Finally, we solve for b

$$b = y_j - \sum_{i=1}^{m} \alpha_i y_i k(x_i, x_j) \tag{190}$$

The threshold is then obtained by averaging b over all Support Vectors x_j, which all have $\alpha_j > 0$, but with the additional constraint that $\alpha_j < C$. [48]

The constant C allows us to balance the minimum training error with the maximum margin [48]. A large C penalizes inaccuracies and creates a classifier that is more accurate on the training data. A small C instead penalizes a complicated model. This penalty is driven by the idea that simplified models are more robust compared to complicated models, and thus preferred - simplified models may be inaccurate, but their performance generalizes more readily to future data [45]. Choosing the best C, however, is difficult; there is no a priori method of finding it [48].

A modification of the C-SV classifier replaces C by two new parameters ν and ρ. In this case, the problem needing solving, which is called the ν-SV classifier, is

$$\text{minimize } \tau(\bar{w}, \bar{\xi}, \rho) = \frac{1}{2} \|\bar{w}\|^2 - \nu\rho + \frac{1}{m} \sum_{i=1}^{m} \xi_i \tag{191}$$

$$\text{subject to } y_i(\langle \bar{x}_i, \bar{w} \rangle + b) \geq \rho - \xi_i \tag{192}$$

$$\text{and } \xi_i \geq 0,\ \rho \geq 0. \tag{193}$$

where $\bar{w} \in H^m$, $\xi \in \mathbb{R}^m$, and $\rho, b \in \mathbb{R}$. The parameter ρ, which needs to be optimized, helps to determine the margin of separation between the two classes. For $\xi = 0$, the margin is $2\rho/\|\bar{w}\|$. The parameter ν is an upper bound on the fraction of margin errors - the points that are either errors or lie within the margin - and a lower bound on the fraction of Support Vectors. Increasing ν increases the margin, but allows more

errors [48], so it penalizes a complicated model rather than inaccuracies. Conversely, a small ν penalizes inaccuracies rather than complexity, and results in a classifier that is more accurate on the training set. A benefit of using the ν-SV classifier is that ν has the statistical interpretation that it tends toward the fraction of misclassified points as the number of points becomes large. [45]

To derive the quadratic optimization problem for ν-SV classification, we once again begin with the Lagrangian [48]

$$\begin{aligned} L(\bar{w}, \bar{\xi}, b, \rho, \bar{\alpha}, \bar{\beta}, \delta) =& \frac{1}{2} \|\bar{w}\|^2 - \nu\rho + \frac{1}{m} \sum_{i=1}^{m} \xi_i \\ & - \sum_{i=1}^{m} (\alpha_i (y_i (\langle \bar{x}_i, \bar{w} \rangle + b) - \rho + \xi_i) + \beta_i \xi_i) - \delta\rho \end{aligned} \tag{194}$$

where $\alpha_i, \beta_i, \delta_i \geq 0$. As before, the Lagrangian must be minimized with respect to the primal variables $\bar{w}, \bar{\xi}, b, \rho$, and maximized with respect to dual variables $\bar{\alpha}, \bar{\beta}, \delta$. The partial derivatives with respect to the four primal variables are each calculated and set equal to zero, which results in the four conditions [48]

$$\bar{w} = \sum_{i=1}^{m} \alpha_i y_i \bar{x}_i \tag{195}$$

$$\alpha_i + \beta_i = \frac{1}{m} \tag{196}$$

$$\sum_{i=1}^{m} \alpha_i y_i = 0 \tag{197}$$

$$\sum_{i=1}^{m} \alpha_i - \delta = \nu \tag{198}$$

In order to arrive at the quadratic optimization problem, we substitute Equations (195) and (196) into the Lagrangian (194), and apply the kernel-dot product substitution (157). The optimization problem becomes

$$\text{maximize } W(\bar{\alpha}) = -\frac{1}{2}\sum_{i,j=1}^{m} \alpha_i \alpha_j y_i y_j k(x_i, x_j) \tag{199}$$

$$\text{subject to } 0 \leq \alpha_i \leq \frac{1}{m}, \tag{200}$$

$$\sum_{i=1}^{m} \alpha_i y_i = 0, \tag{201}$$

$$\sum_{i=1}^{m} \alpha_i \geq \nu \tag{202}$$

with the decision function, as in Equation (183), taking the form

$$f(\bar{x}) = \text{sgn}\left(\sum_{i=1}^{m} \alpha_i y_i k(x, x_i) + b\right) \tag{203}$$

Note that $\sum_{i=1}^{m} \alpha_i$ no longer appears in Equation (199). The threshold b is found by

$$b = -\frac{1}{2s}\sum_{x \in S_+ \bigcup S_-} \sum_{j=1}^{m} \alpha_j y_j k(x, x_j) \tag{204}$$

where $s > 0$ is the size of two sets S_+, where $y = +1$, and S_-, where $y = -1$, which contain Support Vectors x_i with $0 < \alpha_i < 1$. The margin parameter ρ does not need to be found to calculate the decision function. [48]

It is the ν-SV classifier which will be used to distinguish radar signals of children from those of adults. The classification program using this type of classifier was developed by Erdmann [45]. The program uses an interior-point primal-dual trust-region algorithm [49, 50, 51], with the method from [51] for controlling the weighting between primal and dual optimality conditions.

Appendix C. Covariances of CDC Anthropometric Data

This appendix displays the covariance matrices for the average anthropometric measurements given in the National Health Statistics Report by the Centers for Disease Control and Prevention (CDC), titled *Anthropometric Reference Data for Children and Adults: United States, 2003-2006* [33].

Table 8. Covariances of CDC Anthropometric Measurements, Ages 2-80

	Age	**Height**	**Waist Circ.**	**Mid-Arm Circ.**	**Upper-Arm Leng.**
Age	455.03	304.64	294.57	85.89	84.15
Height	304.64	679.49	408.33	146.79	167.30
Waist Circ.	294.57	408.33	294.85	99.41	104.03
Mid-Arm Circ.	85.89	146.79	99.41	35.11	36.85
Upper-Arm Leng.	84.15	167.30	104.03	36.85	41.49

Table 8 lists the covariances for the given physical measurements of subjects in the age range 2-80. The data for height, waist circumference, mid-arm circumference, and upper-arm length was given for children of each age from 2-19, but was given only for each decade for adults from age 20-80. However, for the measurements of calf circumference, upper-leg length, and mid-thigh circumference, the data was given for children of each age from 8-19, rather than 2-19. The covariances for these latter anthropometric dimensions are calculated and displayed separately, in Table 9.

Table 9. Covariances of CDC Anthropometric Measurements, Ages 8-80

	Age	**Calf Circ.**	**Upper-Leg Leng.**	**Mid-Thigh Circ.**
Age	477.46	35.79	8.27	33.16
Calf Circ.	35.79	12.32	10.17	16.82
Upper-Leg Leng.	8.27	10.17	12.00	14.44
Mid-Thigh Circ.	33.16	16.82	14.44	23.94

Appendix D. MatLab Code

The following documentation provides the MatLab code used to process the radar data for this thesis. Note that code not produced by this author (such as the Support Vector Machine code [45]) is not provided; it may be obtained from appropriate sources. The provided code also assumes radar data is input in the correct format (obtained by an Agilent 8714ES RF Network Analyzer). The code is provided primarily as reference for the operations used. Manipulation of input data or adjustment of the code may be needed in order to employ the code in other applications.

The code provided is as follows: a function to process Agilent 8714ES RF Network Analyzer data files, code used to apply various processing methods to the radar data, code to isolate data vectors for SVM analysis, and PCA code.

```
1  % Function to read VNA data files
2  % Stephanie Keith
3  % AFIT Masters Student
4  % 9/19/12
5
6  function [ RealData, ImagData, Freq, fileNum, baddata_loc ] = ...
7      AgilentOldVNARead
8  %AgilentOldVNARead reads .s1p files (openable with Wordpad or ...
       Notepad)
9  %produced by the Agilent 8714ES RF Network Analyzer ...
       300kHz-3000MHz (VNA),
10 %assuming a specific file naming convention
11 %   The file naming convention must match: 'TRACE##.s1p', give or
12 %   take the presence of the numbers '#'. Generally, there will ...
       be no more
13 %   than 30 traces per subject due to the space limitation of the ...
       VNA's
```

```
14 %   internal hard drive and the time it takes to run the subjects.
15 %   This program works with no change, if placed in the same ...
       directory as
16 %   the files it reads.
17 %   INPUTS - none
18 %   OUTPUTS
19 %       RealData - real data from the VNA files. Data from a ...
       single file is
20 %       oriented vertically down a column. Multiple files are ...
       stored across
21 %       the columns; each column is data from a new file.
22 %       ImagData - imaginary data from the VNA files. Data from a ...
       single
23 %       file is
24 %       oriented vertically down a column. Multiple files are ...
       stored across
25 %       the columns; each column is data from a new file.
26 %       Freq - frequency data from the VNA files. Data from a ...
       single file
27 %       is
28 %       oriented vertically down a column. Multiple files are ...
       stored across
29 %       the columns; each column is data from a new file.
30 %       fileNum - the numbers identifying the file names. ...
       Provides an easy
31 %       reference of the original file name. NaN indicates no ...
       number was
32 %       present in that location of the original file name.
33 %       baddata_loc - gives the column number of bad data, ...
       designated by
34 %       -9999999. This is also the row number in fileNum, ...
       indicating the
```

```
35 %       file with bad data.
36
37 %       The columns of RealData, ImagData, Freq correspond to ...
       each other,
38 %       and to the rows of fileNum. For X files with Y rows of data,
39 %       RealData, ImagData, Freq will all be (Y,X); fileNum will ...
       be (X,1)
40
41     % Find the "name" of all the files we want to load
42
43     files = dir('*.s1p'); % returns names of all *.s1p files ...
           within the
44     % directory in a vector
45     % We want files of the form:
46     % TRACE##.s1p
47     % where the numbers indicate the trace number.
48
49     count = 1;
50     for i=1:numel(files) % loops from 1 to number of elements in ...
           files
51
52         numberStr = ...
               regexp(files(i).name,'TRACE(\d*\d*).S1P','tokens');
53         % NOTE: NAME IS CASE SENSITIVE.
54
55         if isempty(numberStr)≠1 % if numberStr is NOT empty
56             % (i.e. we found a file with a matching name)
57
58             % This block isolates and saves the identifying ...
                   numbers in
59             % the file names.
60             numberStr = numberStr{1}; % draw out the values from the
```

```
61              % single cell they are stored in
62              fileNum(count,:) = str2double(numberStr); % convert these
63              % values to numbers
64
65              count = count+1; % increment count
66
67          end
68
69      end
70
71      fileNum = sort(fileNum);
72      % Files were not read in in ascending order by number
73      % (which indicates angle). This command sorts the
74      % fileNum vector key in ascending order in order for the ...
            following
75      % operations to proceed logically through the angular sweep ...
            around the
76      % subject.
77
78      % Load data
79
80      count = 1;
81      baddata_loc = -1; %initialize location of bad data. -1 means no
82      % bad data.
83      for i=1:length(fileNum)
84
85          fileName = ['TRACE' int2str(fileNum(i,1)) '.S1P'];
86
87          % Read data using textscan command
88          fileID = fopen(fileName); %assigns number to file location
89
90          % Test to make sure we have valid data:
```

```
91          data = textscan(fileID, '%[! HP8714ES: E.06.02]'); % ...
                reads what
92          % SHOULD be first line of proper file
93          frewind(fileID); % restarts the reading of the file from the
94          % beginning, otherwise it will pick up where it left off
95
96          if strcmp(data{1,1}{1,1}, '! HP8714ES: E.06.02 ') == 1
97              % compares the two strings; matching strings in ...
                    strcmp return 1
98
99              data = textscan(fileID, '%f %f %f',...
100                 'HeaderLines',3,'CollectOutput',1);
101             fclose(fileID); %closes file
102
103             allVNA = data{1}; %All VNA data
104
105             RealData(:,i) = allVNA(:,2); % real part of the ...
                    returned signal
106             ImagData(:,i) = allVNA(:,3); % imaginary part of the
107             % returned signal
108             Freq(:,i) = allVNA(:,1); % frequency (MHz)
109
110         else
111
112             % File cannot be read, input bad data marker
113             RealData(:,i) = -9999999;
114             ImagData(:,i) = -9999999;
115             Freq(:,i) = -9999999;
116
117             baddata_loc(count) = i;
118             % record location of bad data; refer to location in ...
                    fileNum
```

```
            % to see the file name indices
            count = count+1;

        end

    end

end
```

```
% Data Processing Code
% Stephanie Keith
% AFIT Masters Student
% 2 Mar 2013

clear all; close all

%% Read Background - need only run once if Background.mat not exist

% Read Background (consisting of turntable behind walls)
fileName = 'turntable only.S1P';
fileID = fopen(fileName); %assigns number to file location
data = textscan(fileID, '%f %f %f',...
    'HeaderLines',3,'CollectOutput',1);
fclose(fileID); %closes file

allVNA = data{1}; %All VNA data

BackReal = allVNA(:,2); % real part of the returned signal
BackImag = allVNA(:,3); % imaginary part of the returned signal

```

```
22 Back = BackReal + BackImag*1i;
23
24 save Background Back
25
26 clear all;
27
28 %% Read Turntable — need only run once if Turntable.mat not exist
29
30 % Read Turntable and Back (consisting of turntable behind walls,
31 % and background with nothing but reflecting floor)
32 fileName = 'Turntable only&cloth.S1P';
33 fileID = fopen(fileName); %assigns number to file location
34 data = textscan(fileID, '%f %f %f',...
35     'HeaderLines',3,'CollectOutput',1);
36 fclose(fileID); %closes file
37
38 allVNA = data{1}; %All VNA data
39
40 TurnReal = allVNA(:,2); % real part of the returned signal
41 TurnImag = allVNA(:,3); % imaginary part of the returned signal
42
43 Turn = TurnReal + TurnImag*1i;
44
45 fileName = 'Back—nothing.S1P';
46 fileID = fopen(fileName); %assigns number to file location
47 data = textscan(fileID, '%f %f %f',...
48     'HeaderLines',3,'CollectOutput',1);
49 fclose(fileID); %closes file
50
51 allVNA = data{1}; %All VNA data
52
53 PureBackReal = allVNA(:,2); % real part of the returned signal
```

```
54 PureBackImag = allVNA(:,3); % imaginary part of the returned signal
55
56 PureBack = PureBackReal + PureBackImag*1i;
57
58 TurnOnly = Turn - PureBack;
59
60 save Turntable TurnOnly
61
62 clear all;
63
64 %% Read Sphere for Calibration - need only run once if Sphere.mat ...
       not exist
65
66 % Stand on turntable - turntable = stand only (w back)
67 % Sphere on stand - stand = Sphere only (with turntable)
68
69 % Read Stand on turntable
70 fileName = 'stand on turntable.S1P';
71 fileID = fopen(fileName); %assigns number to file location
72 data = textscan(fileID, '%f %f %f',...
73     'HeaderLines',3,'CollectOutput',1);
74 fclose(fileID); %closes file
75
76 allVNA = data{1}; %All VNA data
77
78 StandonTurnReal = allVNA(:,2); % real part of the returned signal
79 StandonTurnImag = allVNA(:,3); % imaginary part of the returned ...
       signal
80
81 StandonTurn = StandonTurnReal + StandonTurnImag*1i;
82
83 load Turntable
```

```
load Background

% Determine signature of isolated stand with back
Stand = StandonTurn - TurnOnly;

% Determine signature of isolated stand, no back
StandOnly = StandonTurn - TurnOnly - Back;

% Read Ball on stand on turntable
fileName = 'Ball on stand on turntable.S1P';
fileID = fopen(fileName); %assigns number to file location
data = textscan(fileID, '%f %f %f',...
    'HeaderLines',3,'CollectOutput',1);
fclose(fileID); %closes file

allVNA = data{1}; %All VNA data

BallonStandReal = allVNA(:,2); % real part of the returned signal
BallonStandImag = allVNA(:,3); % imaginary part of the returned ...
    signal

BallonStand = BallonStandReal + BallonStandImag*1i;

% Determine Ball w effects of turn, but no stand or back
Ball_w_Turn = BallonStand - Stand;

% Determind Ball w/o stand, turntable, or background (pureball)
BallOnly = BallonStand - StandonTurn;

% Determine ball with only background, no turntable, not stand
Ball_w_Back = BallonStand - TurnOnly - StandOnly;

```

```
115 save Sphere Ball_w_Turn BallOnly Ball_w_Back
116
117 clear all;
118
119 %% Load Data
120
121 load Adult
122 load Child
123 load Background
124 load Turntable
125 load Sphere
126
127 %% Apply Background Subtraction - optional
128
129 for i = 1:size(AdultData,2)
130     AdultData(:,i) = AdultData(:,i) - Back;
131 end
132
133 for i = 1:size(ChildData,2)
134     ChildData(:,i) = ChildData(:,i) - Back;
135 end
136
137 %% Apply Turntable Only Subtraction - optional
138 % do not run if Background Subtraction already applied
139
140 for i = 1:size(AdultData,2)
141     AdultData(:,i) = AdultData(:,i) - TurnOnly;
142 end
143
144 for i = 1:size(ChildData,2)
145     ChildData(:,i) = ChildData(:,i) - TurnOnly;
146 end
```

```
147
148 %% Define constants
149
150 % Define speed of light (m/s)
151 c = 299792458;
152
153 K = 1601; % The number of frequency bins per pulse
154 Np = 1; % The number of pulses
155 Nfft = 1601; % Size of the FFT to form the range profile
156
157 minF = 400e6; % lowest frequency of pulse
158 maxF = 800e6; % highest frequency of pulse
159 ΔF = (maxF - minF)/K; % frequency step from sample to sample
160 dr = c/(2*ΔF*K); % range resolution
161
162 % Determine the maximum scene size of the image (m)
163 maxWr = c/(2*ΔF); % maximum range
164
165 % Display maximum scene size and resolution (range
166 fprintf('Maximum Scene Size: %.2f m range \n',maxWr);
167 fprintf('Resolution: %.2f m range \n',dr);
168
169 % Calculate the range to every bin in the range profile (m)
170 r_vec = linspace(-Nfft/2,Nfft/2-1,Nfft)*maxWr/Nfft;
171
172 %% IFFT, No Window
173
174 % IFFT
175 for i=1:size(AdultData,2) % for each data set from each file ...
       (across cols)
176     if AdultData(1,i) == -9999999 %indicates column of bad data
177         IFFT_Adult(:,i) = -9999999;
```

```
178     else
179         IFFT_Adult(:,i) = fftshift(ifft(AdultData(:,i),Nfft));
180     end
181 end
182
183 for i=1:size(ChildData,2) % for each data set from each file ...
        (across cols)
184     if ChildData(1,i) == -9999999 %indicates column of bad data
185         IFFT_Child(:,i) = -9999999;
186     else
187         IFFT_Child(:,i) = fftshift(ifft(ChildData(:,i),Nfft));
188     end
189 end
190
191 %Isolate peak data
192 Iso_IFFT_Adult = IFFT_Adult(816:832,:);
193 Iso_IFFT_Child = IFFT_Child(816:832,:);
194 IsoVec = r_vec(816:832);
195
196 for i = 1:size(IFFT_Adult,2)
197     Iso_Freq_Adult(:,i) = fft(fftshift(Iso_IFFT_Adult(:,i)));
198 end
199
200 for i = 1:size(IFFT_Child,2)
201     Iso_Freq_Child(:,i) = fft(fftshift(Iso_IFFT_Child(:,i)));
202 end
203
204 % save Freq AdultData ChildData
205 % save Time IFFT_Adult IFFT_Child
206
207 %% IFFT, Window
208
```

```
209 % Hamming window
210 hamm = hamming(1601);
211
212 Window_Adult = zeros(size(AdultData,1),size(AdultData,2));
213 for i = 1:size(AdultData,2)
214     Window_Adult(:,i) = hamm.*AdultData(:,i);
215 end
216
217 IFFT_Adult_Win = zeros(size(AdultData,1),size(AdultData,2));
218 for i=1:size(AdultData,2) % for each data set from each file ...
       (across cols)
219     if AdultData(1,i) == -9999999 %indicates column of bad data
220         IFFT_Adult_Win(:,i) = -9999999;
221     else
222         IFFT_Adult_Win(:,i) = fftshift(ifft(Window_Adult(:,i),Nfft));
223     end
224 end
225
226 Window_Child = zeros(size(ChildData,1),size(ChildData,2));
227 for i = 1:size(ChildData,2)
228     Window_Child(:,i) = hamm.*ChildData(:,i);
229 end
230
231 IFFT_Child_Win = zeros(size(ChildData,1),size(ChildData,2));
232 for i=1:size(ChildData,2) % for each data set from each file ...
       (across cols)
233     if ChildData(1,i) == -9999999 %indicates column of bad data
234         IFFT_Child_Win(:,i) = -9999999;
235     else
236         IFFT_Child_Win(:,i) = fftshift(ifft(Window_Child(:,i),Nfft));
237     end
238 end
```

```
239
240 for i = 1:size(AdultData,2)
241     Freq_Adult_Win(:,i) = fft(fftshift(IFFT_Adult_Win(:,i)));
242 end
243
244 for i = 1:size(ChildData,2)
245     Freq_Child_Win(:,i) = fft(fftshift(IFFT_Child_Win(:,i)));
246 end
247
248 % Isolate peak data
249 Iso_IFFT_Child_Win = IFFT_Child_Win(816:832,:);
250 Iso_IFFT_Adult_Win = IFFT_Adult_Win(816:832,:);
251
252 for i = 1:size(AdultData,2)
253     Iso_Freq_Adult_Win(:,i) = fft(fftshift(Iso_IFFT_Adult_Win(:,i)));
254 end
255
256 for i = 1:size(ChildData,2)
257     Iso_Freq_Child_Win(:,i) = fft(fftshift(Iso_IFFT_Child_Win(:,i)));
258 end
259
260 % save Freq_Win Freq_Adult_Win Freq_Child_Win
261 % save Time_Win IFFT_Adult_Win IFFT_Child_Win
262
263 %% Apply filtering to windowed data, full data used
264 close all;
265
266 %Calculate range bin size
267 N=1601;%Number of frequencies, potentially chopped.
268
269 %Calculate filter parameters
270 fo=1601;
```

```
271
272 rvec_new = r_vec + abs(r_vec(1));
273 extent = rvec_new(N);
274
275 F = [0 5.5+ abs(r_vec(1)) 6.5+ abs(r_vec(1)) 9.5+ abs(r_vec(1))...
276     10.5+ abs(r_vec(1)) extent]/extent; A = [0 0 1 1 0 0];
277 b = firpm(fo,F,A);
278 filt=b(:);
279 save filter filt
280 [h,w] = freqz(b,1,N);
281
282 figure;
283 plot(F,A,w/pi,abs(h))
284 legend('Ideal','firpm Design')
285
286 % Apply filter to Data
287 filtAdult = IFFT_Adult_Win;
288 for i = 1:size(AdultData,2)
289     filtAdult(:,i) = h.*filtAdult(:,i);
290 end
291
292 filtChild = IFFT_Child_Win;
293 for i = 1:size(ChildData,2)
294     filtChild(:,i) = h.*filtChild(:,i);
295 end
296
297 for i = 1:size(AdultData,2)
298     Freq_filtAdult(:,i) = fft(fftshift(filtAdult(:,i)));
299 end
300
301 for i = 1:size(ChildData,2)
302     Freq_filtChild(:,i) = fft(fftshift(filtChild(:,i)));
```

```
303 end
304
305 % Isolate peak data
306 Iso_filtChild = filtChild(816:832,:);
307 Iso_filtAdult = filtAdult(816:832,:);
308
309 for i = 1:size(AdultData,2)
310     Iso_Freq_filtAdult(:,i) = fft(fftshift(Iso_filtAdult(:,i)));
311 end
312
313 for i = 1:size(ChildData,2)
314     Iso_Freq_filtChild(:,i) = fft(fftshift(Iso_filtChild(:,i)));
315 end
316
317 % save Freq_Win_Filt Freq_filtAdult Freq_filtChild
318 % save Time_Win_Filt filtAdult filtChild
319
320 %% Compare Pure Mie with Measured Mie
321
322 close all;
323
324 numfreqs=1601;%number of frequencies entered in the vna
325 msm=zeros(numfreqs,3);%mie scattering matrix
326 freq=400e6:400e6/1600:800e6;
327
328 msm(:,1)=freq';
329 i=1;
330 for f=400e6:400e6/1600:800e6
331      [msm(i,2) msm(i,3)]=miePEC(.25,f,0,0,20); % miePEC is Mie ...
           scattering
332      % code found in the online MatLab database, Author: Walton ...
           C. Gibson,
```

```
333       % Tripoint Industries, Inc.
334       i=i+1;
335   end
336
337   figure;
338   plot(msm(:,1),20*log10(abs(msm(:,2))));
339
340   % Filter Measured Sphere
341   % IFFT
342   IFFT_Ball = fftshift(ifft(BallOnly,Nfft));
343
344   filtBall = h.*IFFT_Ball;
345
346   %% Apply Mie Calibration - Ball w Background only (no stand, ...
          turntable)
347
348   % close all;
349
350   IFFT_Ball = fftshift(ifft(Ball_w_Back,Nfft));
351
352   filtBall = h.*IFFT_Ball;
353
354   % Operate in log, so we can add/subtract
355   MeasSphere = 20*log10(abs(fft(fftshift(filtBall))));
356   PerfectSphere = 20*log10(abs(msm(:,2)));
357
358   for i = 1:size(AdultData,2)
359       MeasAdult(:,i) = 20*log10(abs(fft(fftshift(filtAdult(:,i)))));
360   end
361
362   for i = 1:size(ChildData,2)
363       MeasChild(:,i) = 20*log10(abs(fft(fftshift(filtChild(:,i)))));
```

```
364 end
365
366 Cal_factor = MeasSphere - PerfectSphere;
367
368 PerfectAdult = zeros(size(AdultData,1),size(AdultData,2));
369 for i = 1:size(AdultData,2)
370     PerfectAdult(:,i) = MeasAdult(:,i)- Cal_factor;
371 end
372
373 PerfectChild = zeros(size(ChildData,1),size(ChildData,2));
374 for i = 1:size(ChildData,2)
375     PerfectChild(:,i) = MeasChild(:,i)- Cal_factor;
376 end
377
378 PerfectChild_Time = zeros(size(ChildData,1),size(ChildData,2));
379 for i = 1:size(ChildData,2)
380     PerfectChild_Time(:,i) = ...
381         20*log10(abs(fftshift(ifft(PerfectChild(:,i),Nfft))));
382 end
383
384 PerfectAdult_Time = zeros(size(AdultData,1),size(AdultData,2));
385 for i = 1:size(AdultData,2)
386     PerfectAdult_Time(:,i) = ...
387         20*log10(abs(fftshift(ifft(PerfectAdult(:,i),Nfft))));
388 end
389
390 % save Freq_Win_Filt_Mie PerfectAdult PerfectChild
391 % save Time_Win_Filt_Mie PerfectAdult_Time PerfectChild_Time
392
393 %% Reduced Vectors Based on Time Domain Features, Turntable Sub, ...
       Windowing
394
```

```
395 IFFT_Adult_Win = 20.*log10(abs(IFFT_Adult_Win));
396 IFFT_Child_Win = 20.*log10(abs(IFFT_Child_Win));
397
398 % Locate Relevant Peaks - always located in same position in data
399 TargPeakA = IFFT_Adult_Win(823,:);
400 TargPeakC = IFFT_Child_Win(823,:);
401 LeftPeakA = IFFT_Adult_Win(818,:);
402 LeftPeakC = IFFT_Child_Win(818,:);
403 RightPeakA = IFFT_Adult_Win(829,:);
404 RightPeakC = IFFT_Child_Win(829,:);
405
406 % Find Valley Depth between Targ and Left Peak
407 for i=1:size(AdultData,2)
408     [LeftMinA(i), LeftMinLocA(i)] = min(IFFT_Adult_Win(818:823,i));
409     [RightMinA(i), RightMinLocA(i)] = min(IFFT_Adult_Win(823:829,i));
410 end
411 LeftMinVecLocA = 817+LeftMinLocA;
412 RightMinVecLocA = 822+RightMinLocA;
413
414 LeftMinLocA = r_vec(LeftMinVecLocA);
415 RightMinLocA = r_vec(RightMinVecLocA);
416
417 for i=1:size(ChildData,2)
418     [LeftMinC(i), LeftMinLocC(i)] = min(IFFT_Child_Win(818:823,i));
419     [RightMinC(i), RightMinLocC(i)] = min(IFFT_Child_Win(823:829,i));
420 end
421
422 LeftMinVecLocC = 817+LeftMinLocC;
423 RightMinVecLocC = 822+RightMinLocC;
424
425 LeftMinLocC = r_vec(LeftMinVecLocC);
426 RightMinLocC = r_vec(RightMinVecLocC);
```

```
427
428 LeftValleyDepthA = TargPeakA - LeftMinA;
429 RightValleyDepthA = TargPeakA - RightMinA;
430
431 LeftValleyDepthC = TargPeakC - LeftMinC;
432 RightValleyDepthC = TargPeakC - RightMinC;
433
434 % Find Width of Target Peak
435 for j=1:size(AdultData,2)
436
437     if LeftValleyDepthA(j) > RightValleyDepthA(j)
438
439         start = LeftMinVecLocA(j);
440         i = start +1;
441         while IFFT_Adult_Win(start,j)<IFFT_Adult_Win(i,j)
442             i = i+1;
443         end
444
445         startend = i;
446
447         PeakWidthA(j) = r_vec(i)-r_vec(start);
448
449     elseif LeftValleyDepthA(j) < RightValleyDepthA(j)
450
451         start = RightMinVecLocA(j);
452         i = start -1;
453         while IFFT_Adult_Win(start,j)<IFFT_Adult_Win(i,j)
454             i = i-1;
455         end
456
457         startend = i;
458         PeakWidthA(j) = r_vec(start)-r_vec(i);
```

```
459
460      end
461
462  end
463
464  for j=1:size(ChildData,2)
465
466      if LeftValleyDepthC(j) > RightValleyDepthC(j)
467
468          start = LeftMinVecLocC(j);
469          i = start +1;
470          while IFFT_Child_Win(start,j)<IFFT_Child_Win(i,j)
471              i = i+1;
472          end
473
474          startend = i;
475
476          PeakWidthC(j) = r_vec(i)-r_vec(start);
477
478      elseif LeftValleyDepthC(j) < RightValleyDepthC(j)
479
480          start = RightMinVecLocC(j);
481          i = start -1;
482          while IFFT_Child_Win(start,j)<IFFT_Child_Win(i,j)
483              i = i-1;
484          end
485
486          startend = i;
487          PeakWidthC(j) = r_vec(start)-r_vec(i);
488
489      end
490
```

```
491 end
492
493 ReducedAdult = [TargPeakA; LeftPeakA; RightPeakA; ...
       LeftValleyDepthA; ...
494     RightValleyDepthA; PeakWidthA];
495
496 ReducedChild = [TargPeakC; LeftPeakC; RightPeakC; ...
       LeftValleyDepthC; ...
497     RightValleyDepthC; PeakWidthC];
498
499 % save Reduced ReducedAdult ReducedChild
```

```
1  % Support Vector Machine Analysis of Child/Adult Radar Data
2  % Stephanie Keith
3  % AFIT Masters Student
4  % 2 Mar 2013
5
6  % This code merely isolates the data vectors for SVM analysis. ...
       The actual
7  % SVM code is indicated by the function svmblkbx, and was written ...
       by Dr.
8  % Grant Erdmann. Erdmann's code is not provided here.
9
10 clear all; close all; clc;
11
12 %% Load & Process Data for SVM
13
14 load Angles % azimuthal angles for child, adult radar data
15
16 load RadarData % child, adult radar data
```

```
17
18 % CertainAngles is a function to pull out only the angles of the ...
      adult,
19 % child data we want to process with the SVM. In this case, the ...
      angles are
20 % those closest to 0, 45, 90, 135, 180.
21 [ Adult_Single, Child_Single ] = CertainAngles( AdultData, ...
      AdultAngle,...
22     ChildData, ChildAngle );
23
24 % SVM Function requires magnitude of data (does not perform on ...
      imaginary
25 % numbers)
26 Adult = 20*log10(abs(Adult_Single));
27 Child = 20*log10(abs(Child_Single));
28
29 % Total number of adult, child vectors
30 TotNumAdult = size(Adult,2);
31 TotNumChild = size(Child,2);
32
33 TrainNumAdult = ceil(0.75*TotNumAdult); % number of training vectors
34 ValNumAdult = TotNumAdult - TrainNumAdult; % number of testing ...
      vectors
35
36 TrainNumChild = floor(0.75*TotNumChild); % number of training vectors
37 ValNumChild = TotNumChild - TrainNumChild; % number of testing ...
      vectors
38
39 %% SVM Set 1 - Take Test data from end of data vectors
40
41 clc;
42
```

```
% Build training data vector and associated identification vector ...
    (+/- 1)
TrainVec1 = [Adult(:,1:TrainNumAdult) Child(:,1:TrainNumChild)];
Class_train1 = [-ones(1,TrainNumAdult) ones(1,TrainNumChild)];

% Build testing data vector and associated identification vector ...
    (+/- 1)
TestVec1 = [Adult(:,TrainNumAdult+1:TrainNumAdult+ValNumAdult)...
     Child(:,TrainNumChild+1:TrainNumChild+ValNumChild)];
Class_test1 = [-ones(1,ValNumAdult) ones(1,ValNumChild)];

% Call SVM function (Erdmann's code)
[guess_all,trainguess_all,params_all] = ...
    svmblkbx(TrainVec1,Class_train1,...
     TestVec1,Class_test1,0.05);

%% SVM Set 2 - Take test data from start of data vectors

clc;

TrainVec2 = [Adult(:,ValNumAdult+1:ValNumAdult+TrainNumAdult)...
     Child(:,ValNumChild+1:ValNumChild+TrainNumChild)];
Class_train2 = [-ones(1,TrainNumAdult) ones(1,TrainNumChild)];

TestVec2 = [Adult(:,1:ValNumAdult) Child(:,1:ValNumChild)];
Class_test2 = [-ones(1,ValNumAdult) ones(1,ValNumChild)];

[guess_all,trainguess_all,params_all] = ...
    svmblkbx(TrainVec2,Class_train2,...
     TestVec2,Class_test2,0.05);

%% SVM Set 3 - Take data from 2nd quarter of vectors
```

```
71
72 clc;
73
74 TrainVec3 = [Adult(:,1:ValNumAdult) ...
      Adult(:,2*ValNumAdult+1:TotNumAdult)...
75     Child(:,1:ValNumChild) Child(:,2*ValNumChild+1:TotNumChild)];
76 Class_train3 = [-ones(1,TrainNumAdult) ones(1,TrainNumChild)];
77
78 TestVec3 = [Adult(:,ValNumAdult+1:2*ValNumAdult)...
79     Child(:,ValNumChild+1:2*ValNumChild)];
80 Class_test3 = [-ones(1,ValNumAdult) ones(1,ValNumChild)];
81
82 [guess_all,trainguess_all,params_all] = ...
      svmblkbx(TrainVec3,Class_train3,...
83     TestVec3,Class_test3,0.05);
84
85 %% SVM Set 4 - Take data from 3rd quarter of vectors
86
87 clc;
88
89 TrainVec4 = [Adult(:,1:2*ValNumAdult)...
90     Adult(:,3*ValNumAdult+1:TotNumAdult) Child(:,1:2*ValNumChild)...
91     Child(:,3*ValNumChild+1:TotNumChild)];
92 Class_train4 = [-ones(1,TrainNumAdult) ones(1,TrainNumChild)];
93
94 TestVec4 = [Adult(:,2*ValNumAdult+1:3*ValNumAdult)...
95     Child(:,2*ValNumChild+1:3*ValNumChild)];
96 Class_test4 = [-ones(1,ValNumAdult) ones(1,ValNumChild)];
97
98 [guess_all,trainguess_all,params_all] = ...
      svmblkbx(TrainVec4,Class_train4,...
99     TestVec4,Class_test4,0.05);
```

```
% Principal Component Analysis of Child/Adult Radar Data
% Stephanie Keith
% AFIT Masters Student
% 9 Feb 2013

close all; clear all; clc;

%% 1. Load radar data

% Load radar data consisting of adult and child data, and the vectors
% denoting the azimuthal location where each child or adult radar ...
    vector
% was taken

load Adult
load Child
load Freq

% Transform to magnitude of radar data (PCA process does not ...
    perform well
% with imaginary numbers)
Adult = 20*log10(abs(AdultData));
Child = 20*log10(abs(ChildData));

% Create full data matrix
Data = [Adult Child];
Data = Data';

%% 2. Subtract mean
```

```
28
29 Mean = mean(Data,1);
30
31 Data_Adjust = zeros(size(Data,1),size(Data,2));
32 for i = 1:size(Data,2);
33     Data_Adjust(:,i) = Data(:,i) - Mean(i);
34 end
35
36 %% 3. Calculate covariance matrix
37
38 Cov_Data = cov(Data);
39
40 %% 4. Calculate eigenvectors, eigenvalues of covariance matrix
41
42 % Note: eig returns the eigenvalues along the diagonal of a matrix;
43 % eigenvectors are returned in corresponding columns of a matrix.
44
45 [ EVecs EVals ] = eig(Cov_Data);
46
47 %% 5. Choose components, form feature vector
48
49 % Order components by eigenvalue, high to low.
50 % Isolate eigenvalues to form 1 vector rather than matrix
51
52 EVals_row = find(EVals ~= 0); % Finds eigenvalues in matrix
53 EVals_row = EVals(EVals_row)'; % Isolates them to create one vector
54 EV = [EVals_row; EVecs]; % Concatenate to eigenvectors for sorting
55 EV_sort = sortrows(EV', -1); % sort along the first row, largest ...
      vals first
56 EV_sort = EV_sort';
57
58 % Isolate feature vector, remove EVals from feature vector
```

```
59 FeatureVec_Full = EV_sort;
60 FeatureVec_Full(1,:) = []; % remove EVals
61 FeatureVec_Isol = FeatureVec_Full(:,1:3); % isolate features; use ...
       3 for max
62
63 %% 6. Derive new data set
64
65 FinalData_Full = FeatureVec_Full'*Data_Adjust';
66 FinalData_Isol = FeatureVec_Isol'*Data_Adjust';
67
68 % Transpose back into table format
69 FinalData_Full = FinalData_Full';
70 FinalData_Isol = FinalData_Isol';
71
72
73 %% 7. Get data back
74
75 Data_Recover_Full = FeatureVec_Full*FinalData_Full';
76 for i = 1:size(Data,2);
77     Data_Recover_Full2(:,i) = Data_Recover_Full(i,:)+Mean(i);
78 end
79
80 Data_Recover_Isol = FeatureVec_Isol*FinalData_Isol';
81 for i = 1:size(Data,2);
82     Data_Recover_Isol2(:,i) = Data_Recover_Isol(i,:)+Mean(i);
83 end
84
85 %% 8. Plot data (2-D or 3-D plot of 2 or 3 highest eigenvalues)
86 % Child (red circles)/Adult (blue triangles)
87
88 close all;
89
```

```
f = figure;
for i=1:size(Adult,2) % Plot adult data
    scatter3(FinalData_Isol(i,1),FinalData_Isol(i,2),...
        FinalData_Isol(i,3),...
        'MarkerEdgeColor',[0 0 1],...
        'Marker','v')
    hold on;
end
for i=(size(Adult,2)+1):size(Data,1) % Plot child data
    scatter3(FinalData_Isol(i,1),FinalData_Isol(i,2),...
        FinalData_Isol(i,3),...
        'MarkerEdgeColor',[1 0 0])
end

xlabel('x')
ylabel('y')
zlabel('z')
title('Reduced Frequency Data, PCA Analysis')
```

Appendix E. IRB Documentation (Child)

The following pages include IRB documentation for the child volunteer study. The documents are: the signed approval letter, IRB protocol, and Informed Consent Document.

DEPARTMENT OF THE AIR FORCE
AIR FORCE RESEARCH LABORATORY
WRIGHT-PATTERSON AIR FORCE BASE OHIO 45433

21 DEC 2012

MEMORANDUM FOR 711 HPW/RHXBA (DR. DUSTIN BRUENING)

FROM: 711 HPW/IR (AFRL IRB)

SUBJECT: IRB approval for the use of human volunteers in research

1. Protocol title: 3D Modeling and Identification of Pediatric Shape and Motion
2. Protocol number: FWR20120233H
3. Protocol version: 1.01
4. Risk: Minimal Risk
5. Approval date: 21 December 2012
6. Expiration date: 4 December 2013
7. Scheduled renewal date: 4 November 2013
8. Type of review: Amendment - Expedited
9. Assurance Number and Expiration Date:
   a. AFRL DoD Assurance 50002: 14 March 2014
   b. Infoscitex Corp FWA #00008359 DoD 50339 : 01 February 17
10. CITI Training: Completed
11. The above protocol has been reviewed and approved by the AFRL IRB via convened board review procedures. All requirements, as set by the IRB and its legal counsel, have been fully complied with. The investigator will use minors (a regulatory designated "vulnerable population) to include 50 healthy individuals from ages 4 – 17 years old. The objective is to characterize children's size, shape, and movement patterns in order to discriminate between children and adults using stand-off sensors as well as to develop realistic animations of children for training scenarios. A secondary aim is to develop a data base of pediatric images to share with AFRL/RYMD for future technology development. All images will be immediately de-identified and no identifiable image will be used/maintained for any purpose. Appropriate parental consent and minor assent is provided for in this study. The convened IRB determined the study to constitute minimal risk. **Amendment:** The investigator seeks to use 10 of the previously approved subjects and alter the experimentation with this sub-set of subjects to use the radar through a mock wall in order to develop an algorithm to discriminate size and shape

based upon radar images of a person. The location for this sub-set of exposures is in a different building (which has undergone safety inspection for children), but the exposure levels are no more than what is in the original protocol terms and was found to be safe exposure limits for children. Accordingly, the protocol remains minimal risk. This protocol therefore meets the criteria for expedited review in accordance with 32 CFR 219.110 (b)(2): Minor changes in previously approved research (during the period of one year or less) for which approval is authorized.

12. HIPAA authorization is not required, since no HIPAA protected information will be recorded in the execution of this protocol.

13. FDA regulations do not apply since no drugs, supplements, or unapproved medical devices will be used in this research.

14. This approval applies only to the requirements of 32 CFR 219, DoDD 3216.2, AFI 40-402, and related human research subject regulations. If this project is a survey, attitude or opinion poll, questionnaire or interview, consult AFI 38-501, AF Survey Program, for further guidance. Headquarters AFPC/DPSAS is the final approval authority for conducting attitude and opinion surveys within the Air Force. If the survey, attitude or opinion poll, questionnaire or interview is hosted on a .com server, consult AFI 33-129, Web Management and Effective Use of Internet-based Capabilities, for further guidance. If the study is being conducted under an IDE or IND, a copy of the FDA IDE or IND approval letter must be submitted by the Principal Investigator to the IRB.

15. Any serious adverse event, unexpected problems, or other issues resulting from this study should be reported immediately to the IRB. Amendments to protocols and/or revisions to informed consent documents must have IRB approval prior to implementation. Please retain both hard copy and electronic copy of the final approved protocol and informed consent document.

16. All inquiries and correspondence concerning this protocol should include the protocol number and name of the primary investigator. Please ensure the timely submission of all required progress and final reports and use the templates provided on the AFRL IRB web site http://www.wpafb.af.mil/library/factsheets/factsheet.asp?id=7496 .

17. For questions or concerns, please contact the IRB administrator, Lt Robert Walker at Robert.walker@wpafb.af.mil or (937) 904-8094. All inquiries and correspondence concerning this protocol should include the protocol number and name of the primary investigator.

KIM E. LONDON
Acting Chairman, AFRL IRB

3D Modeling and Identification of Pediatric Shape and Motion
F-WR-2012-0233-H

1. **Principal Investigator**
   a. Dustin Bruening, DR-II, Research Physiologist, 711 HPW/RHXBA, 937-255-5272, dustin.bruening@wpafb.af.mil

2. **Associate Investigators**
   a. David Bowden, DR-I, Electrical Engineer, 711 HPW/RHXBA, 937-255-8518, david.bowden@wpafb.af.mil
   b. Analee Miranda, DR-II, Research Mathematician, AFRL/RYMD, 937-528-8118, analee.miranda@wpafb.af.mil
   c. Lamar Westbrook, DR-I, Electronics Engineer, AFRL/RYMD, 937-528-8114, lamar.westbrook@wpafb.af.mil
   d. Stephanie Keith, Captain, AFIT/ENP, 937-785-3636, skeith@afit.edu
   e. Evelyn Boettcher, Researcher, Infoscitex Corp., 937-255-8810, evelyn.boettcher.ctr@wpafb.af.mil
   f. Christopher Hess, Research Technician, Infoscitex Corp., 937-255-5390, christopher.hess2@wpafb.af.mil
   g. Derek Benson, Research Technician, Infoscitex Corp., 937-255-2058, derek.benson@wpafb.af.mil
   h. Casserly Whitehead, Researcher, Infoscitex Corp, 937-255-1902, casserly.whitehead.ctr@wpafb.af.mil
   i. Kristin Spencer, 2nd Lt, Human Factors Engineer, USAF, 711 HPW/RHXBA, 937-255-7119, kristin.spencer@wpafb.af.mil
   j. Max Grattan, Research Technician, Infoscitex Corp, max.grattan.ctr@wpafb.af.mil

3. **Medical Consultant or Research Monitor**
   Not applicable

4. **Facility/Contractor**
   This research effort will be conducted by personnel from the Human Signatures Branch, Human Centered ISR Division, Human Effectiveness Directorate, Air Force Research Laboratory (711 HPW/RHXBA), as well as by RHXBA's in-house contractor, Infoscitex, under the Federal-wide Assurance Number 00008359 with the Department of Defense Addendum number F50339. In-house government personnel from the Multispectral Sensing & Detection Division, Sensors Directorate, Air Force Research Laboratory (AFRL/RYM) and a student from the Air Force Institute of Technology will also conduct this research.

5. **Objective**
   To characterize children's size, shape, and movement patterns for the purposes of: 1) discriminating between children and adults using stand-off sensors, and 2) developing realistic animations of children for training scenarios.

6. Background

Modern defense applications have become increasingly human-centric. Humans are more diverse and adaptive than conventional targets such as tanks and aircraft, and can be difficult to evaluate without a comprehensive understanding of relevant human characteristics that can be integrated into adaptive algorithms for stand-off detection. Our current research applications include: 1) identification of, or discrimination among, individuals or groups of individuals from a distance; and 2) simulating realistic human size, shape, and motion for bio-fidelic computer animations and training scenarios. (See also IRB protocol FWR20100055H). While our past focus has previously been on adult movement, there is a need to also incorporate child data into these efforts. This will broaden the variability in our human characterization databases and allow us to explore stand-off discrimination between adults and children.

7. Impact

By establishing a high-fidelity dataset of 3D human size, shape and motion signatures, we can develop automated techniques for stand-off signature recognition as well as enhance bio-fidelic human models for simulation and training applications. Ultimately, this work may lead to an increase in the safety and success of military operations.

8. Experimental Plan

a. Equipment:

3-D size and shape information will be collected using a 3DMD (Atlanta, Ga.) white-light whole body scanner. The scanner consists of 9 camera mounts, each comprising two black and white cameras, two color cameras, and one projection camera. The cameras operate similar to standard digital cameras, emitting a brief white light flash to illuminate the subject. The various camera images and views are then combined to create a high resolution 3D point cloud or mesh. The whole-body scanner does not see through clothing, but rather returns what amounts to a 3D surface camera image. Accordingly, the scanner is no more intrusive than a standard digital camera. Subject privacy will be protected as described in section **8f**.

3-D movement will be collected using one or a combination of two systems:

1. An 18 camera, passive-optical motion capture system (Motion Analysis Corp, Santa Rosa, CA). These cameras use a near infrared light to track the three-dimensional positions of small (6 - 20 mm diameter) retro-reflective markers placed on each subject's body.
2. An 18 sensor inertial system (e.g. APDM Opal, Portland OR). The wireless inertial sensors measure orientation using a combination of accelerometers, gyroscopes, and magnetometers. Neither the optical nor inertial motion capture systems collect identifying information nor are harmful to subjects.

Traditional high speed video cameras (Basler Corp, Exton PA) will also be used to record the movements. These will be synchronized with the motion capture system(s). Subject privacy will be protected as described in section **8f**.

Low-power indoor radar will be used to record the phase-doppler signatures of the test movements. Two different radar systems will be used at alternate times (not together):

1) A linear frequency modulated homodyne (LFMH) radar with separate transmission and receiving antenna units. The system is capable of supporting frequency chirp rates of up to 10 KHz while maintaining 512 frequency steps/chirp, with 10-20 cm resolution cells.

2) A bistatic, low power (less than 1 Watt) Doppler-range radar operating from 250 MHz up to 3 GHz using a pulsed Chirp waveform. An Agilent PNA-L Series Network Analyzers may be used for reference purposes. The power output of the PNA is less than the power output of the radar.

The 88th Medical Group Bio-Environmental Safety Group has evaluated both radar systems at the described parameters and concluded that they pose no significant health hazard. Copies of the test certificates are included in the appendix. Operation specifications are also available upon request.

One or both of two models of polarization cameras will be used to provide 2-D shape information during the movement tasks. In indoor settings, these cameras act as simple infrared cameras, collecting black and white images (facial features will not be recognizable). The cameras will be placed at an approximate distance of 100 feet from the capture area. The models are the PIRATE, which operates in a wavelength range of 7.8-9.8 microns, and the SPITFIRE, a four band camera that operates at 3.2-3.7, 3.7-4.2, 3.2-4.2, and 4.5-5.0 micron wavelengths. The polarization imaging is completely passive (much like the standard video cameras) and poses no risk to human subjects or persons operating the equipment. The shape output does not contain detailed facial features, so that subject identity will not be recognizable.

An ASC Flash Ladar Video Camera (FLVC) will be used to provide 3D shape information during the movement tasks. This camera can measure the range of all objects in its field of view with a single laser pulse. Light from the laser illuminates the scene in front of the camera lens, which focuses the image on to the 3D sensor focal plane array, and the range to the object viewed by each pixel can then be computed. Nominal Ocular Hazard Distance (HOHD), and Skin Hazard Distance (NSHD) were both calculated for this sensor (included in Appendix E). The sensor will be mounted at least 10 feet away from subjects, far beyond the calculated Hazard Distance, and will contain a safety guard to prevent accidental operator entrance into the hazard zone. This sensor poses no risk to human subjects or persons operating the equipment outside of the hazard zone.

b. Subjects:

We anticipate requiring approximately 50 healthy pediatric subjects, ages 4-17. The subject sample size was chosen to provide variability in size, shape, and movement patterns while still being practically attainable in terms of recruitment, cost, and time. We foresee achieving sufficient variability by targeting recruitment to attain approximately 10 subjects in each of 5 age categories: 4-6, 7-9, 10-11, 12-14, 15-17 yrs. Subjects will be recruited from base personnel using an advertisement flyer (see attached flyer), posted in buildings near the collection site. All recruitment and scheduling will be handled by Casserly Whitehead, CTR. Note that no one in an investigators chain of command will be recruited by that investigator. As recruitment progresses, specific age screening may be needed to achieve variability goals. Size and shape variability may be monitored as collection progresses, and a few additional subjects may be collected beyond the anticipated 50 if needed. No more than 75 subjects will be recruited. Parents will be required to transport, accompany, and remain with their children throughout the data collection.

c. Duration:

The time commitment for each subject will be a single session lasting approximately one to one and a half hours. Sessions will be available during the late afternoon/early evening and over some holidays to accommodate parent and student schedules. Duration for the entire study is estimated to be one year comprising data collection and analysis, although additional data analysis of the de-identified data may continue thereafter (see analysis section **8d**). In the event that a subject does not complete the entire protocol due to fatigue or other factors, the subject will be given the option of a follow up visit to complete it.

A small subject subset (up to 10 subjects) will also include an additional test session with an alternate radar configuration. The duration of this session will be approximately ½ hour.

d. Description of experiment, data collection, and analysis:

All testing (except for the alternate radar subtest) will take place in the 3D Biosignatures laboratory in Area B, Bldg 824. The radar subtest will take place in the indoor range in Area B, Bldg 620. At the beginning of the test session, each parent will be provided an informed consent document for his/her review and signature, with the opportunity for questions and clarifications. An ombudsman with no conflicts of interest will be present during the consent process to act in the best interest of the child, ensuring that the child understands the protocol and is participating voluntarily. The ombudsman will intervene at any sign that the child is hesitant to participate or that the information is not conveyed appropriately to the child. Four ombudsman have been selected, all of whom have experience with human subjects, are outside the Human Signatures branch, and are conveniently located within Bldg. 824 (see attached CVs, Appendix F):

a. John Buhrman, DR-III, Senior Biomedical Engineer, 711 HPW/RHCP, 937-255-3121, John.Buhrman@wpafb.af.mil

b. Suzanne Smith, DR-III, Senior Biomedical Engineer, 711 HPW/RHCP, 937-255-9331, Suzanne.Smith@wpafb.af.mil
c. Chris Perry, DR-III , Lead Biomedical Engineer, 711 HPW/RHCP, 937-254-5411, Chris.Perry@wpafb.af.mil
d. Nathan Wright, DR-II ,Biomedical Engineer, 711 HPW, RHCP, 937-255-2554, Nathan.wright@wpafb.af.mil

Each child will be asked to provide assent either verbally (ages 7 and under), by signing the assent form (age 8-14), or by co-signing the consent form (ages 15-17). In each case, the parent will sign the consent form. Verbal assent will be documented by the parent signing the assent form on behalf of the child, with the ombudsman signing as a witness. Each child will also be given the opportunity for questions and clarifications, and each child and parent will be shown the representative picture of a de-identified image (see below) with the ombudsman present. Parents and children will also receive a short safety briefing explaining what to do in the event of an emergency (shelter and building exit locations, etc.).

Each subject's gender, height and weight will first be recorded. A few additional limb length measurements may also be performed using a standard flexible tape measure. Subjects will be asked to provide their ethnicity and whether they are healthy, able to perform the required movements, and whether they have any implanted medical devices, prosthesis, or musculoskeletal injuries that would interfere with normal movement. Next, the retro-reflective markers (and orientation sensors if available) will be attached to the subject's skin with a skin-friendly adhesive (e.g. 3M 1522 toupee tape or similar). For accurate marker placement, the subject will wear form fitting shorts and tops that will be provided for them. An example is shown in Figure 1 below. A private changing area will be available. An experimenter of the same gender will place all markers on the subject. Parents will be present during the entire test (at no time will any investigator be alone with the subject).

FIGURE 1: This catalog example shows the typical form fitting clothing to be worn. Not that in order to place markers on the top of the pelvis, a few inches at the bottom of the shirt may be trimmed or rolled, or small cutouts may be made to expose the reflective markers. Reflective markers are placed over the medial and lateral peaks of the iliac crests as well as on the anterior and posterior superior iliac spines (ASIS and PSIS).

The subject will then be scanned in a comfortable static pose. The scanner requires that the subject hold still for only a few seconds.

Each subject will then perform several different movements in the motion capture area. These will consist of movements or activities that are performed on a regular basis, including walking or jogging the length of the capture area (approximately 50 feet), standing still in various poses, and/or picking up a small object and throwing it toward a target. No more than about five repetitions of each activity will be performed. These activities are designed to replicate typical activities that a child might engage in during various in-field surveillance scenarios. Motion capture, 2-D video, polarization camera images, ladar images, and radar will be collected during each movement (only one radar unit will be used at a time).

For the radar subtest, a few subjects will undergo radar testing (only) in bldg. 620. For this subtest, subjects will go through the consent/assent process exactly as described above. Subjects will not be required to change clothing. Testing will consist of simply standing still on a custom turntable, in a comfortable pose, for a few seconds at a time, approximately 30 times. The turntable platform is about 6 inches off the ground and will rotate the child a few degrees in between scans (the rotation of the turntable is extremely slow and has been safety approved).

As the data will be used by various collaborators in several different analyses, data will be immediately de-identified (2-D video and 3-D scans) and raw, identifiable images will be permanently deleted. De-identification of data will be done as described in section **8f** below.

Two different groups (RHXBA and RYM) will perform separate analysis on the collected data, and copies of de-identified data will be housed internally in both building 824 and 630. Access to data will be controlled by the investigators listed on the protocol (see also section **8f**).

Dr. Bruening and colleagues in RHXBA will investigate differences in size, shape, and movement between children and adults. Anthropometric measurements will be taken from the 3-D scans and compared to previously collected adult scan databases using ANOVA or regression techniques. Movement differences will also be investigated using the motion capture data, with similar statistical treatment, including ANOVA on discrete variables, or more complicated time series analysis for continuous variables. 2-D video will subsequently be used to determine whether the discovered differences from the previous analyses are detectable from planar images. Finally, 3-D avatars (animation models) will be created, incorporating realistic movement from the motion capture, for use in training scenarios.

Dr. Miranda and colleagues will investigate child/adult discrimination from radar data and 2-D video. Collected variables will be compared to similar measures in other active statistical data sets (CDC, AFRL, etc.) For radar data, a mathematical spline method will be carried out in order to extend the pre-existing anthropometric results in order to increase the robustness of the statistical analysis. Basic linear regression models will be used to form an initial first order Bayes-based classifier. A new classifier based on support machine methods will be developed and compared to the Bayes-based classifier for consistency of statistical results. 2-D video may also be analyzed in a similar fashion.

Future research on the de-identified data set will be confined to the DoD and DoD contractors for the purposes of threat detection and discrimination and other exploitation methods in support of military research, development, or operations (see confidentiality protection section **8f.** below).

e. Safety monitoring:

Subject safety throughout the data collection will be monitored by the investigators listed above. Dr. Bruening, who has experience in similar pediatric data collections through previous experience working at a children's hospital, will attend and oversee each data collection. Parents will be required to stay with their children throughout the collection, and will also be supervising. Risks should not be greater than for typical daily activities.

f. Confidentiality protection:

Subjects will be listed by name on a contact roster and assigned a study number. That number will be assigned to the test data. No other personal identifying information will be assigned to the data sets, and the roster and test data will be kept separate. The contact roster will be stored on a locked computer and locked cabinet in Bldg. 824, and accessed

only by investigators listed on this study. The de-identified data sets will then be made available to selected researchers in Bldgs 824 and 630. Data transfer will be controlled by investigators in RHXBA. A DVD (or similar media) will be used to transfer de-identified data, and all data will be marked with the following data use restrictions:

For Official Use Only (FOUO), DISTRIBUTION STATEMENT D. Distribution authorized to the Department of Defense and U.S. DoD contractors only (Administrative and Operational Use) (*date of determination*). Redistribution of this material and other requests shall be referred to (711HPW RHXBA, 2800 Q St, Bldg. 824, WPAFB OH 45433).

3-D Scanner images will be de-identified by blurring the facial pixels and colors, as shown in Figure 2. Similarly, 2-D video data will be de-identified by applying a blur or pixilation to each video frame as shown in Figure 2.

FIGURE 2: 3-D scans (left) and 2-D video (right) images will be de-identified by blurring or pixelating the face as shown above. Note that the clothing worn will be similar to that shown above, but the t-shirt and white elastic wraps will be replaced by a snug sleeveless triathlon or running top as mentioned previously

9. Risk Analysis

This study includes only tasks that are performed on a regular basis and is thought to be of minimal risk to subjects. Subjects will be informed that if they feel tired they may stop the test at any time. Slight discomfort is possible when removing the skin mounted sensors, as the adhesive may pull on arm or leg hairs or mildly irritate sensitive skin (similar to a bandage removal). The reflective motion capture markers need to be placed on landmarks

on the pelvis (ASIS and PSIS). Markers placement will be performed by an experimenter of the same gender as the child. Subjects will also be informed that if they are uncomfortable with the placement they may stop the study at any time. Parents will oversee all aspects of the data collection. Radiation exposure from the radar was tested as mentioned above and deemed insignificant. The ladar camera was also tested and is considered safe for all subjects.

10. References

1. NA

11. Attachments

A. Informed Consent Form
B. Child Assent Form
C. Curriculums Vitae of Investigators
D. CITI Training for New investigators
E. Equipment Safety Documentation (Radar and Ladar)
F. Ombudsman CVs
G. Recruitment Flyer
H. De-identified image for consent

Appendix F. IRB Documentation (Adult)

The following pages include IRB documentation for the adult volunteer study. The documents are: the signed approval letter and IRB protocol.

DEPARTMENT OF THE AIR FORCE
AIR FORCE RESEARCH LABORATORY
WRIGHT-PATTERSON AIR FORCE BASE OHIO 45433

MEMORANDUM FOR AFRL/RYMD (DR. ANALEE MIRANDA)

FROM: 711 HPW/IR (AFRL IRB)

SUBJECT: IRB approval for the use of human volunteers in research

1. Protocol title: Human Classification Using Radar
2. Protocol number: FWR20130052H
3. Protocol version: 1.0
4. Risk: Minimal
5. Approval date: 13 December 2012
6. Expiration date: 12 December 2013
7. Scheduled renewal date: 12 November 2013
8. Type of review: Initial- Expedited
9. Assurance Number and Expiration Date:
   - AFRL DoD Assurance 50002: 14 March 2014
   - AFIT DoD Assurance 50301: 29 November 2014
   - Infoscitex FWA 00008359: 1 February 2017
10. CITI Training: Completed
11. The above protocol has been reviewed and approved by the AFRL IRB via expedited review procedures. All requirements, as set by the IRB and its legal counsel, have been fully complied with. The study objective is to characterize adult's size, shape, and High Range Resolution (HRR) radar scattering at a variety of frequencies for the purpose of discriminating between differing demographics using stand-off sensors. The human images will be taken by cameras, imagers and radar limits of exposure that are found to be safe, minimal and consistent with daily life exposure limits. This protocol therefore meets the criteria for expedited review in accordance with 32 CFR 219.110 (b)(1) and U.S. Department of Health and Human Services category (4) Collection of data through noninvasive procedures (not involving general anesthesia or sedation) routinely employed in clinical practice, excluding procedures involving x-rays or microwaves. Where medical devices are employed, they must be cleared/approved for marketing. (Studies intended to evaluate the safety and effectiveness of the medical device are not

generally eligible for expedited review, including studies of cleared medical devices for new indications.)

12. A HIPAA authorization is not required, since no HIPAA protected information will be recorded in the execution of this protocol.

13. FDA regulations do not apply since no drugs, supplements, or unapproved medical devices will be used in this research.

14. This approval applies only to the requirements of 32 CFR 219, DoDD 3216.2, AFI 40-402, and related human research subject regulations. If this project is a survey, attitude or opinion poll, questionnaire or interview, consult AFI 38-501, AF Survey Program, for further guidance. Headquarters AFPC/DPSAS is the final approval authority for conducting attitude and opinion surveys within the Air Force. If the survey, attitude or opinion poll, questionnaire or interview is hosted on a .com server, consult AFI 33-129, Web Management and Effective Use of Internet-based Capabilities, for further guidance. If the study is being conducted under an Investigational New Drug (IND) or Device Exemption (IDE), a copy of the FDA IDE or IND approval letter must be submitted by the Principal Investigator to the IRB.

15. Any serious adverse event or issues resulting from this study should be reported immediately to the IRB. Amendments to protocols and/or revisions to informed consent documents must have IRB approval prior to implementation. Please retain both hard copy and electronic copy of the final approved protocol and informed consent document.

16. All inquiries and correspondence concerning this protocol should include the protocol number and name of the primary investigator. Please ensure the timely submission of all required progress and final reports and use the templates provided on the AFRL IRB web site http://www.wpafb.af.mil/library/factsheets/factsheet.asp?id=7496 .

17. For questions or concerns, please contact the IRB administrator, Lt Robert Walker at Robert.walker@wpafb.af.mil or (937) 904-8094. All inquiries and correspondence concerning this protocol should include the protocol number and name of the primary investigator.

KIM E. LONDON, CIP
Acting Chair, AFRL IRB

cc:
AFMSA/SGE-C

1st Indorsement to AFRL/RYMD (DR. ANALEE MIRANDA) Memo, 13 December 2012, Initial Approval, Expedited Review, Protocol #FWR20130052H

MEMORANDUM FOR 711 HPW/IR (KIM LONDON)

I have reviewed the hardcopy and electronic records and found them to be complete and accurate.

ROBERT L. WALKER 2 Lt, USAF
Lead Administrator, AFRL IRB

2nd Indorsement to AFRL/RYMD (DR. ANALEE MIRANDA) Memo, 13 December 2012, Initial Approval, Expedited Review, Protocol #FWR20130052H

MEMORANDUM FOR AFMSA/SGE-C

This protocol has been reviewed and approved by the AFRL IRB. I concur with the recommendation of the IRB and approve this research.

21 DEC 2012

TIMOTHY T. JEX
Brigadier General, USAF, MC, CFS
Commander
711th Human Performance Wing

Human Classification Using Radar
F-WR-2013-0052-H

1. **Principal Investigator**
   a. Miranda, Analee, DR-II, Research Mathematician, AFRL/RYMD, 937-528-8118, analee.miranda@wpafb.af.mil

2. **Associate Investigators**
   a. Dustin Bruening, DR-II, 711 HPW/RHXBA, 937-255-5272, dustin.bruening @wpafb.af.mil
   b. David Bowden, DR-I, Electrical Engineer, 711 HPW/RHXBA, 937-255-8518, david.bowden@wpafb.af.mil
   c. Christopher Hess, Research Technician, Infoscitex Corp., 937-255-5390, christopher.hess2@wpafb.af.mil
   d. Derek Benson, Research Technician, Infoscitex Corp., 937-255-2058, derek.benson@wpafb.af.mil
   e. Westbrook, Lamar, DR-I, Electronics Engineer, AFRL/RYMD, 937-528-8114, lamar.westbrook@wpafb.af.mil
   f. Keith, Stephanie, Captain, AFIT/ENP, 937-785-3636, Stephanie.Keith@afit.edu

3. **Medical Consultant or Research Monitor**
   Not applicable

4. **Facility/Contractor**
   This research effort will be conducted by government personnel from the Multispectral Sensing & Detection Division, Sensors Directorate, Air Force Research Laboratory (AFRL/RYM.) This research effort will also be conducted by personnel from the Human Signatures Branch, Forecasting Division, Human Effectiveness Directorate, Air Force Research Laboratory (711 HPW/RHXBA), under work unit 71840226 as well as by RHXBA's in-house contractor, Infoscitex, under the Federal-wide Assurance Number 00008359 with the Department of Defense Addendum number F50339.

5. **Objective**
   To characterize adult's size, shape, and High Range Resolution (HRR) radar scattering at a variety of frequencies for the purpose of discriminating between differing demographics using stand-off sensors.

6. **Background**
   Modern defense applications have become increasingly human-centric. Humans are more diverse and adaptive than conventional targets such as tanks and aircrafts, and can be difficult to evaluate without a comprehensive understanding of human characteristics as measured at standoff. While past focus has been on the problem of discriminating between human motions, we will collect data from a variety of sensors to derive a functional relationship between human HRR profiles at a variety of frequencies and

anthropometric data sets. In order to develop statistically robust mapping algorithms between the anthropometric data and HRR profiles a broad band of frequencies will be required. This new data will allow exploration of stand-off discrimination between human demographic groups.

7. Impact

By creating an algorithmic mapping to distinguish between human demographic groups at standoff we will improve the situational awareness of the warfighter. This work thus serves the purpose of increasing awareness while simultaneously reducing risk**. In addition, the capability for an all-weather/season solution is of utmost important. Discrimination of human subjects wearing layers of clothing or shielded from cloud cover or canopy is now possible with certain sensors and via state-of-the-art image and signals processing. It is the goal of this study to verify that these sensors and algorithms indeed achieve a low-false-alarm classification and discrimination of features such gender, size, height, and age.**

8. Experimental Plan

a. Equipment:

3-D size and shape information will be collected using a 3DMD (Atlanta, Ga.) white-light whole body scanner. The scanner consists of 9 camera mounts, each comprising two black and white cameras, two color cameras, and one projection camera. The cameras operate similar to standard digital cameras, emitting a brief white light flash to illuminate the subject. The various camera images and views are then combined to create a high resolution 3D point cloud or mesh. The whole-body scanner does not see through clothing, but rather returns what amounts to a 3D surface camera image. Accordingly, the scanner is no more intrusive than a standard digital camera.

Low-power indoor radar will be used to record the phase-Doppler signatures of the test movements.

1) A linear frequency modulated homodyne (LFMH) radar with separate transmission and receiving antenna units. The system is capable of supporting frequency chirp rates of up to 10 KHz while maintaining 512 frequency steps/chirp, with 10-20 cm resolution cells. The system is operational between 2-18 GHz, however, in this test, we will only be using X and Ku band.

2) A bistatic, low power (less than 1 Watt) Doppler-range radar operating from 250 MHz up to 3 GHz using a pulsed Chirp waveform.

3) NEW ADDITTION: An Agilent PNA-L Series Network Analyzer (static measurements) will be used in conjunction with the antennas used in sensor 2. The power output of the PNA-L is significantly less than the power output of the radar (~ 0.003 Watts.) This new sensor will be used in two ways:

a) **3D Biosignatures laboratory, Building 824, Area B; in conjunction with the other sensors previously approved.**
b) **Indoor Range, Building 620, Area B, Indoor Range behind a wall (which decreases the radiation output.) and using a turntable.**

The reason for this change is to increase the situational awareness to the warfighter in situations when the human subjects are located inside a building or man-made structure. This new location is required due to the extremely LOW power nature of the system. The system is extremely low power (SIGNIFICANTLY safer to the human subjects) and requires a quiet area in order to receive the scattering measurements. The measurements in this alternate location will only be performed on a small subset (less than 10 subjects) of the group. This test will be performed over a short period of time (less than one month) and will conclude when the data acquired from the 10 subjects is collected. Appropriate safety inspections and protocols have been completed. The relevant safety documentation is included as an attachment.

3) An Xbox 360 Kinect sensor. This sensor is equipped with multiple passive detectors and emits no radiation.

4) 2D video may also be taken with a standard video camera.

5) Participants will also be asked to carry a pedometer attached to the waist or a phone with a pedometer application in their pockets. Neither of these will emit radiation above that of a standard cellular phone.

6) Polarization Cameras: The two polarization cameras to be used in this study are the PIRATE camera which operates at 7.8-9.8 microns and the SPITFIRE, a four band camera that operates at 3.2-3.7, 3.7-4.2, 3.2-4.2, and 4.5-5.0 microns. The benefit of polarization sensing is that it provides 3D shape information of the objects in view from a passive sensor. So, where you could get true 3D shape information of a vehicle or a face from a laser radar system, polarization gives you this information passively, with one image. For this study, the polarization data will be used to evaluate the changes in the 3D signatures of human subjects performing the operationally relevant activities described below. Because the polarization imaging technique is completely passive (much like a standard video camera), this type of sensor poses no risk to human subjects or persons operating the equipment.

7) Hyper-spectral Imagers: The Four Hyper-spectral imagers to be used in this study are the ASD FieldSpec 3 which operates in the range of 350-2500nm, the HyperSpectTIR HST which operates in the range of 450-2450nm, the PHIRST light II SCC BAE which operates in the range of 400-720nm, and the SOC700 which operates in the range of 430-900 nm. The collection of hyper-spectral data takes advantage of hundreds of spectral channels producing extremely high resolution that provide characteristics of materials

previously missed with multi-spectral imagers. For this study, hyper-spectral imagers will be used to determine the slightest change from 350nm - 2500nm wavelengths (1nm - 10nm resolution), of dismounts performing operationally relevant activities. Hyper-spectral imaging is completely passive (just like a standard video camera), so these sensors will pose no risk to human subjects or persons operating the equipment.

8) Ladar Video Camera: The ladar video camera to be used in this study is the ASC Flash Ladar Video Camera (FLVC). This camera can measure the range of all objects in its field of view with a single laser pulse. Light from the laser illuminates the scene in front of the camera lens, which focuses the image on to the 3D sensor focal plane array. The range to the object viewed by each pixel can then be computed. The benefit of a Ladar Video Camera is that it can provide 3D shape information in real time, and that is a sensor that could be used in the field, not just a laboratory. Nominal Ocular Hazard Distance (HOHD), and Skin Hazard Distance (NSHD) were both calculated for this sensor. These values were calculated for unaided viewing (Bare eye, no focusing optics), and aided viewing (Focusing optics). The greatest distance for any of these calculations is 200cm. The sensor will be mounted approximately 100 feet away from subjects and equipment operators, which is far beyond the calculated Hazard Distances. This sensor poses no risk to human subjects or persons operating the equipment.

The 88th Medical Group Bio-Environmental Safety Group has evaluated all radar systems at the described parameters and concluded that they pose no significant health hazard. Copies of the test certificates are included in the appendix. Operation specifications are also available upon request.

b. Subjects:

We anticipate requiring approximately 100 healthy adult subjects over the age of 18. The subject sample size was chosen to provide variability in size and shape while still being practically attainable in terms of recruitment, cost, and time. The first wave of testing will be accomplished by targeting recruitment to attain subjects in each of 3 age categories: 18-29, 30-50, and 50+ yrs. Subjects will be recruited from all WPAFB personnel using an e-mail announcement and flyer, see attachments 1 and 2. We will then analyze the subjects' height, BMI, and other anthropometric measurements to determine the statistical robustness of the sample group. Based on this analysis, further advertising may be done in order to achieve an approximation of the anthropometric measurements of the broader population.

NOTE: If necessary we will recruit subjects of a specific set of measurements (height, weight, etc.) from a local talent agency in order to round out our data set to achieve the necessary statistical robustness. For instance the PC Goenner Talent Agency located at 123 Webster St. Dayton OH 45402 has a wide variety of persons available for hire at

hourly rates for modeling. This option will only be used if the volunteer sample set lacks sufficient statistical robustness. An amendment to the protocol will be submitted to the IRB should this option occur. No varying recruitment methods will be used until IRB approval of said changes.

c. Duration:

The time commitment for most subjects will be a single session lasting approximately one hour to one and a half hours. The time commitment for a small subset of no more than 10 participants will be asked to perform a second session in the Indoor Range, Area B, Bldg 620. This additional second session will last approximately 30-45 minutes. Duration for the entire study is estimated to be one year comprising data collection and analysis, although additional data analysis may continue thereafter.

d. Description of experiment, data collection, and analysis:

Most testing will take place in the 3D Biosignatures laboratory in Area B, Bldg 824. A small subset of 10 participants will be asked to perform a second session in the Indoor Range, Area B, Bldg 620. At the beginning of the test session, each subject will be provided an informed consent document for his/her review and signature, with the opportunity for questions and clarifications.

Each subject's gender, height, and weight will be recorded. Subjects will also be asked to provide their ethnicity and whether they are healthy, able to perform the required movements, and whether they have any implanted medical devices, prosthesis, or other medical conditions that could exclude them from participation. A few additional limb length measurements may also be performed using a standard flexible tape measure.

The subject will then be scanned in a comfortable static pose. The scanner requires that the subject hold still for only a few seconds.

Each subject will then perform several different movements in the motion capture area where the radars are situated. These will consist of movements or activities that are performed on a regular basis, including walking the length of the capture area (approximately 50 feet), standing still in various poses, picking up a small object (ie, a pen or a tennis ball), and pantomiming a throwing motion. No more than about five repetitions of each activity will be performed. These activities are designed to replicate typical activities that an adult might engage in during various in-field surveillance scenarios and to achieve necessary radar cross sections. 2-D video and radar will be collected during each movement (only one radar unit will be used at a time).

For a small subset of the participating group, an appointment will be scheduled to perform a data collection in the indoor range. Each subject's gender, height, arm length, leg length, and head size will be recorded after the signed consent form is

collected. The subject will then enter the indoor range and stand in a turntable that will rotate every twenty seconds for at most thirty times. The radar will be turned on and off during that period. A rest period may be requested if the subject is tired or requires rest. The total time the subject will need to stand in the turntable is approximately 15 – 45 minutes (rest periods are included in this estimate.) The experiment will stop should a participant find standing for a prolonged period of time difficult.

As the data will be used by various collaborators in several different analyses, data will be immediately de-identified (2-D video and 3-D scans) and raw, identifiable images will be permanently deleted. De-identification of data will be done as described in section **8f** below.

Two different groups (RHXBA and RYM) will perform separate analysis on the collected data, and copies of de-identified data will be housed internally in both building 824 and 620. Access to data will be controlled by the investigators listed on the protocol (see also section **8f**).

Dr. Bruening and colleagues in RHXBA will investigate differences in size, shape, and movement between differing demographic groups. Anthropometric measurements will be taken from the 3-D scans and compared to previously collected adult scan databases using regression techniques. 2-D video will subsequently be used to determine whether the discovered differences from the previous analyses are detectable from planar images.

Dr. Miranda and colleagues will investigate human target discrimination from radar data and 2-D video. Collected variables will be compared to similar measures in other active statistical data sets (CDC, AFRL, etc.) For radar data, a mathematical spline method will be carried out in order to extend the pre-existing anthropometric results to increase the robustness of the statistical analysis. Basic linear regression models will be used to form an initial first order Bayes-based classifier. A new classifier based on support machine methods will be developed and compared to the Bayes-based classifier for consistency of statistical results. 2-D video may also be analyzed in a similar fashion.

e. Safety monitoring:

The investigators listed above will monitor subject safety throughout the data collection. Risks should not be greater than for typical daily activities.

f. Confidentiality protection:

Subjects will be listed by name on a contact roster and assigned a study number. That number will be assigned to the test data. No other personal identifying information will be assigned to the data sets, and the roster and test data will be kept separate. The contact roster will be stored on a locked computer and locked cabinet in Bldg. 824, and accessed

only by investigators listed on this study. The de-identified data sets will then be made available to selected researchers in Bldgs 824 and 620. Access will be controlled as mentioned above.

3-D Scanner images will be de-identified by blurring the facial pixels and colors, as shown in Figure 2. Similarly, 2-D video data will be de-identified by applying a blur or pixilation to each video frame as shown in Figure 2.

9. Risk Analysis

This study includes only tasks that are performed on a daily basis and is thought to be of minimal risk to subjects. Subjects will be informed that if they feel tired they may stop the test at any time. Radiation exposure from the radar is well below the exposure limit of $2\ ^{W}/_{m^2}$ for 6 minutes/action level of $1\ ^{W}/_{m^2}$. The results from the Electromagnetic Frequency Radiation Surveys conducted 8-14 Aug 2012 AND 18 Dec 2012 demonstrates the measurements, calculations, and delineates the exposure limits as required by law.

10. References

1. NA

11. Attachments

A. E-Mail Announcement
B. Flyer
C. Informed Consent Form
D. Resumes of investigators
E. Electromagnetic Frequency Radiation Surveys (2)
F. Safety Inspection Letter

Bibliography

1. Analee M. Miranda. Personal Communication, Dec. 2012.

2. Shobha Sundar Ram, Yang Li, Adrian Lin, and Hao Ling. Doppler-based detection and tracking of humans in indoor environments. *Journal of the Franklin Institute*, 345(6):679 – 699, 2008. Advances in Indoor Radar Imaging.

3. Ram M. Narayanan. Through-wall radar imaging using UWB noise waveforms. *Journal of the Franklin Institute*, 345(6):659 – 678, 2008. Advances in Indoor Radar Imaging.

4. Pin-Heng Chen, R.M. Narayanan, Chieh-Ping Lai, and A. Davydov. Through wall ranging and imaging using UWB random noise waveform: System design considerations and preliminary experimental results. In *Antennas and Propagation Society International Symposium, 2009. APSURSI '09. IEEE*, pages 1 –4, June 2009.

5. Hong Wang, R. M. Narayanan, and Zheng Ou Zhou. Through-wall imaging of moving targets using UWB random noise radar. *Antennas and Wireless Propagation Letters, IEEE*, 8:802–805, 2009.

6. C.-P. Lai, R.M. Narayanan, Q. Ruan, and A. Davydov. Hilbert-huang transform analysis of human activities using through-wall noise and noise-like radar. *Radar, Sonar Navigation, IET*, 2(4):244 –255, August 2008.

7. R. M. Narayanan, M. C. Shastry, P. H. Chen, and M. Levi. Through-the-wall detection of stationary human targets using doppler radar. *Progress In Electromagnetics Research B*, 20:147–166, 2010.

8. Donna Miles. New device will sense through concrete walls. World Wide Web Page, 3 Jan 2006. Keywords: Radar Scope, Baranoski.

9. Edward J Baranoski. New sensor signal processor paradigms: When one pass isn't enough. In *HPEC 2008*, Sept 23-25 2008.

10. A.S. Bugaev, V.V. Chapursky, S.I. Ivashov, V.V. Razevig, A.P. Sheyko, and I.A. Vasilyev. Through wall sensing of human breathing and heart beating by monochromatic radar. In *Ground Penetrating Radar, 2004. GPR 2004. Proceedings of the Tenth International Conference on*, volume 1, pages 291 –294, June 2004.

11. E. F. Greneker, J. L Geisheimer, D. S. Andreasen, O. D. Asbel, B. L. Stevens, and B. S. Mitchell. Development of inexpensive radar flashlight for law enforcement and corrections applications. Technical report, Georgia Tech Research Institute, Apr 30 2000.

12. Analee Miranda. Radar imaging and feature detection of biological media.

13. P. Barber and C. Yeh. Scattering of electromagnetic waves by arbitrarily shaped dielectric bodies. *Applied Optics*, 14(12):2864, 1975.

14. K. Sarabandi and P.F. Polatin. Electromagnetic scattering from two adjacent objects. *Antennas and Propagation, IEEE Transactions on*, 42(4):510 –517, Apr 1994.

15. J. Park, J. T. Johnson, N. Majurec, M. Frankford, E. Culpepper, J. Reynolds, J. Tenbarge, and L. Westbrook. Software defined radar studies of human motion signatures. In *Radar Conference (RADAR), 2012 IEEE*, page 0596, 7-11 May 2012 2012.

16. Michael Otero. Application of a continuous wave radar for human gait recognition. pages 538–548, 2005.

17. S.S. Ram and Hao Ling. Microdoppler signature simulation of computer animated human and animal motions. In *Antennas and Propagation Society International Symposium, 2008. AP-S 2008. IEEE*, pages 1 –4, July 2008.

18. T. Thayaparan, L. Stanković, and I. Djurović. Micro-doppler-based target detection and feature extraction in indoor and outdoor environments. *Journal of the Franklin Institute*, 345(6):700 – 722, 2008. Advances in Indoor Radar Imaging.

19. Youngwook Kim and Hao Ling. Human activity classification based on micro-doppler signatures using a support vector machine. *Geoscience and Remote Sensing, IEEE Transactions on*, 47(5):1328 –1337, May 2009.

20. P. van Dorp and F.C.A. Groen. Human walking estimation with radar. *Radar, Sonar and Navigation, IEE Proceedings* -, 150(5):356 – 365, Oct. 2003.

21. S. Z. Gürbüz, W. L. Melvin, and D. B. Williams. Detection and identification of human targets in radar data. In *Society of Photo-Optical Instrumentation Engineers (SPIE) Conference Series*, volume 6567 of *Society of Photo-Optical Instrumentation Engineers (SPIE) Conference Series*, April 2007.

22. Ronan Boulic, Nadia Magnenat-Thalmann, and Daniel Thalmann. A global human walking model with real-time kinematic personification. *The Visual Computer*, 6:344–358, 1990.

23. J. Park, JT Johnson, N. Majurec, M. Frankford, E. Culpepper, J. Reynolds, J. Tenbarge, and L. Westbrook. Software defined radar studies of human motion signatures. In *Radar Conference (RADAR), 2012 IEEE*, pages 0596–0601, 2012.

24. Dustin P. Fairchild and Ram M. Narayanan. Human activity classification using hilbert-huang transform analysis of radar doppler data. In *Proc. SPIE 8021, Radar Sensor Technology XV*, 2011.

25. E.F. Greneker. Radar sensing of heartbeat and respiration at a distance with applications of the technology. In *Radar 97 (Conf. Publ. No. 449)*, pages 150 –154, Oct 1997.

26. A.G. Yarovoy, L.P. Ligthart, J. Matuzas, and B. Levitas. UWB radar for human being detection. *Aerospace and Electronic Systems Magazine, IEEE*, 21(11):22 –26, Nov. 2006.

27. Revision of part 15 of the commissions rules regarding ultra-wideband transmission systems, first report and order. pages 12–16. Federal Communications Commission, February 14, 2002.

28. S.R.J. Axelsson. Random noise radar/sodar with ultrawideband waveforms. *Geoscience and Remote Sensing, IEEE Transactions on*, 45(5):1099 –1114, May 2007.

29. S.Z. Gürbüz, W.L. Melvin, and D.B. Williams. Detection and identification of human targets in radar data. In *Signal Processing, Sensor Fusion, and Target Recognition XVI, Proc. SPIE*, volume 6567, 2007.

30. David Bowden. An age-based classification model derived from anthropometric measurements. Technical report, Air Force Research Lab, 711HPW RHXBA, April 2012.

31. Matt Ferrara, Ron Miller, Micah North, and Jonothan Pryor. Green man measurement and signal processing, small human discrimination from standoff. Unpublished progress report, Matrix Research, Inc., May 7, 2012.

32. E. Bleszynski, M. Bleszynski, and T. Jaroszewicz. Feature extractions, small human discrimination from standoff. Unpublished progress report, Monopole Research, December 01, 2011 - March 31, 2012.

33. Margaret A. McDowell, Cheryl D. Fryar, Cynthia L. Ogden, and Katherine M. Flegal. Anthropometric reference data for children and adults: United States, 2003–2006. Number 10. Centers for Disease Control and Prevention, Oct. 22, 2008.

34. Merrill I. Skolnik. *Introduction to Radar Systems*. McGraw-Hill, New York, NY, 3rd edition, 2001.

35. Julius A. Stratton. *Electromagnetic Theory*. McGraw-Hill, New York, NY, 1st edition, 1941.

36. Bo E. Sernelius. Lecture 12: Reflection and refraction, electrodynamics course, 2012.

37. Ashley L. Schmitt. Radar imaging with a network of digital noise radar systems. Master's thesis, Air Force Institute of Technology, 2009.

38. C. Thajudeen, A. Hoorfar, and F. Ahmad. Measured complex permittivity of walls with different hydration levels and effect on power estimation of TWRI target returns. *Progress In Electromagnetics Research B*, 30:177–199, 2011.

39. K. Viriyametanont, S. Laurens, G. Klysz, J.-P. Balayssac, and G. Arliguie. Radar survey of concrete elements: Effect of concrete properties on propagation velocity and time zero. *NDT & E International*, 41(3):198 – 207, 2008.

40. G. Klysz, J.P. Balayssac, and X. Ferrières. Evaluation of dielectric properties of concrete by a numerical FDTD model of a GPR coupled antenna–parametric study. *NDT & E International*, 41(8):621 – 631, 2008.

41. M.N Soutsos, J.H Bungey, S.G Millard, M.R Shaw, and A Patterson. Dielectric properties of concrete and their influence on radar testing. *NDT & E International*, 34(6):419 – 425, 2001.

42. Steven M. Kay. *Modern Spectral Estimation: Theory and Application*. Prentice Hall, Englewood Cliffs, NJ, 1988.

43. K. Sarabandi, F.T. Ulaby, and M.A. Tassoudji. Calibration of polarimetric radar systems with good polarization isolation. *Geoscience and Remote Sensing, IEEE Transactions on*, 28(1):70 –75, Jan 1990.

44. Lindsay I. Smith. *A Tutorial on Principal Components Analysis*. University of Otago, New Zealand, February 26, 2002.

45. Grant D. Erdmann. Data classification methodology. Technical report, Air Force Research Lab, 2005.

46. Gleb V. Tcheslavski. Lecture 7: Helmholtz wave equations and plane waves, 2008.

47. Roger F. Harrington. *Time-Harmonic Electromagnetic Fields*. McGraw-Hill, New York, NY, 1961.

48. Bernhard Scholkopf and Alexander J. Smola. *Learning with Kernels: Support Vector Machines, Regularization, Optimization, and Beyond*. The MIT Press, Cambridge, Massachusetts, 2002.

49. S. Bohte, M. Breitenbach, and G. Gudic. Nonparametric classification with polynomial MPMC cascades. In *Proceedings of the 21st International Conference on Machine Learning*, Banff, Canada, 2004.

50. A.R. Conn, N.I.M. Gould, D. Orban, and Ph.L. Toint. A primal-dual trust-region algorithm for non-convex nonlinear programming. *Math. Program., Ser. B*, 87:215–249, 2000.

51. G. Erdmann. *A New Minimax Method and Its Application to Optics Problems*. PhD thesis, University of Minnesota School of Mathematics, 2003.

Vita

Captain Stephanie R. Keith graduated from the University of North Dakota with a Bachelor of Science degree in Physics, in May, 2008. Upon graduation, she was commissioned as a Second Lieutenant through AFROTC Detachment 610. Her first assignment was to the Air Force Research Lab, Detachment 7, Edwards Air Force Base, California, where she served as Propulsion Physicist in the Aerospace Branch, supporting satellite propulsion research and development. Specifically, she was a key member of the Advanced Concepts Group, researching novel methods of monopropellant fuel ignition. In August, 2011, she entered the Graduate School of Engineering and Management, Air Force Institute of Technology, for a Master of Science degree in Applied Physics. Upon graduation, she will be assigned to NASIC's Persistent Infrared Squadron.

REPORT DOCUMENTATION PAGE

Form Approved
OMB No. 0704–0188

1. REPORT DATE *(DD–MM–YYYY)*	2. REPORT TYPE	3. DATES COVERED *(From — To)*
21–03–2013	Master's Thesis	Sept 2011 — Mar 2013

4. TITLE AND SUBTITLE

DISCRIMINATION BETWEEN CHILD AND ADULT FORMS USING RADAR FREQUENCY SIGNATURE ANALYSIS

5a. CONTRACT NUMBER

5b. GRANT NUMBER

5c. PROGRAM ELEMENT NUMBER

6. AUTHOR(S)

Keith, Stephanie R., CAPT, USAF

5d. PROJECT NUMBER

5e. TASK NUMBER

5f. WORK UNIT NUMBER

7. PERFORMING ORGANIZATION NAME(S) AND ADDRESS(ES)

Air Force Institute of Technology
Graduate School of Engineering and Management (AFIT/EN)
2950 Hobson Way
WPAFB OH 45433-7765

8. PERFORMING ORGANIZATION REPORT NUMBER

AFIT-ENP-13-M-20

9. SPONSORING / MONITORING AGENCY NAME(S) AND ADDRESS(ES)

Air Force Research Laboratory
2950 Hobson Way
WPAFB OH 45433-7765
DSN 271-0690, COMM 937-255-3636
Email: analee.miranda@wpafb.af.mil

10. SPONSOR/MONITOR'S ACRONYM(S)

AFRL,RF

11. SPONSOR/MONITOR'S REPORT NUMBER(S)

12. DISTRIBUTION / AVAILABILITY STATEMENT

DISTRIBUTION STATEMENT A.:
APPROVED FOR PUBLIC RELEASE; DISTRIBUTION UNLIMITED.

13. SUPPLEMENTARY NOTES

14. ABSTRACT

In this thesis we develop a method to discriminate between adult and child radar signatures. In particular, we examine radar data measured from behind a wall, which introduces radar signal attenuation and multipath effects. To investigate the child/adult discrimination problem in a through-wall, multipath scenario, a previously developed free-space human scattering model was expanded to incorporate multiple paths, and the effects of transmission through, and reflections from, walls and ground. In addition to the model expansion, radar scattering measurements were collected from human volunteers, both child and adult, in order to investigate the classification of child and adult through-wall radar data. To our knowledge, this is the first published work that analyzes child radar scattering data. A classification accuracy of above 95% was reached in both the time and frequency domains, indicating that, with minimal processing, it is possible to achieve a high degree of certainty of the identity of a subject behind a wall, in a real-world, multipath environment.

15. SUBJECT TERMS

Radar Imaging, Pattern Recognition, Non-combatants

16. SECURITY CLASSIFICATION OF:			17. LIMITATION OF ABSTRACT	18. NUMBER OF PAGES	19a. NAME OF RESPONSIBLE PERSON
a. REPORT	b. ABSTRACT	c. THIS PAGE			Dr. A. L. Magnus, AFIT/ENP
U	U	U	UU	213	19b. TELEPHONE NUMBER *(include area code)* (937) 255-3636, x4555; amy.magnus@afit.edu